

REPORT DOCUMENTATION PAGE			Form Approved OMB NO. 0704-0188		
<p>The public reporting burden for this collection of information is estimated to average 1 hour per response, including the time for reviewing instructions, searching existing data sources, gathering and maintaining the data needed, and completing and reviewing the collection of information. Send comments regarding this burden estimate or any other aspect of this collection of information, including suggestions for reducing this burden, to Washington Headquarters Services, Directorate for Information Operations and Reports, 1215 Jefferson Davis Highway, Suite 1204, Arlington VA, 22202-4302. Respondents should be aware that notwithstanding any other provision of law, no person shall be subject to any penalty for failing to comply with a collection of information if it does not display a currently valid OMB control number.</p> <p>PLEASE DO NOT RETURN YOUR FORM TO THE ABOVE ADDRESS.</p>					
1. REPORT DATE (DD-MM-YYYY) 03-08-2015		2. REPORT TYPE Final Report		3. DATES COVERED (From - To) 13-Feb-2012 - 12-Feb-2015	
4. TITLE AND SUBTITLE Final Report: Prognostic Health Management of DoD Assets			5a. CONTRACT NUMBER W911NF-12-1-0079		
			5b. GRANT NUMBER		
			5c. PROGRAM ELEMENT NUMBER 206022		
6. AUTHORS Mannur J. Sundaresan, Albert Esterline			5d. PROJECT NUMBER		
			5e. TASK NUMBER		
			5f. WORK UNIT NUMBER		
7. PERFORMING ORGANIZATION NAMES AND ADDRESSES North Carolina A&T State University 1601 East Market Street Greensboro, NC 27411 -0001			8. PERFORMING ORGANIZATION REPORT NUMBER		
9. SPONSORING/MONITORING AGENCY NAME(S) AND ADDRESS (ES) U.S. Army Research Office P.O. Box 12211 Research Triangle Park, NC 27709-2211			10. SPONSOR/MONITOR'S ACRONYM(S) ARO		
			11. SPONSOR/MONITOR'S REPORT NUMBER(S) 60562-EG-REP.10		
12. DISTRIBUTION AVAILABILITY STATEMENT Approved for Public Release; Distribution Unlimited					
13. SUPPLEMENTARY NOTES The views, opinions and/or findings contained in this report are those of the author(s) and should not be construed as an official Department of the Army position, policy or decision, unless so designated by other documentation.					
14. ABSTRACT This proposed research will synergistically developed numerical models, experiments, algorithms, and other tools applicable to prognostic health management. The topics covered included (1) Characterize acoustic emission signals from different failure modes in composite materials, and identification of the features of critical damage, (2) Experimental characterization of the influence of attenuation on acoustic emission signals in carbon epoxy composite laminates (3) Characterization of acoustic emission signals during fatigue crack growth in aluminum panels. (4) Characterization of fretting related acoustic emission signals, in which acoustic emission characteristics					
15. SUBJECT TERMS Structural Health Monitoring, Acoustic emission, numerical analysis, composite materials					
16. SECURITY CLASSIFICATION OF:			17. LIMITATION OF ABSTRACT UU	15. NUMBER OF PAGES	19a. NAME OF RESPONSIBLE PERSON Mannur Sundaresan
a. REPORT UU	b. ABSTRACT UU	c. THIS PAGE UU			19b. TELEPHONE NUMBER 336-285-3750

Report Title

Final Report: Prognostic Health Management of DoD Assets

ABSTRACT

This proposed research will synergistically developed numerical models, experiments, algorithms, and other tools applicable to prognostic health management. The topics covered included (1) Characterize acoustic emission signals from different failure modes in composite materials, and identification of the features of critical damage, (2) Experimental characterization of the influence of attenuation on acoustic emission signals in carbon epoxy composite laminates (3) Characterization of acoustic emission signals during fatigue crack growth in aluminum panels, (4) Characterization of fretting related acoustic emission signals, in which acoustic emission characteristics were correlated with the features of the surfaces participating in the frictional process, (5) Identification for the first time the horizontal shear component of acoustic emission signals and designing sensors capable of detecting these components, along with securing a US patent on this sensor, (6) Development of a Multiagent based structural health monitoring system, (7) Development of a machine learning system for classifying acoustic emission signals, and (8) Supporting summer internships for three minority high school students during the summer of 2014 and another three minority high school students which is planned during the summer of 2015.

Enter List of papers submitted or published that acknowledge ARO support from the start of the project to the date of this printing. List the papers, including journal references, in the following categories:

(a) Papers published in peer-reviewed journals (N/A for none)

Received

Paper

08/30/2013	1.00	Kassahun Asamene, Mannur Sundaresan. Analysis of experimentally generated friction related acoustic emission signals, Wear, (08 2012): 607. doi: 10.1016/j.wear.2012.07.019
------------	------	---

TOTAL: 1

Number of Papers published in peer-reviewed journals:

(b) Papers published in non-peer-reviewed journals (N/A for none)

Received

Paper

TOTAL:

Number of Papers published in non peer-reviewed journals:

(c) Presentations

Number of Presentations: 0.00

Non Peer-Reviewed Conference Proceeding publications (other than abstracts):

<u>Received</u>	<u>Paper</u>
08/30/2013	2.00 Bonaventure Mills-Dadson, ABM Islam, Kassahun Asamene, Mannur Sundaresan. Monitoring Friction Related Surface Degradation Using AcousticEmission Technique, Proceedings of SPIE Smart Structures and NDE Conference March 2013, San Diego, CA. 10-MAR-13, . : ,
08/30/2013	3.00 Chantly Smith, Gopal Kumaran , Mannur Sundaresan, Letchuman Sripragash. Monitoring Damage Development Around Stress Raisers inCarbon/Epoxy Laminates, Proceedings of SPIE Smart Structures and NDE Conference March 10-13, 2013, San Diego, CA. 10-MAR-13, . : ,
08/30/2013	4.00 Travis Whitlow, Kassahun Asamene , Larry Hudson, Alan Parker , Mannur Sundaresan. Monitoring Damage Growth in Carbon/Epoxy Composite Panels, Proceedings of SPIE Smart Structures and NDE Conference March 10-13, 2013, San Diego, CA. 10-MAR-13, . : ,
08/30/2013	5.00 Perngjin Pai, Jun Liu , Mannur Sundaresan. Dynamic characteristics and vibration-based damage inspection ofstructures with actual fatigue cracks, Proceedings of SPIE Smart Structures and NDE Conference March 10-13, 2013, San Diego, CA. 10-MAR-13, . : ,
09/08/2014	8.00 Albert Esterline, William Wright , Jules Chenou. Weather-Monitoring Sensor Web for SupportingSituation Awareness, IEEE Interdisciplinary conference on cognitive methods in situation awareness. 03-MAR-14, . : ,
TOTAL:	5

Number of Non Peer-Reviewed Conference Proceeding publications (other than abstracts):

Peer-Reviewed Conference Proceeding publications (other than abstracts):

<u>Received</u>	<u>Paper</u>
-----------------	--------------

TOTAL:

Number of Peer-Reviewed Conference Proceeding publications (other than abstracts):

(d) Manuscripts

<u>Received</u>	<u>Paper</u>
08/30/2013	6.00 Duwarahan Rajendra, Craig Supria , Mannur Sundaresan, Hardik Vagh. Shear Horizontal wave detection and analysis in fatigue crack growth related acoustic emission signals, TBD (08 2013)
08/30/2013	7.00 Albert Esterline, Mannur Sundaresan. A Multiagent-based Structural Health Monitoring System, Manuscript (08 2013)
TOTAL:	2

Number of Manuscripts:

Books

<u>Received</u>	<u>Book</u>
TOTAL:	

<u>Received</u>	<u>Book Chapter</u>
TOTAL:	

Patents Submitted

Acoustic Emission Sensor Array

Patents Awarded

Acoustic Emission Sensor Array

~~This patent application is approved and is pending payment of patent fees~~

Awards

Graduate Students

<u>NAME</u>	<u>PERCENT SUPPORTED</u>	Discipline
B. Mills-Dadson	0.10	
G. Kumaran	0.15	
L. Sripragash	0.25	
ABS Islam	0.35	
K. Asamene	0.15	
FTE Equivalent:	1.00	
Total Number:	5	

Names of Post Doctorates

<u>NAME</u>	<u>PERCENT SUPPORTED</u>
K. Asamene	0.50
Hardik Vagh	0.50
FTE Equivalent:	1.00
Total Number:	2

Names of Faculty Supported

<u>NAME</u>	<u>PERCENT SUPPORTED</u>	National Academy Member
Mannur J. Sundaresan	0.08	
Albert Esterline	0.05	
FTE Equivalent:	0.13	
Total Number:	2	

Names of Under Graduate students supported

<u>NAME</u>	<u>PERCENT SUPPORTED</u>	Discipline
Gene Warwick	0.10	Mechanical Engineering
FTE Equivalent:	0.10	
Total Number:	1	

Student Metrics

This section only applies to graduating undergraduates supported by this agreement in this reporting period

The number of undergraduates funded by this agreement who graduated during this period: 0.00

The number of undergraduates funded by this agreement who graduated during this period with a degree in science, mathematics, engineering, or technology fields:..... 0.00

The number of undergraduates funded by your agreement who graduated during this period and will continue to pursue a graduate or Ph.D. degree in science, mathematics, engineering, or technology fields:..... 0.00

Number of graduating undergraduates who achieved a 3.5 GPA to 4.0 (4.0 max scale):..... 0.00

Number of graduating undergraduates funded by a DoD funded Center of Excellence grant for Education, Research and Engineering:..... 0.00

The number of undergraduates funded by your agreement who graduated during this period and intend to work for the Department of Defense 0.00

The number of undergraduates funded by your agreement who graduated during this period and will receive scholarships or fellowships for further studies in science, mathematics, engineering or technology fields:..... 0.00

Names of Personnel receiving masters degrees

NAME

G. Kumaran

ABS Islam

Total Number: 2

Names of personnel receiving PHDs

NAME

K. Asamene

Travis Whitlow

L. Spragash -summer 2015

Total Number: 3

Names of other research staff

NAME

PERCENT SUPPORTED

FTE Equivalent:

Total Number:

Sub Contractors (DD882)

Inventions (DD882)

Scientific Progress

Technology Transfer

None

Final Report
AMSRD-ARL-RO-SI Proposal Number: 60562-EG-REP

PROGNOSTIC HEALTH MANAGEMENT OF DOD ASSETS

Mannur J. Sundaresan, PI, Department of Mechanical Engineering
Albert Esterline, Investigator, Computer Science
North Carolina A&T State University
Greensboro, NC 27411

Submitted to

**Dr. Samuel Stanton
U. S. Army Research Office
Research Triangle Park, NC 27709-2211**

June, 2015

CONTENTS

SUMMARY OF ACCOMPLISHMENTS	8
PART 1: CHARACTERIZATION OF ACOUSTIC EMISSION EVENTS FROM DAMAGE IN COMPOSITES.....	12
Abstract	12
1.1 Introduction	12
1.2 Experiments.....	13
1.2.1 Test specimens	13
1.3 Results and discussion.....	14
1.3.1 AE Features and wavelet transform	15
1.4 Summary	17
References	18
PART 2: CLUSTERING OF FIBER BREAK RELATED EVENTS IN CARBON FIBER REINFORCED POLYMER COMPOSITES USING ACOUSTIC EMISSION	19
Abstract	19
2.1 Introduction	19
2.2 Experimental	21
2.3 Methodology	21
2.4 Results	23
2.4.1 AE parameters analysis	23
2.4.2 Correlation of AE signals.....	25
2.4.3 Location of clusters	27
2.5 Conclusion.....	29
References	29
PART 3: INFLUENCE OF ATTENUATION ON ACOUSTIC EMISSION SIGNALS IN CARBON FIBER REINFORCED POLYMER PANELS	31
Abstract	31

3.1 Introduction	31
3.2 Experiments to determine material related attenuation as function of mode and frequency.....	33
3.3 Experimental results	33
3.3.1 Identification of A_0 and S_0 modes.....	34
3.3.2 Dispersion curves of the laminates	34
3.3.3 Calculation of attenuation coefficients.....	35
3.3.4 Attenuation coefficients for the CFRP panels.....	36
3.3.5 Discussion of experimental results.....	39
3.4 Illustration of effect of attenuation on acoustic emission waveforms.....	40
3.4.1 Finite element simulations of AE signals.....	40
3.4.2 Different attenuation mechanisms and AE signals	42
3.5 Summary and conclusion	44
References	45
PART 4: CORRELATION BASED FATIGUE CRACK CHARACTERIZATION IN ALUMINUM	47
Abstract	47
4.1 Introduction	47
4.2 Experiments.....	48
4.1.1 Test setup	48
4.1.2 Test procedure.....	49
4.3 Results and discussion.....	50
4.3.1 Fatigue crack growth.....	50
4.3.2 Acoustic emission behavior	51

4.3.3 Evolution of waveforms with crack growth.....	53
4.4 Summary and conclusion	57
References	57
PART 5: NUMERICAL MODEL OF ACOUSTIC EMISSION GENERATION FROM CRACK EXTENSIONS	59
Abstract	59
5.1 Introduction	59
5.2 Finite element source function analysis	59
5.3 Advanced FEM models to simulate crack growth	64
5.4 Crack propagation modeling by element deletion.....	65
References	66
PART 6 SHEAR HORIZONTAL WAVE DETECTION AND ANALYSIS IN FATIGUE CRACK GROWTH RELATED ACOUSTIC EMISSION SIGNALS	68
Abstract	68
6.1 Introduction	68
6.2 Numerical analysis	70
6.3. Experimental setup.....	72
6.3.1 Simulated experiment.....	72
6.3.2 Fatigue test	73
6.4. Results and discussion.....	74
6.4.1 Simulated results	74
6.4.2 Fatigue test results.....	75
6.5. Conclusion.....	78
References	78
PART 7 ANALYSIS OF EXPERIMENTALLY GENERATED FRICTION RELATED ACOUSTIC EMISSION SIGNALS	80

Abstract	80
7.1 Introduction	80
7.2 Experimental test setup	82
7.2.1 Test fixture	82
7.2.2 AE instrumentation	84
7.2.3 Test procedure	85
7.3 Results and discussion	86
7.3.1 Surface roughness of contact surfaces	86
7.3.2 Stick-slip and acoustic emission events	87
7.3.3 Waveforms corresponding to lead-break	89
7.3.4 Friction related waveforms	90
7.3.5 Crack related waveforms	91
7.4 Characterization of the friction related acoustic emission waveforms	93
7.4.1 Effect of surface roughness	93
7.4.2 Effect of sliding velocity	95
7.4.3 Effect of normal pressure	96
7.5 Friction parameters and AE signal characteristics	97
Summary and conclusion	97
References	98
 PART 8: MACHINE LEARNING TECHNIQUES FOR STRUCTURAL HEALTH MONITORING	 100
Abstract	100
8.1 Introduction	100
8.2 Previous Work in machine learning for	102

8.3 Structural health monitoring.....	102
8.4 Approach	103
8.5 Results	104
4.5.1 Supervised-Learning Results	105
4.5.2 Unsupervised-Learning Results	106
8.6 Conclusion.....	108
References	109
 PART 9: A MULTIAGENT-BASED STRUCTURAL HEALTH MONITORING SYSTEM	
111	
Abstract	111
9.1 Introduction	111
9.2 A prototype for handling datastream.....	112
9.3 A prototype with hierarchy of monitor agents	114
References	117

SUMMARY OF ACCOMPLISHMENTS

Part 1: Composite materials experience complex evolution of damage even under static loading conditions. These damage events are associated with acoustic emission signals and such events have been extensively studied in the past to identify the different types of failure modes. A set of cross-ply and quasi-isotropic coupon specimens were instrumented with a configuration of sensors that are likely to preserve the acoustic emission features. These specimens were then tested under quasi-static tensile load to failure. Damage events such as matrix cracks, delamination, and scattered fiber breaks occurred throughout the loading cycles. Typically, several tens of thousands of acoustic emission events were recorded during each of these coupon tests. Features of acoustic emission signals corresponding to different types of damage events were examined. These include features such as frequency content and duration. The features were further analyzed to relate acoustic emission signals with likely failure modes based on the stress levels in the laminates. In addition, features that are indicators of the static strength in the presence of the accumulated damage are also examined. Based on these analyses the features of critical damage events are identified.

Part 2: The objective of this paper is to develop a technique capable to providing timely warning of the onset of critical damage events that precede the catastrophic failure of composite specimens. The sequential failure of 10 or more adjacent fiber breaks are known to trigger the final fracture of composite structural elements. In this paper, the detection of the formation of such critical clusters of fiber breaks among the millions of damage events that include matrix cracks, delamination, and individual fiber breaks, is shown to be feasible through statistical analysis of acoustic emission waveforms.

Acoustic emissions released during static loading of $[0/90]_{3S}$ cross-ply and $[+45/90/-45/0]_{2S}$ quasi-isotropic specimens were examined in detail for a large number of specimens. Matrix cracks, delaminations, and scattered fiber breaks occurred throughout the loading cycle, attempts to relate the features of acoustic emission signals such as amplitudes, frequency content, and duration were not successful. The focus was turned to isolating acoustic emission signals from the critical clusters of fiber breaks. The analysis presented here is based on the hypothesis that nearly collocated and similar microscopic failure events will result in identical acoustic emission waveforms. Since AE waveforms are determined by relative location of the source with respect to the sensor as well as the intervening medium, AE signals from members of a cluster, that occur in close succession, will have identical waveforms. AE waveforms from each group are expected to have a unique signature.

This hypothesis was tested on a number of cross-ply and quasi-isotropic specimens and groups of nearly identical AE signals were found to follow each other after 85% of ultimate load, and their numbers were found to increase exponentially with further increase in load. The tens of thousands of AE waveforms recorded for each specimen were analyzed using cross correlation to isolate groups within which signals were identical. On the average, the final catastrophic failure of the specimen followed immediately after a group in which 15 identical waveforms were seen.

For most specimens, the location of final failure coincided with the location from which such identical AE signals were received.

Part 3: Influence of attenuation on acoustic emission (AE) signals in Carbon Fiber Reinforced Polymer (CFRP) crossply and quasi-isotropic panels is examined in this paper. Attenuation coefficients of the fundamental antisymmetric (A_0) and symmetric (S_0) wave modes were determined experimentally along different directions for the two types of CFRP panels. In the frequency range from 100 kHz to 500 kHz, the A_0 mode undergoes significantly greater changes due to material related attenuation compared to the S_0 mode. Moderate to strong changes in the attenuation levels were also noted with propagation directions. Such mode and frequency dependent attenuation introduces major changes in the characteristics of AE signals depending on the position of the AE sensor relative to the source. Results from finite element simulations of a microscopic damage event in the composite laminates are used to illustrate attenuation related changes in modal and frequency components of AE signals.

Part 4: The relationship between characteristic features of acoustic emission (AE) signals and crack growth in Aluminum panel is examined in this paper. AE signals from fatigue crack growth in an Al 6061 plate with edge notch were collected by means of wideband AE sensors. Distributions of cumulative and individual characteristic features of the signals were evaluated. The signal waveforms were correlated among each other to identify features which were sensitive to crack growth. It was found that the amplitude and duration features were indicative of changes in the crack growth rate. The correlations among the waveforms indicated that the amplitudes of the antisymmetric (A_0) wave components of the signal waveforms increase as the crack length increases. Such characterizations of crack related signals are useful in AE based structural health monitoring applications.

Part 5: The objective of the work performed under this section is to better understand important aspects of AE signal generation, propagation, and detection, so as to better relate AE parameters with fatigue crack growth in critical aircraft structures. We analyze the characteristics of crack related signals in thick and complex structures and develop models that accurately capture the physics of AE signal generation during incremental crack growth.

Part 6: The article demonstrates an ab-initio configuration of piezoelectric sensors to capture shear horizontal components of the acoustic emission waveform. The acoustic emissions from simulated crack growth and incremental crack growth in a cyclically loaded aluminum panel were detected by various acoustic emission sensors. Thereby, the devised sensor performance was assessed in comparison to other bonded piezoelectric sensors and resonant frequency acoustic emission sensors. Variation of the waveforms as a function of the location of the sensor with respect to the source event was considered. Additionally, advantages of Horizontal-shear wave above A_0 and S_0

are discussed to show the need of engineered sensors sensitive to detect shear horizontal waveform related to acoustic emission signals.

Part 7: Acoustic emission signals generated by sliding friction between two flat steel surfaces are characterized. A test fixture to simulate the reciprocating motion between the two surfaces under controlled conditions is developed. Sliding friction under several combinations of surface roughness, relative velocity, and normal pressure was examined. Wideband AE sensors and instrumentation were used for acquiring and analyzing the acoustic emission signals. Acoustic emission events occurred primarily during the slip portion of the stick-slip cycles. AE waveform features obtained during these experiments were indicative of the tribological conditions. Frequency components in excess of 700 kHz were seen during these experiments. The characteristics of the experimentally observed acoustic emission signals were in general agreement with earlier numerical predictions. Friction related acoustic emission signals were distinguishable from those from other sources such as fatigue crack growth. The characterization of friction related acoustic emission signals is likely to be of value in many tribological and structural health monitoring applications.

Part 8: We report on work that is part of the development of an agent-based structural health monitoring system. The data used are acoustic emission signals, and we classify these signals according to source mechanisms, those associated with crack growth being particularly significant. The agents are proxies for communication- and computation-intensive techniques and respond to the situation at hand by determining an appropriate constellation of techniques. It is critical that the system have a repertoire of classifiers with different characteristics so that a combination appropriate for the situation at hand can generally be found. We use unsupervised learning for identifying the existence and location of damage but supervised learning for identifying the type and severity of damage. The supervised learning techniques investigated are support vector machines (SVM), naive Bayes classifiers, and feed-forward neural networks (FNN). The unsupervised learning techniques investigated are k-means (with k equal to 4, 5, and 6) and self-organizing maps (SOM, with 4, 5, and 6 output neurons). For each technique except SOM, we tested versions with and without principal component analysis (PCA) to reduce the dimensionality of the data. We found significant differences in the characteristics of these machine learning techniques, with a general trade-off between accuracy and fast classification runtime. This trade-off can be exploited by the agents in finding appropriate combinations of classification techniques. The approach followed here can be generalized for exploring the characteristics of machine-learning techniques for monitoring various kinds of structures.

Part 9: The overall architecture involves motes (battery-powered devices with processors, memory, attached sensors. And wireless communication capability) that feed data streams to workstations on which a multiagent system allocates resources to interpret and fuse the data. Agent services are made available as Web services, resulting in an end-to-end architecture, extending

from the sensors to the users consuming the information to support decisions. Prototypes have been developed for interpreting individual datastreams, for hierarchical integration of monitoring agents, and for publishing status and alerts on the Web and rendering them on a user's "dashboard."

PART 1: CHARACTERIZATION OF ACOUSTIC EMISSION EVENTS FROM DAMAGE IN COMPOSITES

Abstract

Composite materials experience complex evolution of damage even under static loading conditions. These damage events are associated with acoustic emission signals and such events have been extensively studied in the past to identify the different types of failure modes. A set of cross-ply and quasi-isotropic coupon specimens were instrumented with a configuration of sensors that are likely to preserve the acoustic emission features. These specimens were then tested under quasi-static tensile load to failure. Damage events such as matrix cracks, delamination, and scattered fiber breaks occurred throughout the loading cycles. Typically, several tens of thousands of acoustic emission events were recorded during each of these coupon tests. Features of acoustic emission signals corresponding to different types of damage events were examined. These include features such as frequency content and duration. The features were further analyzed to relate acoustic emission signals with likely failure modes based on the stress levels in the laminates. In addition, features that are indicators of the static strength in the presence of the accumulated damage are also examined. Based on these analyses the features of critical damage events are identified.

1.1 Introduction

The useful life of composite components is affected by damage progressing in different failure modes. These modes include fiber breaking, matrix cracking, and delamination. Unlike monolithic materials, the damage progression is not characterized by growth of a single crack initiating from highly stressed sections of the member. The progression of damage in composites is characterized by distributions of the different failure modes over the dimensions of the laminates [1].

Some of these failure modes have substantial effect on the strength and durability of composite components, while others are considered non-critical [2]. These failure modes tend to occur at different stages of a loading cycle. At lower load levels, matrix cracks appear over the entire volume of the specimen, affecting the stiffness of a laminate. As the load increases further, delaminations and fiber breaks occur. The accumulation of these two modes is likely to lead to the final failure of the component.

Any sudden structural change in the composite laminates such as matrix cracking and fiber breaks produces stress waves which propagate in the structure. These waves, i.e. acoustic emissions (AE), depend on the type of source mechanism and also provide information regarding the type of failure mode. The different failure modes in composites are likely to result in AE signals with different features.

AE data obtained from failure processes under different kinds of tests can be analyzed to differentiate the mechanisms involved. Several researchers used this advantage to investigate the different mechanisms of failure using AE data. An extensive review [3] highlights three major areas of AE research related to composite materials. These include interface studies in single fiber

composites, damage evolution, and detection of failure mechanisms. A study of damage accumulation in quasi-statically loaded composite specimens using wavelet analysis of acoustic emission signals was used to obtain frequency and time information related to different failure mechanisms [4]. Features such as amplitude, number of AE events, cumulative AE energy and peak frequency have also been used for clustering AE data obtained from tensile tests [5]. Debonds between fiber and matrix material has also been characterized using the amplitude and frequency of the signals [6]. An attempt has also been made to examine evolution of microdamage in composites experimentally using a combination of AE classification and multi-parameter filtering [7]. Various damage mechanisms which occur during buckling of a composite laminate has also been studied. Two main damage mechanisms believed to be matrix cracking and delamination were indicated by three classification algorithms implemented by the authors. Ultrasonic C-Scan and digital image correlation were also implemented [8].

This paper examines the possibility of identifying the failure mode from the distinct features of the resulting acoustic emission signal. The details of the experimental works, results and discussion of the results are presented in the following sections.

1.2 Experiments

Tensile test specimens were cut from carbon fiber reinforced plates according to ASTM Standard D3039. These specimens were subjected to quasi-static loading up to fracture. Thousands of AE events were generated by these tests. These signals were later analyzed to identify clusters corresponding to failure mechanisms.

1.2.1 Test specimens

A total of two quasi-isotropic and two cross-ply specimens were used. The stacking sequences for the cross-ply and the quasi-isotropic laminates were $[0/90]_{3s}$ and $[+45/90/-45/0]_{2s}$, respectively. The dimensions for the tension test specimens from both types of specimens for the cross-ply and quasi-isotropic laminates were $300 \text{ mm} \times 25 \text{ mm} \times 1.8 \text{ mm}$ and $300 \text{ mm} \times 25 \text{ mm} \times 2.4 \text{ mm}$, respectively. The fiber volume ratio for the specimens was determined to be 0.65. Table I shows the loads at which fracture occurred in each of the specimens.

Table 1. Loads at which fracture occurred

Test	Load at failure ($\times 10^3 \text{ N}$)
Q6	41.8
Q7	39.1
CP1	43.5
CP3	39.4

The influence of the propagation medium on the detected signals can affect the success of relating the acoustic emission signals to the type of the source giving rise to these signals. Recently the influence of mode and frequency dependent attenuation of acoustic emission signals propagating in composite laminates were examined in detail [9]. Based on this information, the

specimens were instrumented with a configuration of sensors that are likely to preserve the acoustic emission features. Four rectangular piezoelectric (PZT) wafers were bonded to the surface of the plate to detect the AE signals originating from the various failure modes. These sensors were capable of frequency response in excess of 1.5 MHz.

Because of the dense array of sensors used, it was possible to detect the high frequency components of AE signals which otherwise would have been lost because of attenuation. It was also feasible to locate the AE sources better with these sensors. The layout of the sensors is shown in figure 1. The signals from the transducers were amplified by Physical Acoustics Corporation PAC 2/4/6 preamplifiers at 40 dB gain and 50 kHz high pass filters. A 40 dB threshold was set while acquiring the AE signals. The signals from the four channels were recorded by PCI-2 data acquisition system at a rate of 10×10^6 samples/second. The waveforms were recorded for a length of 512 μ s and contained a total of 5120 data points per waveform.

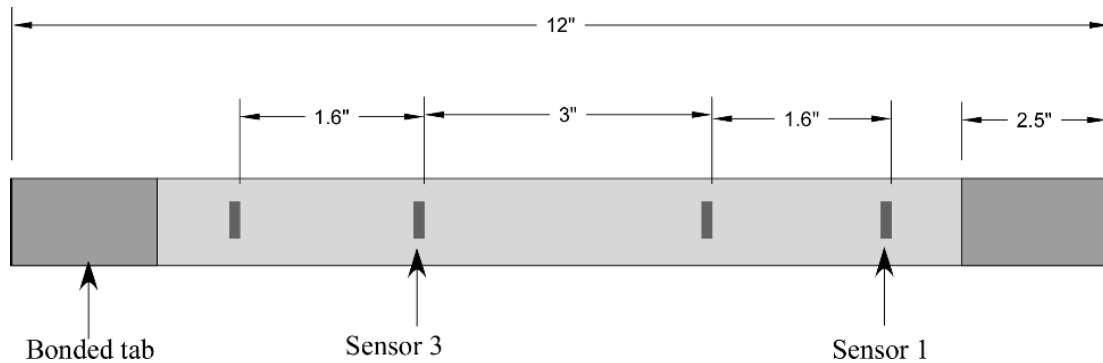


Figure 1. Sensor arrangement in the specimens

1.3 Results and discussion

The number of AE signals acquired during the loading sequence varied from one test to another. Typical acquisition rates of a channel for the quasi-isotropic and the cross-ply coupon tests are shown in figure 2. The number of detected hits varies widely depending on the relative location of the damage events and the sensors. On the average, 25,000 waveforms are sensed by the 4 channels. The sensor closest to the locations of most of the damage events picks 30 to 40% of the total number of hits.

In quasi-isotropic specimens, AE event rate or the number of AE signals captured for a unit load increment, was relatively low until about 85% of the maximum load, and beyond this point, event rate increased exponentially. The cross-ply tests showed initially had a high AE rate followed by modest rate. During the last 15% of the loading cycle there was an exponential increase in the AE rate. Physical observation of the failure shows more delamination in the quasi-isotropic laminates as compared to the cross-ply specimen. Figure 3 shows images of the cross-ply and quasi-isotropic specimens after failure.

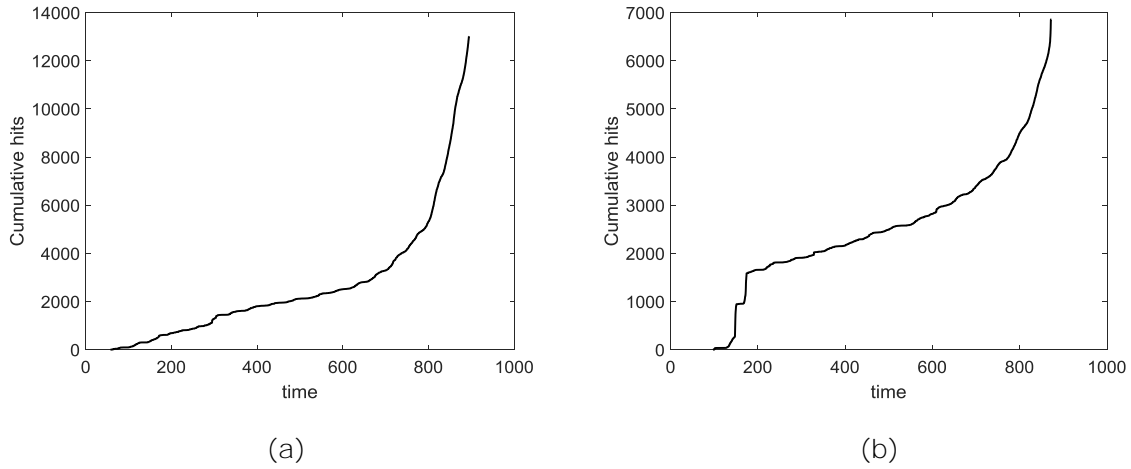


Figure 2. Cumulative AE hits for quasi-isotropic specimen (a) and cross-ply specimen (b)

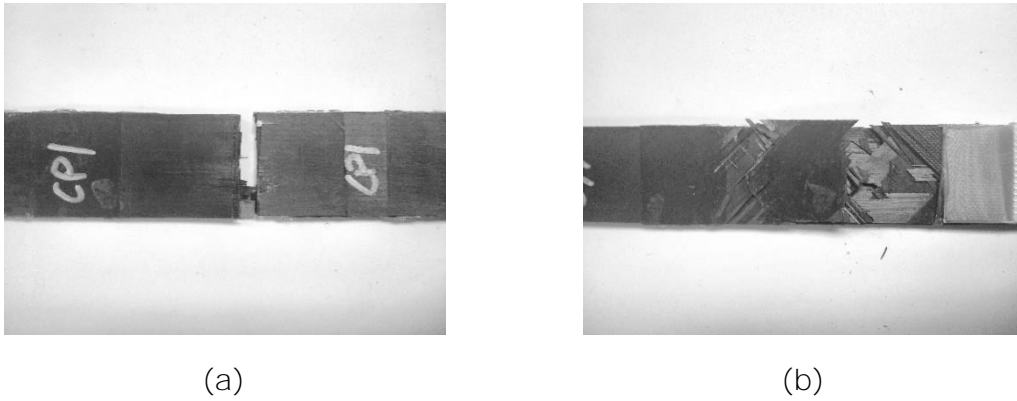


Figure 3. Failure region of (a) Cross-ply specimen (b) Quasi-isotropic specimen

1.3.1 AE Features and wavelet transform

The frequency contents of the AE signals were identified by wavelet diagrams obtained using AGU Vallen wavelet software. The signals were located to ensure that signals from the failure region were duly analyzed. As observed from the physical examination of failed specimens, the failure mechanism for the cross-ply specimens was predominantly fiber fracture and that for the quasi-isotropic specimens was a mix of delamination and fiber break, with delamination being more dominant. These respective failure mechanisms are expected of these layups.

Results of analyzing the wavelet transforms of signals from the failure zone of the tests showed some relation between the types of signals and the observed failure mechanisms. Matrix cracking was detected in both specimens early on in the loading sequence during the early sharp rise in AE events acquisition rate (up to 20% of the load level). The signals related to matrix cracks tend to have relatively low frequency components and dominant antisymmetric wave propagation

components. The amplitudes were relatively large. Figure 4 shows a waveform and wavelet transform of such a signal obtained during the early stages of the loading cycle.

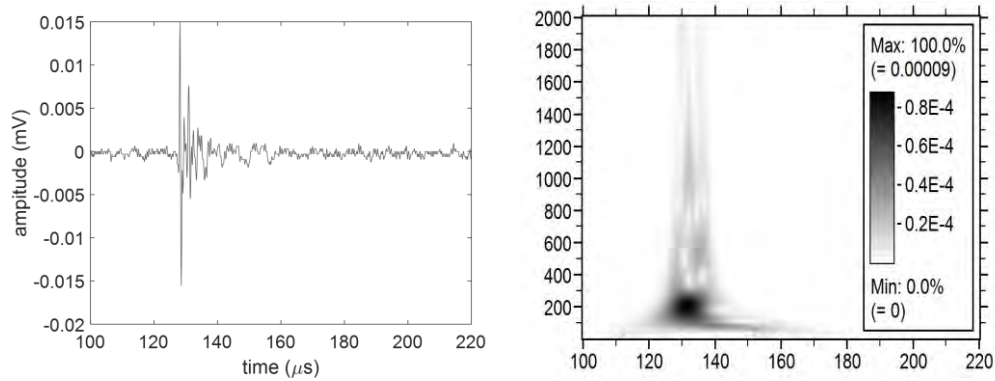


Figure 4. Wavelet transform of signal occurring at 50% of failure load in a cross-ply specimen , likely from a matrix crack.

A very small fraction of the signals recorded in cross-ply specimens, around 20% of final fracture had features similar to the waveform shown in figure 5. In comparison, most of the signals generated above 85% of final fracture load, were similar to the one shown in figure 6. Both of these signals have frequency components in excess of 1.5 MHz and duration of roughly 25 to 50 μs. The short duration and high frequency content in these signals are likely to have resulted from fiber breaks. The signals, in figure 6, generated at high load levels have much larger amplitudes as those, in figure 5, as expected.

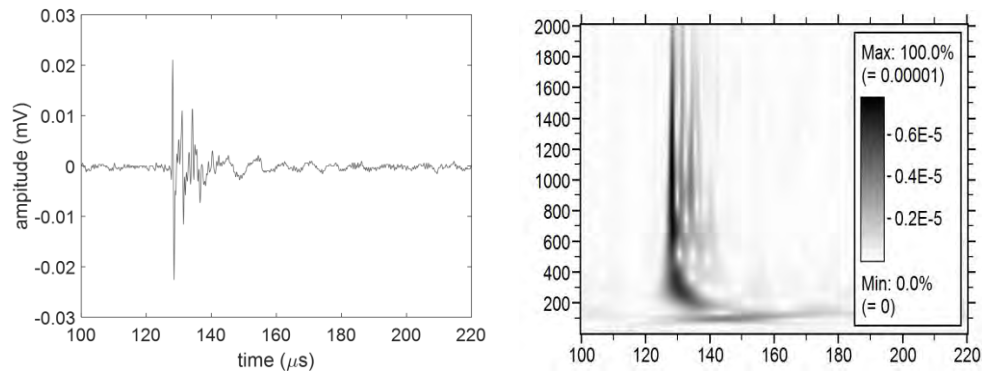


Figure 5. Wavelet transform of signal from early fast AE acquisition rate – early fiber break source

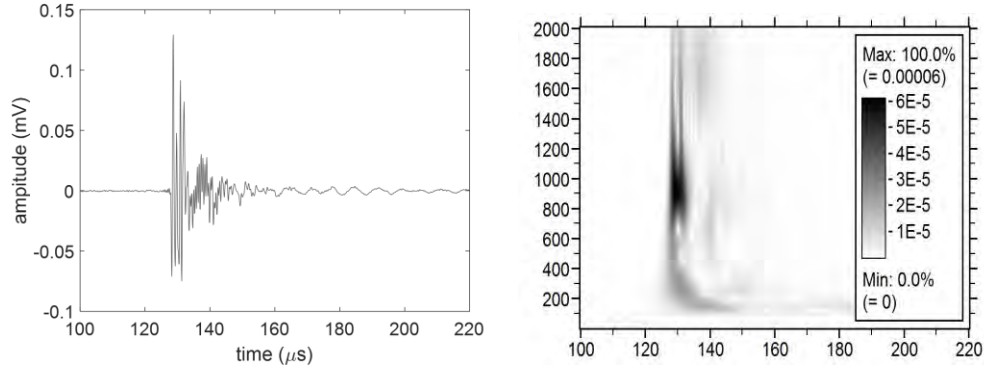


Figure 6. Wavelet transform of signal from near failure – late fiber break source

In tests on quasi-isotropic specimens, there were a significant number of long duration, low frequency signals. The distinctive feature of these signals is a strong presence of antisymmetric components, as seen in figure 7. These signals are likely related to delaminations which occurs over a relatively larger area/volume.

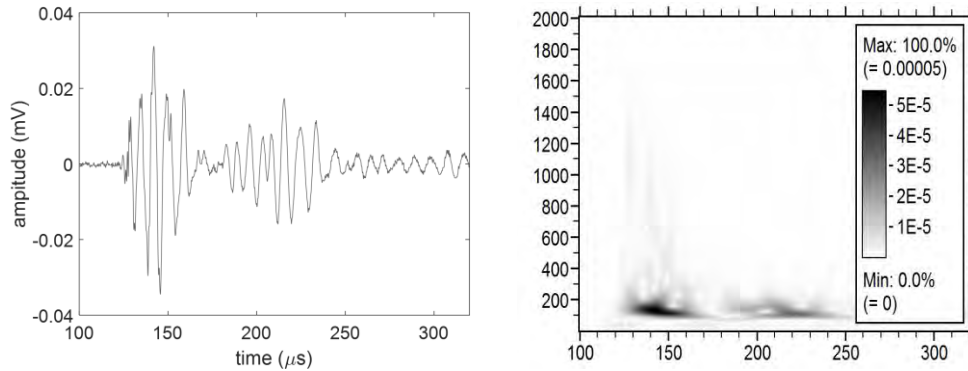


Figure 7. Wavelet transform of signal from zone near failure –corresponding to delamination

1.4 Summary

In this paper, the features of AE signals were analyzed and related to the damage mechanism from which the signals originate. The analysis showed that critical events like delamination and fiber breaks occur close to the final failure. Delamination is characterized by low frequency, long duration signals dominated by anti-symmetric mode. Such signals were found in greater number in quasi-isotropic specimens than in the cross-ply specimens. Fiber breaks are characterized by short duration, high frequency signals with almost no anti-symmetric component.

Non-critical damage events related to matrix cracks occur in the early life of the coupon. AE from matrix crack growth have low frequency signals often with anti-symmetric components. These results can help in identifying failure modes during AE based structural health monitoring of composite materials.

References

- [1] B. Harris, "Fatigue in composite," *CRC/WP*, vol. 3, 2003.
- [2] K. L. Reifsnider and S. W. Case, "Damage tolerance and durability of material systems," *Damage Tolerance and Durability of Material Systems*, by Kenneth L. Reifsnider, Scott W. Case, pp. 435. ISBN 0-471-15299-4. Wiley-VCH, April 2002., vol. 1, 2002.
- [3] I. M. De Rosa, C. Santulli, and F. Sarasini, "Acoustic emission for monitoring the mechanical behaviour of natural fibre composites: a literature review," *Composites Part A: Applied Science and Manufacturing*, vol. 40, pp. 1456-1469, 2009.
- [4] A. Bussiba, M. Kupiec, R. Piat, and T. Böhlke, "Fracture characterization of C/C composites under various stress modes by monitoring both mechanical and acoustic responses," *Carbon*, vol. 46, pp. 618-630, 2008.
- [5] T. Loutas and V. Kostopoulos, "Health monitoring of carbon/carbon, woven reinforced composites. Damage assessment by using advanced signal processing techniques. Part I: Acoustic emission monitoring and damage mechanisms evolution," *Composites science and technology*, vol. 69, pp. 265-272, 2009.
- [6] W. Haselbach and B. Lauke, "Acoustic emission of debonding between fibre and matrix to evaluate local adhesion," *Composites Science and Technology*, vol. 63, pp. 2155-2162, 2003.
- [7] Y. A. Dzenis and J. Qian, "Analysis of microdamage evolution histories in composites," *International Journal of Solids and Structures*, vol. 38, pp. 1831-1854, 3// 2001.
- [8] J. P. McCrory, S. K. Al-Jumaili, D. Crivelli, M. R. Pearson, M. J. Eaton, C. A. Featherston, *et al.*, "Damage classification in carbon fibre composites using acoustic emission: A comparison of three techniques," *Composites Part B: Engineering*, vol. 68, pp. 424-430, 1// 2015.
- [9] K. Asamene, L. Hudson, and M. Sundaresan, "Influence of attenuation on acoustic emission signals in carbon fiber reinforced polymer panels," *Ultrasonics*, vol. 59, pp. 86-93, 2015.

PART 2: CLUSTERING OF FIBER BREAK RELATED EVENTS IN CARBON FIBER REINFORCED POLYMER COMPOSITES USING ACOUSTIC EMISSION

Abstract

The objective of this paper is to develop a technique capable to providing timely warning of the onset of critical damage events that precede the catastrophic failure of composite specimens. The sequential failure of 10 or more adjacent fiber breaks [1-6] are known to trigger the final fracture of composite structural elements. In this paper, the detection of the formation of such critical clusters of fiber breaks among the millions of damage events that include matrix cracks, delamination, and individual fiber breaks, is shown to be feasible through statistical analysis of acoustic emission waveforms.

Acoustic emissions released during static loading of $[0/90]_{3S}$ cross-ply and $[+45/90/-45/0]_{2S}$ quasi-isotropic specimens were examined in detail for a large number of specimens. Matrix cracks, delaminations, and scattered fiber breaks occurred throughout the loading cycle, attempts to relate the features of acoustic emission signals such as amplitudes, frequency content, and duration were not successful. The focus was turned to isolating acoustic emission signals from the critical clusters of fiber breaks. The analysis presented here is based on the hypothesis that nearly collocated and similar microscopic failure events will result in identical acoustic emission waveforms. Since AE waveforms are determined by relative location of the source with respect to the sensor as well as the intervening medium, AE signals from members of a cluster, that occur in close succession, will have identical waveforms. AE waveforms from each group are expected to have a unique signature.

This hypothesis was tested on a number of cross-ply and quasi-isotropic specimens and groups of nearly identical AE signals were found to follow each other after 85% of ultimate load, and their numbers were found to increase exponentially with further increase in load. The tens of thousands of AE waveforms recorded for each specimen were analyzed using cross correlation to isolate groups within which signals were identical. On the average, the final catastrophic failure of the specimen followed immediately after a group in which 15 identical waveforms were seen. For most specimens, the location of final failure coincided with the location from which such identical AE signals were received.

2.1 Introduction

Damage progression in carbon fiber reinforced composites is known to occur in stages and involves several failure mechanisms (e.g., matrix cracking, fiber breakage, and delamination). The presence of certain mechanisms may give an indication on where along the failure process the material currently is. Each mechanism has a unique physical process in terms of duration and energy release rate which should produce distinct AE signals. The subtle differences in AE signals have been a focus for distinguishing the failure modes. Liu [7] and Mechraoui [8] studied the various failure mechanisms using primarily AE amplitude with each mechanism occupying a distinct amplitude range but noted that amplitude values will depend on the material system. Yu [9] looked at specific frequency values to monitor failure in carbon reinforced composite

specimens. Bussiba [10] showed that not only do the different failure modes generate unique frequencies but they also have noticeably different durations. Fiber breaks are very short duration events and are known to give rise to relatively high frequency content [11]. However, examining a given parameter may not provide sufficient information regarding the source [12] since the failure modes may occupy common parameter regimes.

The various failure modes have different effects on the integrity of the structure and can potentially be classified as either critical or non-critical damage. This ultimately depends on the make-up of the composite which dictates the failure process. Damage initiation and progression in fiber reinforced composites have been well studied in the past with several techniques utilizing micromechanics based models to predict the behavior of the material under certain load conditions. Ogi [13] developed a probabilistic model to predict transverse matrix crack in cross-ply panel and compared it to experimental results. Wharmby [14] related the transverse crack density to changes of the elastic modulus which is more drastic in the absence of 0° plies. It was noticed that the majority of the stiffness reduction occurred within the first 10% of the normalized life. Acoustic energy can also be a useful parameter to study damage progression. High energy events may signify significant damage growth which can be captured and characterized using acoustic emission techniques. Using cumulative AE energy was shown to agree well with C-scanning and microscopic analysis when monitoring damage accumulation [15]. Such methods have been shown to sufficiently capture the material behavior as long as the stress state information can be determined. However, there has not been a technique that focuses on identifying the onset of critical damage in real time. Even AE techniques, which attempt to distinguish between the different failure modes in real time, do not differentiate between non-critical and critical damage growth. For this study, critical damage is defined as that which indicates or precedes final failure.

Filtering out inconsequential signals not only allows for greater emphasis to be placed on important events but also addresses the data management issue associated with AE in unidirectional composite materials. Unidirectional composites are profuse emitter of acoustic emissions and can produce tens of thousands of signals during a simple coupon test. This can be counteracted by raising the trigger threshold to decrease the AE hit rate. Consequently, lower amplitude signals will be missed as a result. Under the assumption that critical damage signals start with low energy, ignoring lower amplitude signals may limit the ability to detect the early onset of critical damage growth. With a filter, all relevant signals across the entire amplitude spectrum can be analyzed and also stored for later processing if necessary. The volume of AE data generated during testing, primarily for fatigue, may restrict the acquisition parameters used or the test duration. Ultimately, this process is a balance between determining the minimum amplitude/energy of relevant signals and staying below the maximum number of signals capable of being analyzed by post-processing software.

This work utilizes a cross-correlation technique as a filter to discriminate between non-critical and critical damage in carbon fiber-reinforced polymer (CFRP) panels while accounting for relevant low energy signals. Cross-ply and quasi-isotropic specimens were cut from laminates developed at NASA Armstrong Flight Research Center. The layups of the laminates were designed

to resemble those of carbon fiber composites used in current aerospace structures. Damage evolution as it transitions from insignificant crack growth to meaningful damage was investigated using AE techniques.

2.2 Experimental

Each panel was made by stacking unidirectional tape to achieve a desired layup. After each lamina were positioned and vacuumed bagged, they were heated 2°F/min to 250°F, held at that temperature for one hour then cooled at room temperature. ASTM tension test standard D3039 was used to determine the dimension of each rectangular specimen which was 25 mm x 275 mm long. The gage length varied between 75 and 150 mm and piezo-electric wafer sensors were bonded adhesively on both ends of the gage section while ultrasonic transducers were attached outside the gage to function as guard sensors. The frequency responses for the PZT sensors and ultrasonic transducers were 100 to 700 kHz and 100 to 400 kHz, respectively. Wideband PAC 2/4/6 preamplifiers were used and the 40 dB setting was typically used for both static and fatigue tests. All AE data was recorded on a 4-channel PCI-2 AE system.

The specimens were loaded using a hydraulic testing machine. Quasi-static tests were done at a rate of 167 lbs/min to ensure a sufficient number of AE events would be captured to characterize the separate failure regions. Lead breaks were done to ensure each sensor had similar frequency responses and sensitivity. Also, the time of flight of signal from one sensor to the next can be measured and used to calculate the speed of sound (velocity) of the signal, which is useful in determining source location.

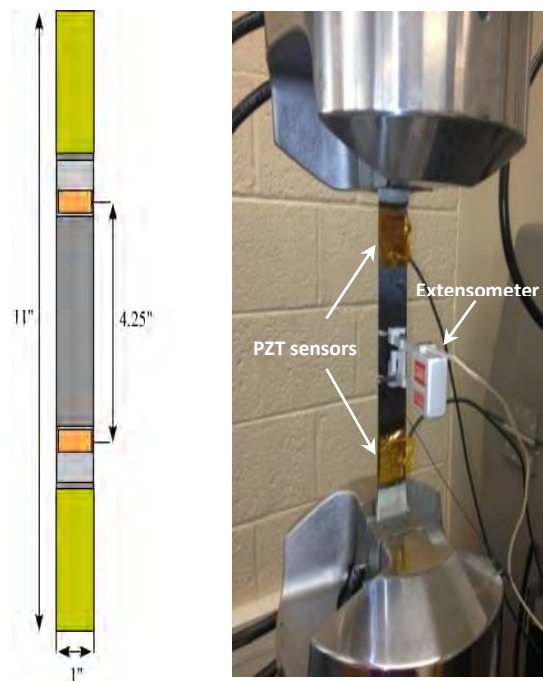


Figure 1. Tensile specimen dimensions (left), specimen during testing.

2.3 Methodology

Each static test is capable of generating tens of thousands of signals depending on parameters such as threshold value, sensor sensitivity, and failure process of the material. Several signal processing techniques can be used to filter and isolate various types of signals. This study utilized a cross-correlation to extract important signals based on the density of signals generated in a particular area over a set period of time. This approach relates an area where a high density of similar AE signals is being generated to critical localized damage growth. Localized damage growth is considered to be where a given source mechanism continuously grows or happens within a relatively small area or volume. In such case, that mechanism should produce repetitive signals as long as there has not been a drastic change in the medium. A focus is placed on critical localized damage, such as fiber breaks, that significantly reduces the strength of the component. It is known that a fiber breakage causes stress redistribution into neighboring fibers which may fail if their ultimate strength is exceeded [16]. These neighboring fibers simultaneously fail in groups, or i-plets, at high load [1, 3, 6]. This behavior has been captured in great detail using computed tomography [4]. Capturing the failure of these i-plets in terms of AE clusters can provide great insight on the damage state of the material in real-time. Also, given that composites may begin to fail in randomly, such a technique may be able to distinguish between separate localized damage areas.

The correlation process relies on raw waveform data captured by the individual sensors to determine location and various AE parameters (duration, frequency, energy, etc.). Typical AE software calculates such information but analyzing waveform data using MATLAB was found to be more sufficient. The cross-correlation technique used to compare separate data sets is shown below in Eqs. 1 and 2.

$$1) \quad R_{xy}(m) = E\{x_{n+m}y_n^*\} = E\{x_ny_{n-m}^*\}$$

$$2) \quad \hat{R}_{xy}(m) = \begin{cases} \sum_{n=0}^{N-m-1} x_{n+m}y_n^* & m \geq 0 \\ \hat{R}_{xy}^*(-m) & m < 0 \end{cases}$$

$$c(m) = \hat{R}_{xy}(m - N) \quad m = 1, 2, \dots, 2N - 1$$

If there are two continuous functions representing waveform data, x and y , there will be an expected value, E , resulting from comparing the two functions. The variable m is the lag or shift, and the output is the correlation array, c . Each correlation value corresponds to a lag value and the degree of how similar two waveforms are can be found by finding the maximum value of c . A visual representation of how this technique works is shown in Fig. 1. The first signal detected by each signal serves as the initial reference signal and the following signals that fall within a specified window are correlated to the reference. Signals that correlate at a high percentage are grouped with the reference signal to form a cluster. Clustered signals are removed from the data set and the remaining signals are shifted to fill the empty spaces and the next iteration of the process begins.

This “on-the-fly” technique uses real time data to monitor critical damage growth and has potential to be used in-situ.

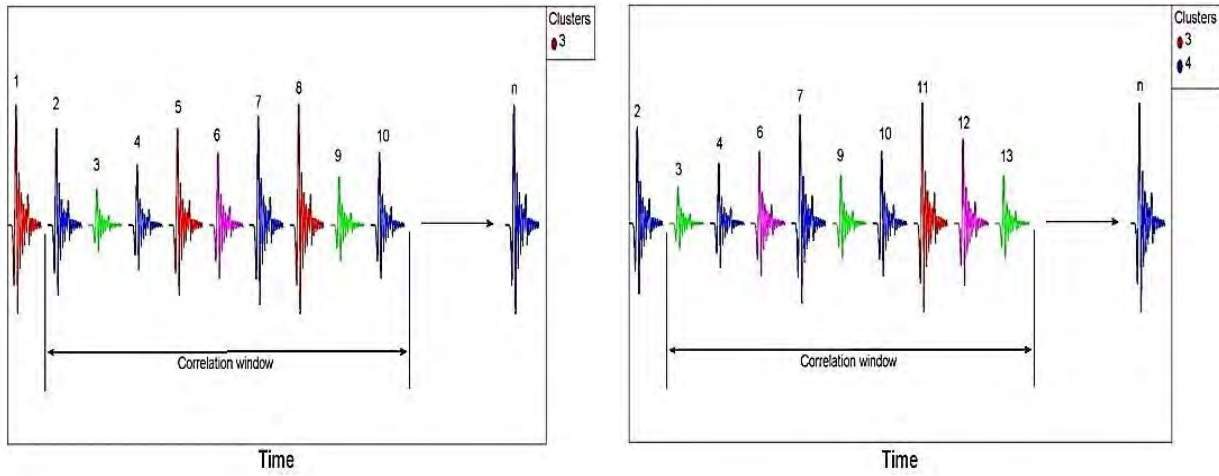


Figure 2. Schematic of clustering process.

Using correlation, the effects of the attenuation, dispersion, and other aspects of wave propagation can be minimize and taken into account. During the early onset of damage, successive signals that correlate at a high percentage may indicate localized damage growth and as the damage becomes more pronounced, individual signals from fiber breaks travel the same path for a finite period of time. The signals within this time window that correlate at or above a predetermined percentage are grouped into a cluster. Whereas most models require intrinsic knowledge about the state of the material to predict failure, here, the rate of cluster formation as well as cluster size was seen to be an indicator of critical damage for quasi-static tests.

2.4 Results

2.4.1 AE parameters analysis

The AE data generated during static loading for both the cross-ply and quasi-isotropic material can be seen below. Cumulative AE events vs stress plots can be seen in Fig. 3 and highlight the separate regions where matrix cracking, delamination, and fiber breaks occur at a high rate. Initially, a sudden increase in the number of events at low stress is seen due to failure of the matrix which generates a high rate of acoustic emissions. This behavior typically happens around 20-40% of the ultimate stress and saturate shortly after. Matrix cracks saturation is followed by an intermediate period characterized by minimal AE signal generation. At this point, the fibers are completely responsible for carrying load and the drastic increase of AE activity seen before failure is primarily associated with fiber breakage and delamination.

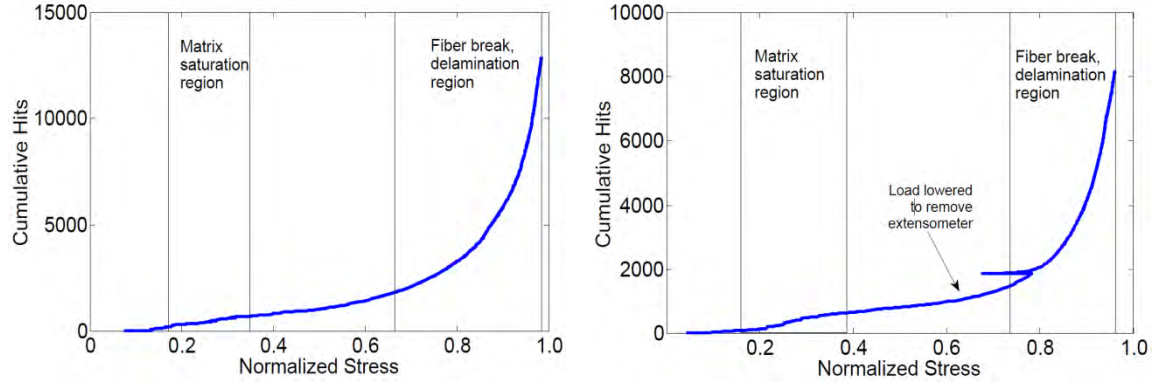


Figure 3. Cumulative AE hits vs stress for cross-ply (top) and quasi-isotropic (bottom).

The above cumulative AE plots follow the expected multi-stage failure process but do not show much difference between the two materials. Since the beginning and last regions contain extensive matrix cracking and fiber breaks, respectively, examining the AE parameters may provide information on the individual failure mechanisms. Splitting of the matrix occurs over a certain area and happens over a particular period of time whereas carbon fibers have a relatively smaller cross-sectional area and break almost instantaneously. This difference in source duration and energy release of the failure modes should generate unique signals in terms of the traditional AE parameters.

Below, the average frequency and duration plots of the individual AE events, shown as blue dots in Fig. 4. Ideally, matrix cracking and fiber breaks should generate very distinct signals but there is only a minimal difference in the frequency characteristics seen for the two regions. This is seen in both cross-ply and quasi-isotropic material. However, the later region for the cross-ply seems to have a slightly higher frequency centroid than the cross-ply material. Duration plots for both material as well as any other parameter plot provided very limited information on the damage development due to signals being affected by attenuation, dispersion, and scattering. The effects of attenuation and dispersion as a function of material properties and geometry have been well documented. However, the effects of attenuation and dispersion as a function of damage is not well understood because they depend on the amount of damage a signal encounters on its path to a sensor rather than the amount of overall damage.

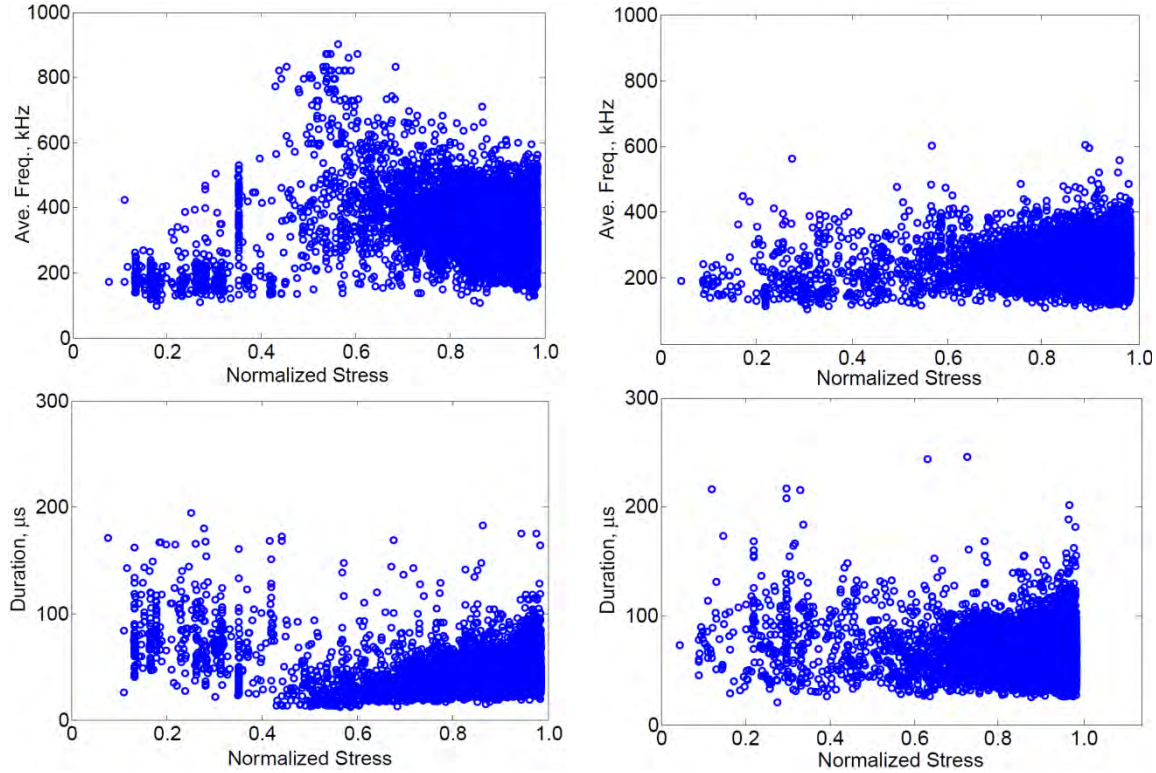


Figure 4. Average Frequency and Duration plots. cross-ply (left), quasi-isotropic(right).

2.4.2 Correlation of AE signals

Clustering of AE signals usually involves extracting parameters and forming groups or classes based on waveform characteristics. Some methods utilize un-supervised approaches that make use of amplitude or other traditional parameters as classification metrics [17-20]. The accuracy of such techniques depends on accurate measurement of distinguishing features while accounting for effects of wave propagation, which is heavily dependent on distance.

The proposed correlation technique took the same data that generated limited insight from a traditional AE parameter standpoint and extracted meaningful information in terms of critical damage growth. To account for the change in the propagating medium due to damage, a window was used to only analyze successive signals to find clusters. This windowing assumes that the material microstructure of a given signal path stays constant or exhibits insignificant change for a finite period of time or stress. The clusters plots using a 90% correlation value are shown in Fig. 5 and detail how various cluster sizes grow as a function of stress. Each line represents an individual cluster size.

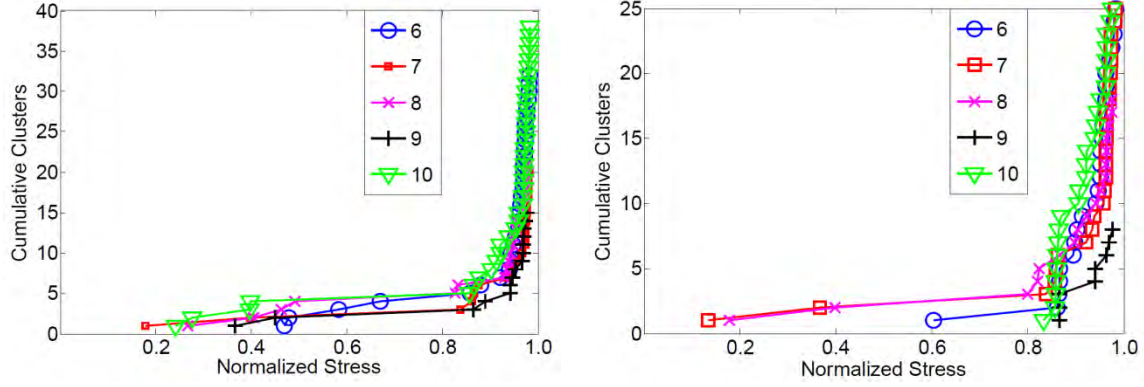


Figure 5. Cumulative cluster growth for cross-ply specimen: sensors1 and 2.

The most accurate and non-trivial way to accurately capture the fiber break phenomenon is to physically count the breaks using high resolution microscopy. Reifsneider and Jamison [1] manually observed fiber breakage in each ply of a cross-ply and unidirectional specimens using scanning electron microscopy (SEM). A specimen was loaded to a certain percentage of the ultimate stress, then unloaded and dissected, and the number of fiber breaks for given area (mm^2) was determined. This was done at multiple ultimate stress percentages. Figure 6 shows a comparison between these findings and the results of this work. The AE data is a cumulative plot of AE clusters that have a size of 10 or greater. After sifting through the data, it was determined that 10 was a consistent metric for a minimal cluster size.

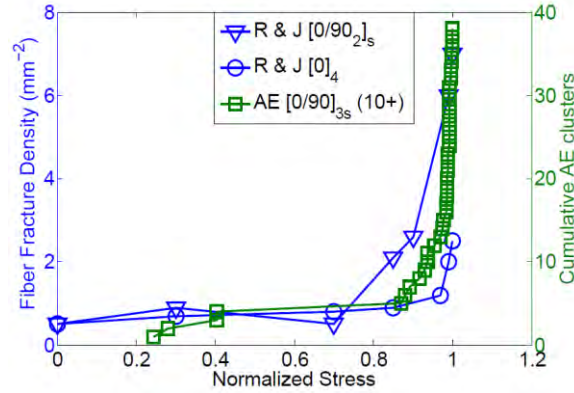


Figure 6. Comparison of SEM results and AE data

From the above plot, the trend of the AE data falls between the SEM data as expected since the lay-up of the AE specimen falls between the layup of the other two. Having such physical evidence can provide calibration and fine tuning of the AE data analysis, which will allow this behavior to be characterized without any labor intensive or computational heavy processes. With that being said, the ultimate comparison would involve the same specimen for AE measurement and SEM imaging.

The waveforms that make up the clusters were also examined and the AE features were studied. AE parameter analysis of clustered waveforms may provide information not noticeable when all AE data is analyzed. The frequency content of the reference waveform of each cluster was plotted with respect to **stress**, Fig. 7.

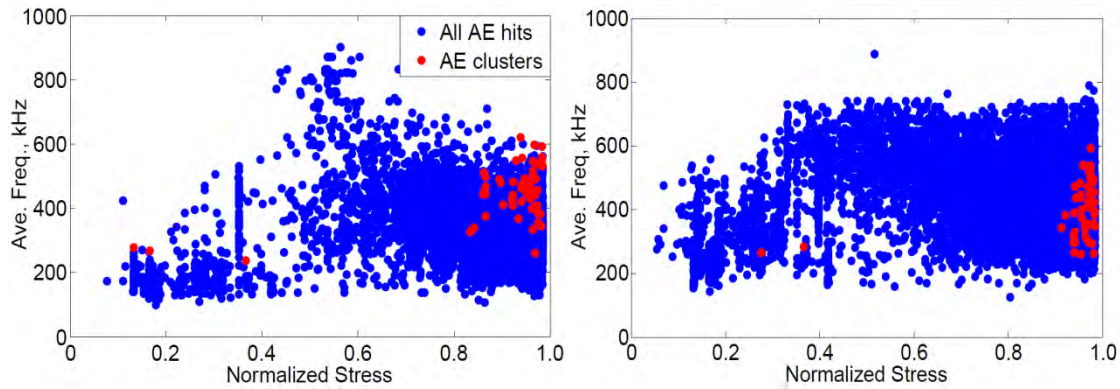


Figure 7. Average frequency of cluster signals (red) and all AE data: data from sensor near failure, away from failure.

In the above average frequency plots, the reference signals (red) are superimposed over all the AE data. Since the clusters are associated with localized damage growth resulting from fiber breakage, it is expected that the signals contain relatively higher frequency content. Theoretically, fiber breaks should generate much higher frequencies than what is shown in Fig. 7 but the PZT wafer sensors had an upper frequency limit around 700 kHz. Sensors having a broader frequency response can be used but the influence of attenuation on the signals seems to play a more significant role in the measurement of higher frequencies. Hence, the reference signals from a given sensor tend to occupy the upper frequency domain when failure occurs near or at that sensor.

2.4.3 Location of clusters

The process of identifying clusters started with understanding localized damage growth. In this section, the origin of AE signals is studied and determined. Location of AE events itself is a well-understood process and has been studied extensively. In the case of transient waves, individual sensors may be triggered by different parts of the same waveform. A detailed waveform analysis was done to mitigate this problem and help enhance source location of AE clusters.

Since clusters are composed of multiple signals, source location only applies to the reference waveform and the subsequent signals are assumed to have originated from the same location. The transient nature of the signals makes it difficult to get precise time of arrival measurements. The extensional mode, given its faster velocity and non-dispersive nature, is primarily used to determine the velocity of the wave. However, as in the case of an aluminum plate, the in-plane surface displacement of the extensional mode is inversely proportional to its frequency, with most of the energy of the in-plane component being contained near the mid-plane of the material; the opposite effect is seen for the out-of-plane component of the extensional mode [21]. The PZT wafer sensors used are designed to be much more sensitive to the in-plane component but there is only a small percentage of in-plane energy available for measurement. The internal structure of composite materials is quite different from isotropic media but this phenomenon may also influence AE measurements in this study.

Figure 8 shows the location of raw AE data and the corresponding signal density plots relative to sensor placement. While it is possible to notice some areas of higher AE activity, the copious nature of polymer matrix composites can mask useful information due to the sheer number of events. The density plot highlights regions of high localized activity that is not clearly visible in the raw data. These clusters of signals are the targets of the correlation technique and can be indicators of critical damage growth. In addition, having location information gives the ability to see where the specimen will fail in real time.

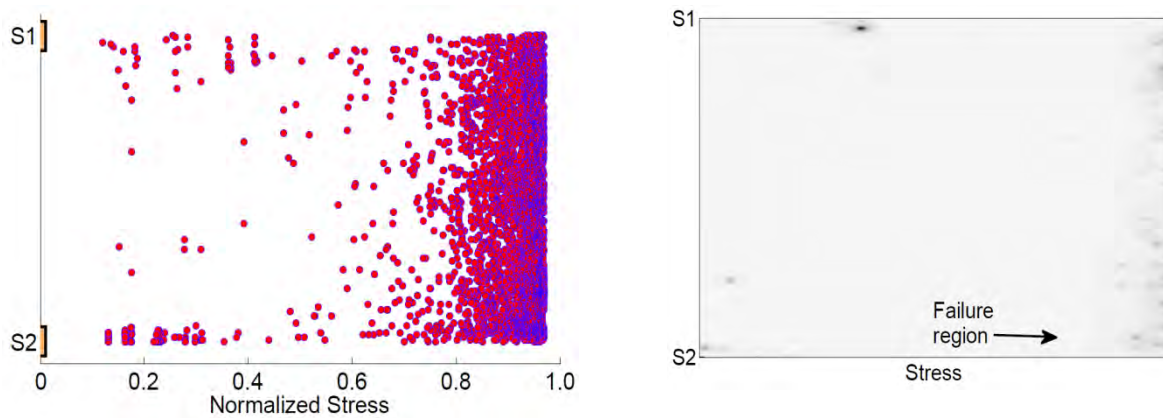


Figure 8. Raw AE location data (left) and signal density (right) plots. S1 and S2 refer to sensors 1 & 2.

The above plot shows the location of AE events as the specimen was loaded to failure. Tens of thousands of signals were measured but the events were seemingly distributed randomly along the gage section. Using only location, there was not a relative clustering of signals near the failure region which would be noticeable in the density plot on the right. However, there was useful information extracted from the above data using correlation and it was plotted in the form of clusters, seen below.

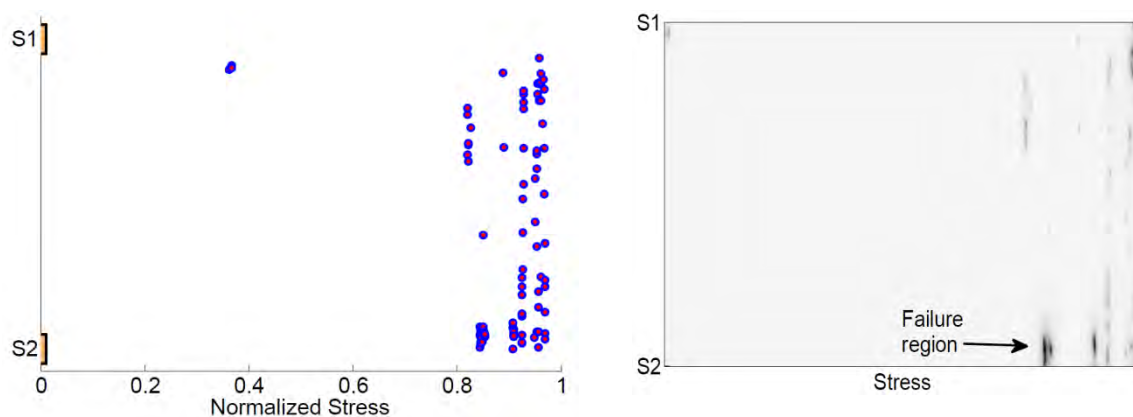


Figure 9. AE cluster location (left) and cluster density (right) plots.

Figure 9 shows the results of applying the correlation technique to raw AE data. Whereas the raw data and the AE parameter data gave very limited insight, the cluster based approach

provided indication of critical damage growth as well as location information. Failure of the specimen occurred slightly above sensor 2 which corresponds well with the dense region of AE clusters. On the color spectrum, red indicates an area of high signal density. The two dense clusters align well with the failure area but slightly less dense clusters appear near sensor 1 right before failure. Ideally, the location of the clusters should indicate where the material will fail. However, the uncertainty associated with the material in terms of its internal structure, Lamb wave behavior, and even the speed of sound right before sudden failure is not well understood and requires more investigation.

2.5 Conclusion

Quasi-static tension tests were performed on cross-ply and quasi-isotropic CFRP specimens. The traditional acoustic emission parameters, such as frequency and duration, were examined for information pertaining to the different types of damage growth during testing. While slight differences were noticed in the frequency and duration centroids of the matrix crack saturation region and the fiber break region for the cross-ply material, there was too much scatter in the data to quantify anything useful. The AE parameter analysis for the quasi-isotropic data was unable to highlight the different failure regions as well.

A correlation technique was developed to extract localized damage growth information associated with critical damage growth. Using the same AE data that yielded minimal information from traditional parameter analyses, the correlation process was able to extract localized clusters which are directly related to fiber bundle failure. This technique was able to monitor the development and growth of various clusters sizes and found that the occurrence of large clusters directly precedes sudden failure.

References

1. Reifsnider, K.L. and Jamison, R., *Fracture of Fatigue-Loaded Composite Laminates*. International Journal of Fatigue, 1982. **4**(4): p. 187-197.
2. De Rosa, I., C. Santulli, and F. Sarasini, *Acoustic emission for monitoring the mechanical behaviour of natural fibre composites: A literature review*. Composite: Part A, 2009. **40**: p. 1456-1469.
3. Thionnet, A., Chou, H.Y., and Bunsell, A., *Fibre break processes in unidirectional composites*. Composites: Part A, 2014. **65**: p. 148-160.
4. Scott, A., et al., *Damage accumulation in a carbon/epoxy composite: Comparison between a multiscale model and computed tomography experimental results*. Composite: Part A, 2012. **43**: p. 1514-1522.
5. Morton, H., et al., *Quantification of carbon fibre/epoxy resin composite failure processes using synchrotron radiation computed tomography*, in *ECCM15-15th European conference on composite materials*. 2012.
6. Foster, G., *Tensile and Flexure Strength of Unidirectional Fiber-Reinforced Composites: Direct Numerical Simulations and Analytic Models*, in *Department of Engineering Science and Mechanics*. 1998, Virginia Polytechnic Institute and State University.

7. Liu, P.F., et al., *A study on the failure mechanisms of carbon fiber/epoxy composite laminates using acoustic emission*. Materials & Design, 2012. **37**: p. 228-235.
8. Mechraoui, S.-E., A. Laksimi, and S. Benmedakhene, *Reliability of damage mechanism localisation by acoustic emission on glass/epoxy composite material plate*. Composite Structures, 2012. **94**(5): p. 1483-1494.
9. Yu, Y.-H., et al., *A study on the failure detection of composite materials using an acoustic emission*. Composite Structures, 2006. **75**(1-4): p. 163-169.
10. Bussiba, A., et al., *Damage evolution and fracture events sequence in various composites by acoustic emission technique*. Composites Science and Technology, 2007.
11. Jong, H.J., *Transverse Cracking in a Cross-ply Composite Laminate - Detection in Acoustic Emission and Source Characterization*. Journal of Composite Materials, 2005. **40**(1): p. 37-69.
12. Gorman, M., *Modal AE analysis of fracture and failure in composite materials, and the quality and life of high pressure composite pressure vessels*. Journal of Acoustic Emission, 2011. **29**: p. 1-28.
13. Ogi, K., S. Yashiro, and K. Niimi, *A probabilistic approach for transverse crack evolution in a composite laminate under variable amplitude cyclic loading*. Composites Part A: Applied Science and Manufacturing, 2010. **41**(3): p. 383-390.
14. Wharmby, A., *Observations on damage development in fibre reinforced polymer laminates under cyclic loading*. International Journal of Fatigue, 2003. **25**(5): p. 437-446.
15. Bourchak, M., et al., *Acoustic emission energy as a fatigue damage parameter for CFRP composites*. International Journal of Fatigue, 2007. **29**(3): p. 457-470.
16. Blassiau, S., A. Thionnet, and A. Bunsell, *Micromechanisms of load transfer in a unidirectional carbon fibre-reinforced epoxy composite due to fibre failures. Part 2: Influence of viscoelastic and plastic matrices on the mechanisms of load transfer*. Composite Structures, 2006. **74**: p. 319-331.
17. Marec, A., J.H. Thomas, and R. El Guerjouma, *Damage characterization of polymer-based composite materials: Multivariable analysis and wavelet transform for clustering acoustic emission data*. Mechanical Systems and Signal Processing, 2008. **22**(6): p. 1441-1464.
18. Godin, N., et al., *Clustering of acoustic emission signals collected during tensile tests on unidirectional glass/polyester composite using supervised and unsupervised classifiers*. NDT & E International, 2004. **37**(4): p. 253-264.
19. Loutas, T. and V. Kostopoulos, *Health monitoring of carbon/carbon, woven reinforced composites. Damage assessment by using advanced signal processing techniques. Part I: Acoustic emission monitoring and damage mechanisms evolution*. Composites Science and Technology, 2009. **69**(2): p. 265-272.
20. Sause, M.G.R., et al., *Pattern recognition approach to identify natural clusters of acoustic emission signals*. Pattern Recognition Letters, 2012. **33**(1): p. 17-23.
21. Rose, J., *Ultrasonic Waves in Solid Media*. 1999.

PART 3: INFLUENCE OF ATTENUATION ON ACOUSTIC EMISSION SIGNALS IN CARBON FIBER REINFORCED POLYMER PANELS

Abstract

Influence of attenuation on acoustic emission (AE) signals in Carbon Fiber Reinforced Polymer (CFRP) crossply and quasi-isotropic panels is examined in this paper. Attenuation coefficients of the fundamental antisymmetric (A_0) and symmetric (S_0) wave modes were determined experimentally along different directions for the two types of CFRP panels. In the frequency range from 100 kHz to 500 kHz, the A_0 mode undergoes significantly greater changes due to material related attenuation compared to the S_0 mode. Moderate to strong changes in the attenuation levels were also noted with propagation directions. Such mode and frequency dependent attenuation introduces major changes in the characteristics of AE signals depending on the position of the AE sensor relative to the source. Results from finite element simulations of a microscopic damage event in the composite laminates are used to illustrate attenuation related changes in modal and frequency components of AE signals.

3.1 Introduction

Acoustic emissions (AE) are stress waves generated due to localized release of strain energy by processes such as crack growth in structural materials. These stress waves which propagate in the structures serve as indicators of damage growth. AE signals in composite laminates originate from multiple failure modes such as transverse matrix cracks, delaminations, and fiber breaks. The different failure modes are expected to act as distinctly different acoustic sources within the laminate.

In plate type structures, stress waves generated by damage events propagate as combinations of different Lamb wave modes [1-4]. The presence of each type of Lamb wave mode and its frequency content is determined by the location and type of the damage event. In composite test specimens, results from previous studies [5-7] indicated occurrence of AE signals in the frequency range between 100 kHz and 500 kHz. In this frequency range, the stress wave propagation is dominated primarily by the fundamental symmetric and antisymmetric modes, commonly referred to as S_0 and A_0 modes and the shear type SH_0 modes [8-12]. Near the higher end of the specified frequency range, higher order modes occur in some cases. These higher order modes are either too small or undetectable by commercially available AE sensors. Hence, experimental AE signals in composite materials, in the specified frequency range, are likely to be combinations of the fundamental modes.

There were numerous attempts in the literature [7, 13-15] to classify AE signals according to the likely failure modes that generate these signals. However, definitive relationships between the different failure modes and the features of resulting AE signals have not been established. Such correlations would be feasible only if the distinguishing features such as ratio of different modes, and different frequency components are preserved in the signals as they propagate along the composite laminates. If these features are not preserved during the propagation of AE related

waves, it would be futile to repeat the attempts to relate features of AE signals to composite failure modes.

The characteristics of AE signal waveforms in terms of the amplitudes of individual wave modes and frequency components are important for identifying failure modes. Both the amplitude and frequency content of the AE signals are altered by different attenuation mechanisms as the waves propagate in the laminates. Geometric spreading as well as frequency dependent dispersion reduces the amplitude of AE signals. The viscoelastic nature of the matrix in carbon/polymer composites introduces significantly higher levels of attenuation.

There have been several studies in the past on the measurement of attenuation in aluminum and composite structures. Mason [16] describes a general procedure for the measurement of attenuation in materials. Ramadas et al. [17] modeled attenuation of Lamb waves using Rayleigh damping model. Pandya et al. [18] experimentally studied the reduction in amplitudes of stress waves with distance in a ballistic impact test in composites. Wandowski et al. [19] conducted attenuation measurements by means of PZT sensors placed on a composite laminate. Kerber et al. [20] used Chirplet transform to calculate attenuation of Lamb wave modes. Sun et al. [21] studied the effects of material viscoelasticity by using numerical model of laser generated Lamb waves. Drinkwater et al. [22] examined the effect of compressively loaded elastomer on propagation of A_0 and S_0 wave modes experimentally. Aggelis et al. [23] used numerical model of a homogeneous material to present how features of AE signals such as duration, rise time and frequency change with distance. Maillet et al. [24] used energy attenuation as an indicator for damage monitoring and lifetime prediction.

The major objective of the present work is to examine how the AE signals generated by damage mechanisms are modified as they propagate across composite laminates. In addition to understanding the changes introduced to AE signals during propagation, the information generated in this paper will also be useful for developing appropriate experimental procedures including the selection of sensors, number of sensors, and their locations for monitoring composite structural members. The AE signals, as discussed earlier, are composed of different frequency and modal components of Lamb waves. Attenuation coefficients of the fundamental Lamb waves which constitute AE signals, over a range of frequencies were measured experimentally in selected directions for a crossply and a quasi-isotropic plate. The AE transducers used in this study are sensitive to out of plane displacements and because of this the SH_0 component is not included in the study. These attenuation coefficients were later incorporated into numerically generated AE waveforms to illustrate the effect of attenuation on AE signals detected at various distances from the source. The details of the experimental as well as numerical procedures and results are presented in the following sections.

3.2 Experiments to determine material related attenuation as function of mode and frequency

Attenuation coefficients of A_0 and S_0 wave modes in two different laminate configurations were measured. They consisted of a crossply laminate with stacking sequence of $[0/90]_{6s}$ and a quasi-isotropic laminate with stacking sequence of $[+45/90/-45/0]_{3s}$, both of which had a total of 24 plies. The dimensions of the crossply and quasi-isotropic laminates were $600 \text{ mm} \times 600 \text{ mm} \times 3 \text{ mm}$ and $425 \text{ mm} \times 425 \text{ mm} \times 3 \text{ mm}$, respectively. The laminates were inspected using thermography to ensure that they were free from major defects. The fiber volume ratio for the laminates was determined to be 0.65.

The panels were excited by single frequency five cycles Hanning window tone burst signal at frequencies ranging from 100 kHz to 500 kHz, in 50 kHz increments. The pulses were applied at locations selected to minimize the effect of reflections from the edges. The peak amplitudes of the A_0 and S_0 components of the received pulses were measured along the directions of 0, 30, 45, 60 and 90 degrees as shown in Figure 1. Along each of these directions, the amplitudes were measured at equally spaced points up to a maximum distance of 250 mm. At each of these locations, the signals were measured on both surfaces of the laminates, so that the S_0 and A_0 components of the signals could be separated by the addition and subtraction of the signal waveforms.

The stress wave signal was introduced into the laminate in most cases using a 5 MHz, 6 mm diameter, damped ultrasonic transducer. In order to generate stronger S_0 modes below 300 kHz, a piezoelectric wafer bonded to the surface of the laminate was used. The response signal waveforms were received in all cases using another 5 MHz, 6 mm diameter, damped ultrasonic transducer. The received waveforms were amplified by a preamplifier with 50 kHz high pass filter and recorded in a commercial AE monitoring system at a sampling rate of 5×10^6 samples/second.

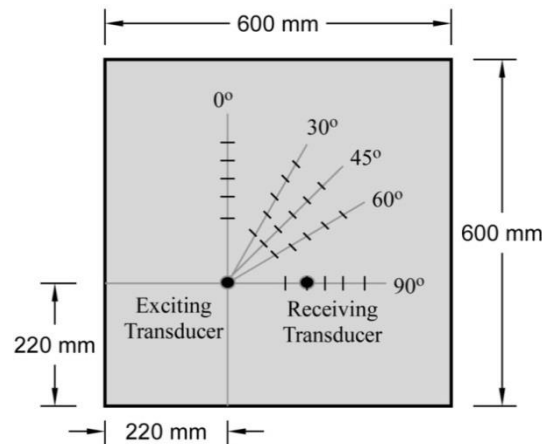


Figure 1 Angles of measurement.

3.3 Experimental results

3.3.1 Identification of A_0 and S_0 modes

Surface excitation of the panels by the sine wave pulses resulted in excitation of multiple Lamb wave modes. For the relatively low frequencies considered here, the Lamb waves predominantly propagate in the form of S_0 and A_0 modes that are separated in time because of the differences in their velocities. The SH_0 component was not detectable as it produces no out of plane displacements. Figure 2 shows two waveforms obtained at the same location but on opposite faces of the crossply laminate. These waveforms were obtained along the 0 degree direction, for 200 kHz input excitation at distance of 100 mm. The A_0 and S_0 wave mode components can be clearly distinguished from the figure.

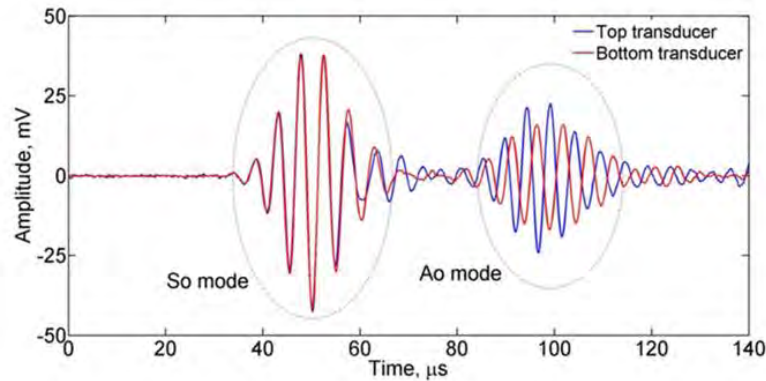


Figure 2 Representative waveforms used for measuring received signal amplitudes; waveforms in crossply laminate

3.3.2 Dispersion curves of the laminates

The experimentally determined Lamb wave dispersion of the fundamental A_0 and S_0 modes along 0 degree direction in the laminates is shown in Figure 3. Time-of-flight analysis was used to generate the dispersion curves. As mentioned earlier, multiple measurements were available at each frequency. The best estimate of the velocity at a given frequency was obtained through averaging. The experimentally determined dispersion curves were assessed for validity through review of similar curves which were generated for similar and different laminate configurations [8-12]. Phase velocities in the two laminate configurations were also evaluated by a software developed by LAMSS (Laboratory for Active Materials and Smart Structures) at University of South Carolina.[25]

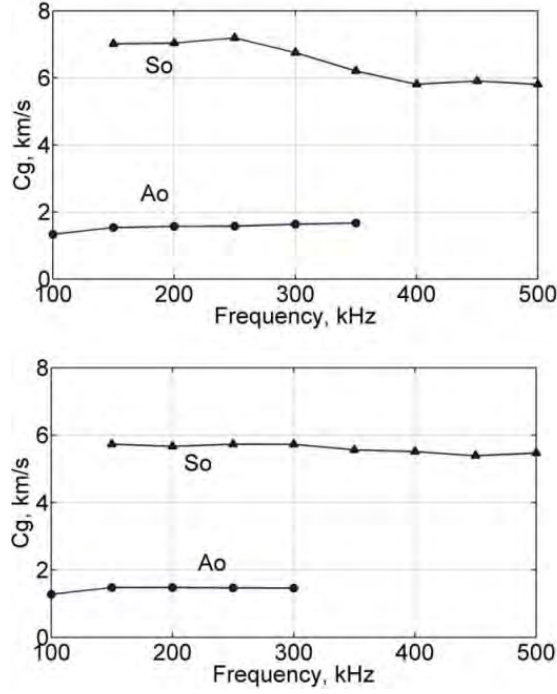


Figure 3 Dispersion curves for crossply (top) and quasi-isotropic (bottom) panels along 0 degree directions

3.3.3 Calculation of attenuation coefficients

The reduction in signal amplitude caused by geometric spreading as the stress waves travel outwards from a source, in a plate like structure, is assumed to be inversely proportional to the square root of the radial distance from the source. The attenuation due to energy loss mechanisms such as material absorption is assumed to result in an exponential decay of the amplitude with distance of propagation. Combining these two effects, the amplitude of a signal, v , at a distance, x is given by

$$v = \left(\frac{1}{\sqrt{x_i}} \right) V e^{-\alpha x} \quad (3.1)$$

Where, V represents the peak amplitude at the source and α is the attenuation coefficient.

Calculation of an attenuation coefficient using equation (3.1) is impossible from single measurement of amplitude as the source amplitude is often unknown. Hence, the attenuation coefficient can be determined by defining equation (3.1) for two different points at radial distances x_1 and x_2 for which the measured peak amplitudes are V_{m1} and V_{m2} respectively. In such a case, the attenuation coefficient is calculated using

$$\alpha = \left(\frac{1}{x_2 - x_1} \right) \ln \left(\frac{V_{m1} \sqrt{x_1}}{V_{m2} \sqrt{x_2}} \right) \quad (3.2)$$

When multiple measurement points exist along a given direction and at a given frequency, several calculated values of attenuation coefficients become available. A least squares method can

be used to obtain a single representative value of the attenuation coefficient from such multiple values. Using equation (3.1) and N amplitude measurements, V_{mi} , along a given direction, the error function can be defined as:

$$\varepsilon = \sum_1^N (V_{mi}\sqrt{x_i} - V e^{-\alpha x_i})^2 \quad (3.3)$$

Alternatively, the error function can be written on a logarithmic function as:

$$\varepsilon = \sum_1^N (\ln(V_{mi}\sqrt{x_i}) - \ln(V e^{-\alpha x_i}))^2 \quad (3.4)$$

Or,

$$\varepsilon = \sum_1^N (\ln(V_{mi}\sqrt{x_i}) - (-\alpha x_i + \ln(V)))^2 \quad (3.5)$$

We want to determine the values of α and V which minimize the error function such that

$$\frac{\partial \varepsilon}{\partial \alpha} = 0 \quad \text{and} \quad \frac{\partial \varepsilon}{\partial V} = 0$$

This gives,

$$-2 \sum_1^N (\ln(V_{mi}\sqrt{x_i}) - (-\alpha x_i + \ln(V))) x_i = 0 \quad (3.6)$$

and,

$$-2 \sum_1^N (\ln(V_{mi}\sqrt{x_i}) - (-\alpha x_i + \ln(V))) = 0 \quad (3.7)$$

This gives a set of equations which in matrix form can be written as follows.

$$\begin{Bmatrix} -\alpha \\ \ln(V) \end{Bmatrix} = \begin{bmatrix} \sum_{i=1}^N x_i^2 & \sum_{i=1}^N x_i \\ \sum_{i=1}^N x_i & N \end{bmatrix}^{-1} \begin{Bmatrix} \sum_{i=1}^N x_i \ln(V_{mi}\sqrt{x_i}) \\ \sum_{i=1}^N \ln(V_{mi}\sqrt{x_i}) \end{Bmatrix} \quad (3.8)$$

Hence, the representative attenuation coefficient, α , can be determined using equation (3.8)

3.3.4 Attenuation coefficients for the CFRP panels

In the experiments, it was noted that the S_0 modes propagate longer distance than the A_0 modes; hence, it was possible to measure the S_0 modes at propagation distances between 25 mm and 250 mm from the source, with 25 mm intervals. For A_0 modes, however, the measurements were made between propagation distances of 25 mm and 100 mm from the source with 12.5 mm intervals. Attenuation coefficients of the S_0 and A_0 modes were obtained from these measurements along each propagation direction for each frequency described in section 2.

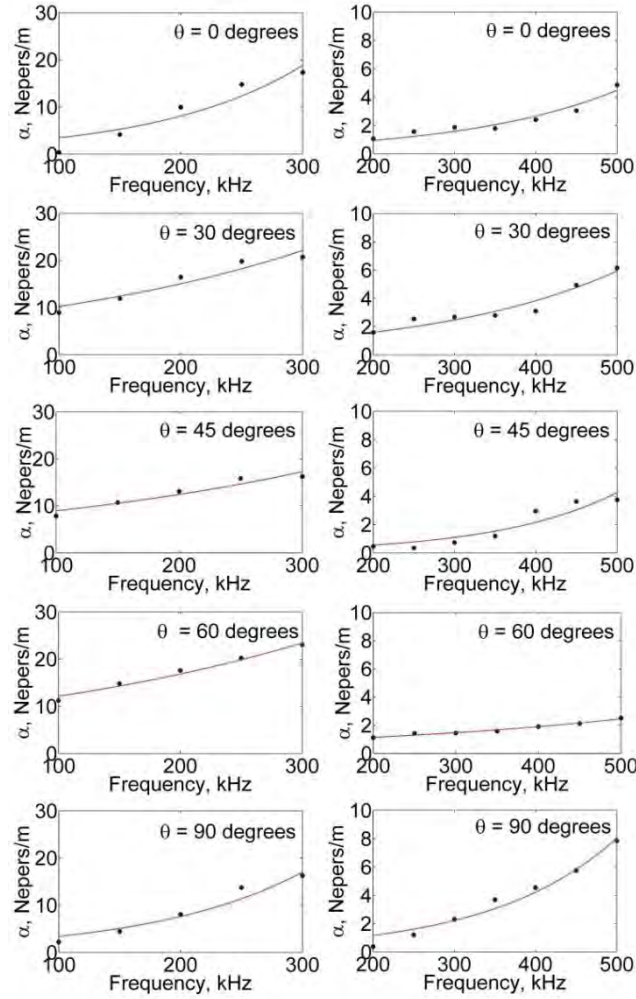


Figure 4 Attenuation coefficients of A_0 (left) and S_0 (right) modes in the crossply laminate along different directions.

Crossply Laminate

A_0 modes: Figure 4 shows the attenuation coefficients of the A_0 and S_0 modes in the crossply laminate along different directions. Because of the steep increase in attenuation with frequency seen in A_0 modes, measurements could be made only to a maximum frequency of 300 kHz. At 100 kHz, attenuation was observed to be relatively lower in the 0 and 90 degree directions with a value of about 3 Nepers/m while along 30, 45, and 60 degree directions; the attenuation was three times higher. The rates of increase of the attenuation with frequency were different for the different directions. The attenuation at 300 kHz was found to lie between 17 and 23 Nepers/m in the five directions considered here.

S_0 modes: Because of the lower attenuation seen in S_0 modes, attenuation measurements could be carried out up to a frequency of 500 kHz. There was modest variation of attenuation levels in the 5 different directions considered. At 200 kHz the attenuation was within the range of 0.5 and 2 Nepers/m in the five directions. However, at 500 kHz, the attenuation was found to be only 2.5 Nepers/m along 60 degree direction while along 90 degree direction it was about 8

Nepers/m. In the other three directions, attenuation values were between these two values. Over the lower frequency side of the measurements, the attenuation level experienced by the signals was very minimal.

Quasi-isotropic Laminate

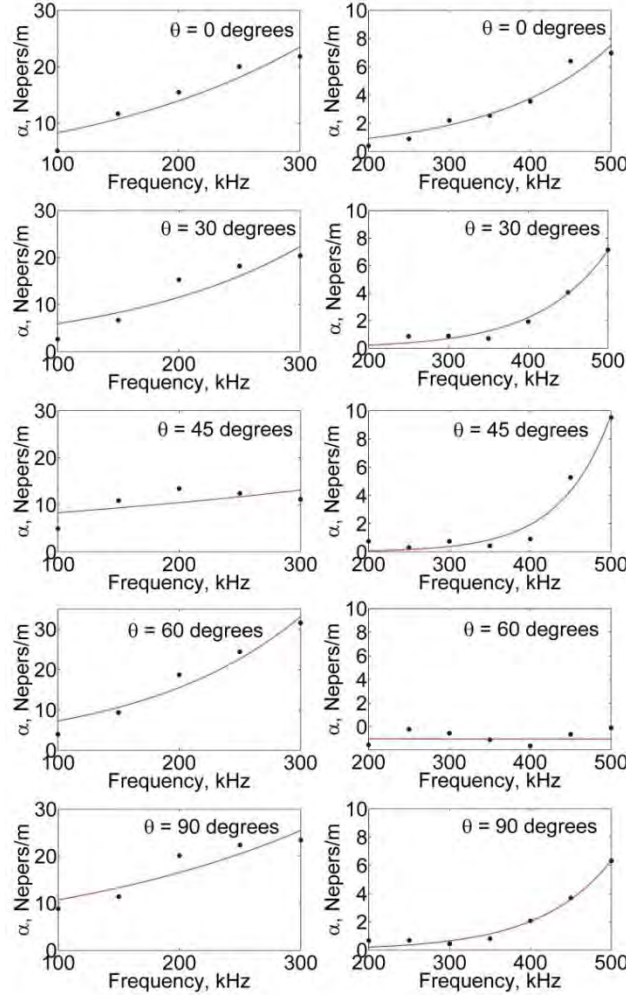


Figure 5 Attenuation coefficients of A_0 (left) and S_0 (right) modes in the quasi-isotropic laminate along different directions.

A_0 modes: Figure 5 shows the attenuation coefficients of the A_0 and S_0 modes in the quasi-isotropic laminate along different directions. As in the case of the crossply specimen, there was a steep increase in attenuation with frequency of A_0 modes. At 100 kHz frequency, attenuation values varied between 6 and 11 Nepers/m. The lowest values were found along 30 and 60 degree directions. The attenuation value for a frequency of 300 kHz was the lowest along 45 degrees at 13 Nepers/m and the highest along 60 degrees direction at 31 Nepers/m.

S_0 modes: As in the case of the crossply laminate, the attenuation of S_0 modes was lower than that of A_0 modes. Attenuation values of the signals at 200 kHz in the five directions considered here were about 1 Neper/m. There were moderate differences in the rate at which S_0 mode attenuation increased with frequency among the different directions. Along the 60 degree

direction, attenuation remained unaffected by the frequency within the range considered. Along the other four directions, the attenuation values at 500 kHz ranged from 6 Nepers/m to 10 Nepers/m.

3.3.5 Discussion of experimental results

In general, A_0 modes were found to have significantly higher levels of attenuation compared to S_0 modes in both the crossply and quasi-isotropic laminates. In addition, in all propagation directions, there is an increase in attenuation with frequency. The propagation direction of 60 degrees is an exception in which attenuation seems to vary very little with frequency for S_0 mode. At a frequency of 200 kHz, the attenuation values of A_0 mode in most directions range from 10 to 20 Nepers/m whereas for S_0 mode, attenuation values range from 0.2 to 1.2 Neper/m for both panels studied in this paper. Hence, at this frequency it takes just 50 mm (2 in) for the amplitude of A_0 mode to lose 80% of initial amplitude where as it takes 300 mm (12 in) for the same thing to happen for S_0 mode. At frequencies greater than 300 kHz, A_0 mode is virtually undetectable beyond a propagation distance of 50 mm (2 in) while even at 500 kHz, the S_0 mode retains nearly 10% of its amplitude after propagating a distance of 250 mm (10 in).

The attenuation coefficients obtained in the quasi-isotropic laminate deviated from the assumed quasi-isotropy behavior. Assumption of quasi-isotropy is valid for such laminates under in-plane loadings. However, because of the variation of strain state in the thickness direction, the quasi-isotropy behavior is not exhibited under bending types of loads. This was described in the discussion of Laminate plate theory by [26]. As the flexural components of displacements do not show quasi-isotropy, some direction dependency is exhibited by wave propagation in the laminates. This was true in the phase velocities as well as group velocities of a quasi-isotropic laminate studied by Rose [8]. This is likely to result in direction dependency of amplitudes of signal waveforms and attenuation coefficients calculated from the amplitude measurements.

In composite laminates, each combination of propagation direction, mode and frequency is likely to result in a different state of deformation including in-plane, bending and twisting components and their variation across the thickness. The resulting deformation of the material is unevenly distributed between the reinforcing fibers and the polymer matrix. In addition, there is beam steering that influences the measured stress wave amplitudes. It is expected that when the matrix material shares the bulk of deformation, the viscoelastic nature of the matrix will result in greater attenuation of the propagating stress wave. Variations in the modes and frequencies result in changes in the strain and deformation components among the individual laminae within the laminate, which in turn will affect the attenuation values. Since the absence of increase in attenuation level of S_0 mode with the increase of frequency along the 60 degree direction was different from those seen in other directions, the experiments were repeated several times, including different parallel paths at 60 degree orientation, and the observed behavior was confirmed to be the true behavior along this direction.

3.4 Illustration of effect of attenuation on acoustic emission waveforms

In plate type structures, AE related waves propagate in the form of Lamb waves occurring over a range of amplitudes and frequencies. As mentioned in the introduction section, different attenuation mechanisms act on these waves. In this section, we demonstrate how the different mechanisms affect the waves as they propagate in the panels. AE events were numerically simulated and corresponding waveforms were measured at several evenly spaced locations. The 2D numerical waveforms take into account the dispersion due to the wide range of frequency components contained in the waveforms. The material absorption factor was later included by making use of the attenuation coefficients which were reported in the previous section. Finally, the geometric spreading factor was included to demonstrate the progressive reduction in amplitudes of the signals.

The procedures used to modify the waveforms in this section are validated by comparing the amplitudes of the modified waveforms with the amplitudes of experimentally generated AE type waveforms in the composite laminates. The AE type signals were generated along 0 degree direction of the laminates by applying a triangular pulse on the laminates. The applied pulse type load and its frequency spectrum are described in the following section. The procedures used for these experiments are quite similar to those described in section 3.2.

3.4.1 Finite element simulations of AE signals

The governing equation for elastodynamic wave propagation in a continuous medium is given by equation (4.1). In the equation, σ_{ij} represents the stress tensor, f_i represents the body force vector and the displacement vector is represented by u_i . In our studies, the solution for this equation was obtained through explicit time integration in LS-DYNA

$$\sigma_{ij,j} + f_i = \rho \frac{\partial^2 u_i}{\partial t^2} \quad (4.1)$$

In previous studies, authors used different types of source functions to simulate energy release during an AE event [27-29]. In the current study, triangular pulse was chosen since it provided waveforms with S_0 and A_0 components in the desired frequency spectrum of this study. The triangular pulse along with its frequency spectrum is shown in Figure 6. The same type of pulse was also used to generate experimental AE type waveforms in the laminates. These waveforms were used to validate the procedures implemented to modify the numerical waveforms.

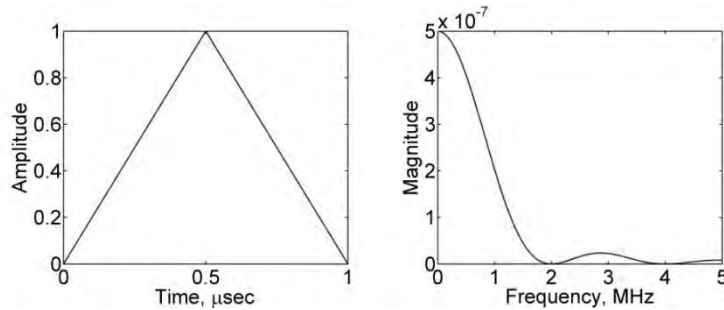


Figure 6 Triangular pulse and its frequency spectrum

Two dimensional plane strain numerical models of the crossply and quasi-isotropic laminates were generated in LS-Prepost. The models had dimensions of 1200 mm by 3 mm. Each of the individual plies in the laminates was modeled by a layer of elements. The elements in each layer had size of 0.125 mm by 0.25 mm. The models totally consisted of 115200 elements and 120025 nodes. The models were used to simulate AE related wave propagation along the 0 degree direction of the respective laminates. The lamina properties shown in Table 1 [30] were used in the simulations. In both models, the left edge was fully constrained and the triangular pulse described earlier was applied on the right edge at a depth of 0.75 mm. During the solution, the stresses and nodal displacements were calculated at a stable increment of 10.8 ns.

Table 1 Lamina Properties

E_1, Pa	E_2, Pa	G_{12}, Pa	G_{23}, Pa	ν_{12}	ν_{23}	ν_{13}
1476e9	10.3e9	7e9	3.7e9	0.27	0.54	0.27

It was possible to generate AE related wave propagation which consisted of different Lamb wave modes. The two dimensional models do not include the geometric spread of the waves as function of propagation distance. Because of the linear elastic properties used in the models, the obtained waveforms were free of material related attenuation. Out of plane displacement waveforms were taken between propagation distances of 25 mm and 250 mm at increment of 25 mm. The numerically generated waveforms were filtered to remove components outside of the 100 kHz-500 kHz range. Figure 7 shows a numerical out of plane displacement waveform and its wavelet. The waveform was measured at distance of 150 mm from the AE source in the crossply laminate. AGU Vallen wavelet is used to obtain the wavelet diagram.

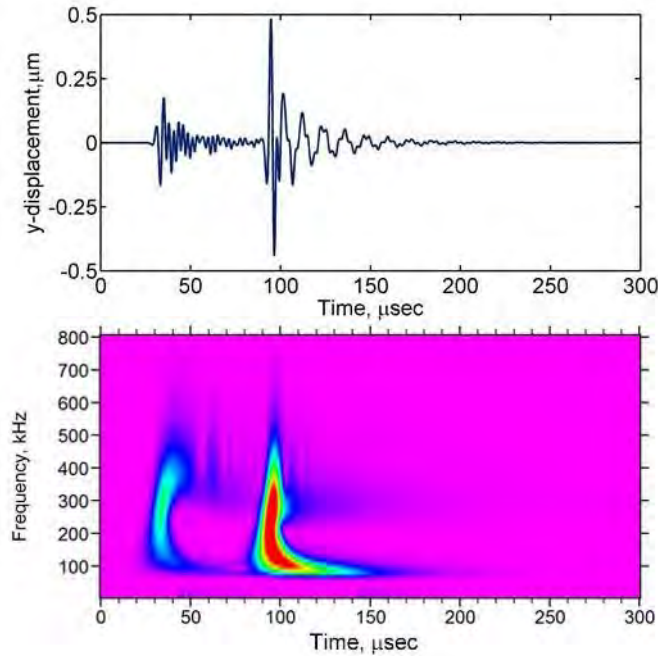


Figure 7 Signal waveform and wavelet diagram for numerical AE event

3.4.2 Different attenuation mechanisms and AE signals

The simulated AE waveforms, after filtering between 100 kHz and 500 kHz, were primarily composed of S_0 and A_0 modes. As mentioned earlier, dispersion was present in these waveforms because of the wider frequency range. The intent of this section is to illustrate the effect of material related attenuation and geometric spreading on AE related waves as they propagate through the composite laminates. From the two dimensional elastic finite element simulations, waveforms at various propagation distances were obtained. These waveforms were modified to include the effects of geometric spreading and attenuation.

The experimentally determined mode and frequency dependent attenuation values, reported in section 3.4, were used to modify the numerical waveforms to illustrate material related attenuation. The S_0 and A_0 components of each of the waveforms were separated first. The frequency components of these modes were then separated by Fast Fourier transform (FFT). The amplitudes of the different frequency components were multiplied by the appropriate attenuation coefficients obtained from the experiments. The attenuated waveforms corresponding to the two modes were obtained using an inverse transform of the respective modified amplitudes. Finally, the S_0 and A_0 modes were combined to construct the attenuated AE waveform.

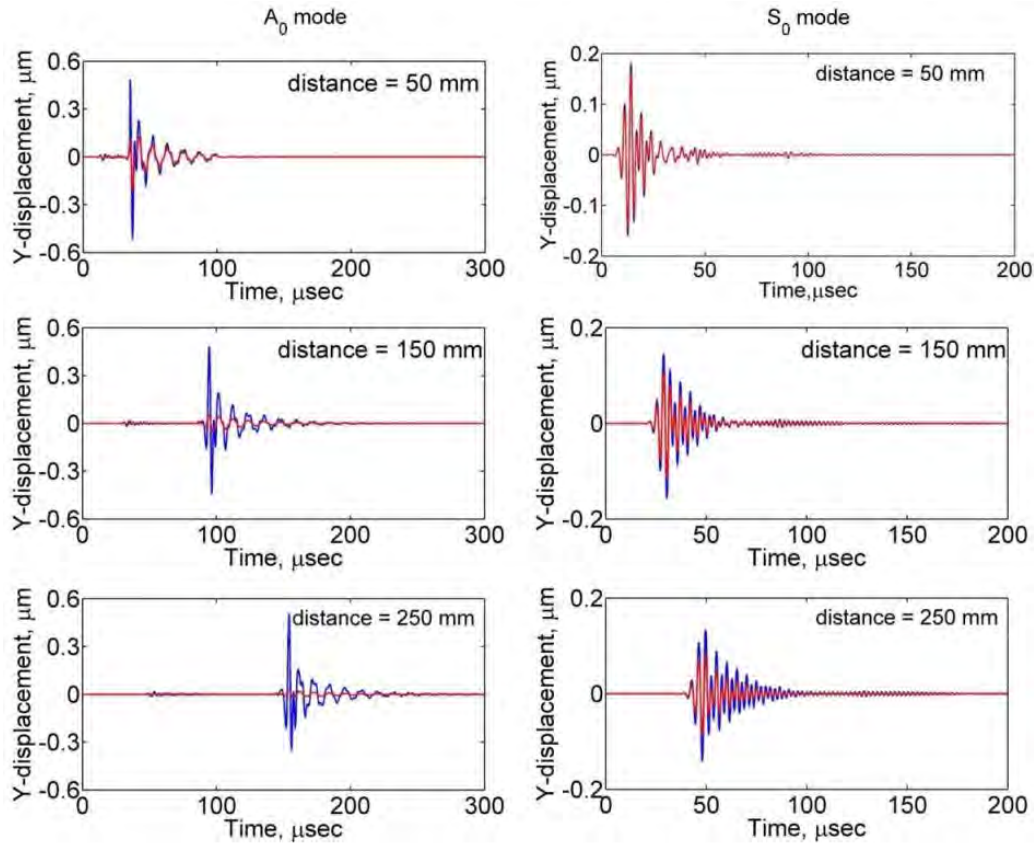


Figure 8 Numerical waveforms without and with material related attenuation for A_0 mode (left) and S_0 mode (right)

Figure 8 shows the effect of material related attenuation on the S_0 and A_0 components of the AE waveforms in the quasi-isotropic laminate. The waveforms shown in blue color are those obtained at different propagation distances without material related attenuation whereas, the waveforms shown in red color are those modified after including material attenuation. The amplitude of A_0 mode rapidly decreases with propagation distance and after a propagation distance of 250 mm, this mode is almost completely eliminated from the AE signal. The amplitude of S_0 mode, on the other hand, undergoes moderate reduction and is recognizable even after a propagation distance of 250 mm.

The effect of geometric spreading was calculated by direct implementation of equation (3.1). A reasonable estimate of peak amplitude near the source of the AE event was calculated by using peak amplitude of a wave mode at propagation distance of 25 mm and an attenuation value corresponding to the frequency at which this amplitude occurred. The calculated estimate of the peak amplitude near the source and a reasonably selected value of attenuation coefficient were used to calculate the expected amplitudes at propagation distances of 50 mm through 250 mm, with increment of 25 mm.

The peak amplitude of the waveforms at a distance of 25 mm from the source was used as the initial amplitude. The results from the two dimensional finite element model represent a parallel beam of Lamb waves propagating in the laminates. The successive modifications to the peak amplitudes of the waveforms introduced by dispersion, material related attenuation and geometric spreading were determined at points located at 50 mm through 250 mm along 0 degree directions in the two laminate configurations under consideration.

Figure 9 shows the peak amplitudes of the A_0 and S_0 modes of the AE waveforms at different propagation distances along the zero degree direction in the laminates. The dispersion related amplitude changes in A_0 and S_0 modes are indicated by blue lines along with the data points indicated by circles. There is an amplitude reduction of about 10 to 20 % in these modes at a distance of 250 mm. Further, in figure 9, the peak amplitudes of the A_0 mode appear to fluctuate about a trend line as the propagation distance increases. Detailed examination of the waveforms revealed that leading edge of the waveforms was dominated alternatively by either one or two high amplitude oscillations, apparently due to dispersion effects. This alternating distribution of energy between one or two oscillations is responsible for the amplitude fluctuations.

The red curves along with the data points indicated by '+' signs represent the amplitudes after including the changes due to both dispersion and material attenuation. At propagation distance of 250 mm, the amplitude reduction of S_0 mode in the crossply and quasi-isotropic laminates was 55% and 45% respectively. The reduction in amplitude of the A_0 mode at 250 mm was about 85% in the crossply laminate and 95% in the quasi-isotropic laminate. In addition to the peak amplitudes, because of dispersion and greater attenuation in higher frequency components, the envelopes of the two modes undergo changes with propagation distance.

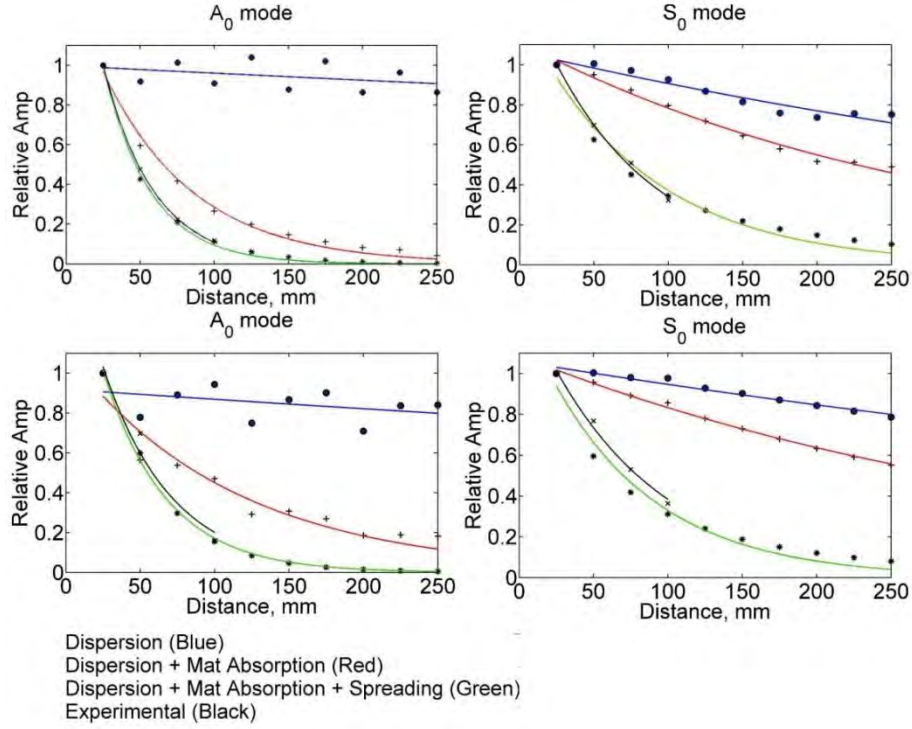


Figure 9 Amplitude reductions due to geometric spreading, material absorption and dispersion in quasi-isotropic (top) and Crossply (bottom) laminates

The green lines with data points indicated by ‘*’ represent the peak amplitudes after the geometric spreading effect was included. As a combined effect of dispersion, material related attenuation and geometric spreading, at distance of 100 mm, the amplitude of S_0 mode dropped to was about 30 of the amplitude at 25 while that of the A_0 mode about 15 % of the amplitude at 25 mm. . These amplitudes which were obtained after modification by all mechanisms were compared with the experimentally generated amplitudes. In figure 9, the black curves with ‘x’ signs represent peak amplitudes of the S_0 and A_0 parts of the experimental AE type waveforms. The excellent match between the curves validates the approaches used to generate the modified amplitudes.

3.5 Summary and conclusion

The influence of attenuation on AE signals in carbon-epoxy laminates is evaluated. Attenuation measurements were made for two common types of carbon/epoxy laminates, namely a crossply laminate and a quasi-isotropic laminate. The experimental results indicate that the A_0 modes of wave propagation experience much higher level of attenuation than their S_0 counterparts. The attenuation of the two modes further depends on the direction of propagation and their frequency components. For illustrating the effect of attenuation, numerical model of stress wave generated from a microscopic damage in a composite laminate was used. A_0 components in the AE emission signals are virtually eliminated as the signal propagates over even modest distances

of the order of 100 mm. In contrast, the S_0 mode is detectable at longer distances. The results implied that attenuation of AE signals has to be taken into consideration in deciding the number, type, and location of the sensors to be used for monitoring integrity of composite structural members. In addition, it should also be included in the interpretation of the AE signals.

References

- [1] Miller RK, Hill EK, Moore PO, Testing ASfN. Acoustic Emission Testing: American Society for Nondestructive Testing; 2005.
- [2] Gorman MR. Plate wave acoustic emission. The Journal of the Acoustical Society of America. 1991;90(1):358-64.
- [3] Eaton M, May M, Featherston C, Holford K, Hallet S, Pullin R. Characterisation of damage in composite structures using acoustic emission. Journal of Physics: conference series: IOP Publishing; 2011. p. 012086.
- [4] Aljets D, Chong A, Wilcox S, Holford K. Acoustic emission source location in plate-like structures using a closely arranged triangular sensor array. Uni Of Glamorgan, Pontypridd, Wales, UK CF37 1DL. 2010.
- [5] Oskouei A, Ahmadi M, Hajikhani M. Wavelet-based acoustic emission characterization of damage mechanism in composite materials under mode I delamination at different interfaces. Express Polym Lett. 2009;3(12):804-13.
- [6] Loutas TH, Kostopoulos V. Health monitoring of carbon/carbon, woven reinforced composites. Damage assessment by using advanced signal processing techniques. Part I: Acoustic emission monitoring and damage mechanisms evolution. Composites Science and Technology. 2009;69(2):265-72.
- [7] Arumugam V, Sajith S, Stanley AJ. Acoustic emission characterization of failure modes in GFRP laminates under mode I delamination. Journal of Nondestructive Evaluation. 2011;30(3):213-9.
- [8] Rose JL. Ultrasonic Guided Waves in Solid Media: Cambridge University Press; 2014.
- [9] Quaegebeur N, Micheau P, Masson P, Maslouhi A. Structural health monitoring strategy for detection of interlaminar delamination in composite plates. SPIE Smart Structures and Materials+ Nondestructive Evaluation and Health Monitoring: International Society for Optics and Photonics; 2011. p. 798407--11.
- [10] Wang L, Yuan FG. Group velocity and characteristic wave curves of Lamb waves in composites: Modeling and experiments. Composites Science and Technology. 2007;67(7-8):1370-84.
- [11] Scholey JJ, Wilcox PD, Wisnom MR, Friswell MI. Quantitative experimental measurements of matrix cracking and delamination using acoustic emission. Composites Part A: Applied Science and Manufacturing. 2010;41(5):612-23.
- [12] Gresil M, Giurgiutiu V. Guided wave propagation in carbon composite laminate using piezoelectric wafer active sensors. SPIE Smart Structures and Materials+ Nondestructive Evaluation and Health Monitoring: International Society for Optics and Photonics; 2013. p. 869525--15.
- [13] Ni Q-Q, Iwamoto M. Wavelet transform of acoustic emission signals in failure of model composites. Engineering Fracture Mechanics. 2002;69(6):717-28.
- [14] Ramirez-Jimenez CR, Papadakis N, Reynolds N, Gan TH, Purnell P, Pharaoh M. Identification of failure modes in glass/polypropylene composites by means of the primary

- frequency content of the acoustic emission event. *Composites Science and Technology*. 2004;64(12):1819-27.
- [15] Haselbach W, Lauke B. Acoustic emission of debonding between fibre and matrix to evaluate local adhesion. *Composites Science and Technology*. 2003;63(15):2155-62.
- [16] Mason WP, Thurston RN. *Physical Acoustics: Principles and Methods*: Academic Press; 1990.
- [17] Ramadas C, Balasubramaniam K, Hood A, Joshi M, Krishnamurthy CV. Modelling of attenuation of Lamb waves using Rayleigh damping: Numerical and experimental studies. *Composite Structures*. 2011;93(8):2020-5.
- [18] Pandya KS, Dharmane L, Pothnis JR, Ravikumar G, Naik NK. Stress wave attenuation in composites during ballistic impact. *Polymer Testing*. 2012;31(2):261-6.
- [19] Wandowski T, Malinowski P, Kudela P, Ostachowicz W. Guided wave-based detection of delamination and matrix cracking in composite laminates. *Proceedings of the Institution of Mechanical Engineers Part C-Journal of Mechanical Engineering Science*. 2011;225(C1):123-31.
- [20] Kerber F, Sprenger H, Niethammer M, Luangvilai K, Jacobs LJ. Attenuation Analysis of Lamb Waves Using the Chirplet Transform. *Eurasip Journal on Advances in Signal Processing*. 2010.
- [21] Sun HX, Xu BQ, Qian RZ. Numerical simulation of laser-generated Lamb waves in viscoelastic materials by finite element method. *Journal of Applied Physics*. 2009;106(7).
- [22] Drinkwater BW, Castaings M, Hosten B. The measurement of A(0) and S-0 Lamb wave attenuation to determine the normal and shear stiffnesses of a compressively loaded interface. *Journal of the Acoustical Society of America*. 2003;113(6):3161-70.
- [23] Aggelis DG, Matikas TE. Effect of plate wave dispersion on the acoustic emission parameters in metals. *Computers & Structures*. 2012;98–99(0):17-22.
- [24] Maillet E, Godin N, R'Mili M, Reynaud P, Fantozzi G, Lamon J. Real-time evaluation of energy attenuation: A novel approach to acoustic emission analysis for damage monitoring of ceramic matrix composites. *Journal of the European Ceramic Society*. 2014;34(7):1673-9.
- [25] <http://www.me.sc.edu/Research/lamss/html/software.html>.
- [26] Barbero EJ. *Finite Element Analysis of Composite Materials using Abaqus™*: Taylor & Francis; 2013.
- [27] Hamstad M. Acoustic emission signals generated by monopole (pencil lead break) versus dipole sources: finite element modeling and experiments. *Journal of Acoustic Emission*. 2007;25:92-106.
- [28] Hora P, Červená O. Acoustic emission source modeling. 2010.
- [29] Giordano M, Condelli L, Nicolais L. Acoustic emission wave propagation in a viscoelastic plate. *Composites Science and Technology*. 1999;59(11):1735-43.
- [30] Daniel IM, Ishai O. *Engineering Mechanics of Composite Materials*: Oxford University Press; 2006.

PART 4: CORRELATION BASED FATIGUE CRACK CHARACTERIZATION IN ALUMINUM

Abstract

The relationship between characteristic features of acoustic emission (AE) signals and crack growth in Aluminum panel is examined in this paper. AE signals from fatigue crack growth in an Al 6061 plate with edge notch were collected by means of wideband AE sensors. Distributions of cumulative and individual characteristic features of the signals were evaluated. The signal waveforms were correlated among each other to identify features which were sensitive to crack growth. It was found that the amplitude and duration features were indicative of changes in the crack growth rate. The correlations among the waveforms indicated that the amplitudes of the antisymmetric (A_0) wave components of the signal waveforms increase as the crack length increases. Such characterizations of crack related signals are useful in AE based structural health monitoring applications.

4.1 Introduction

Acoustic emissions (AE) are stress waves generated due to sudden release of strain energy by processes such as crack growth in structural materials. These waves, in plate type structures, propagate as combinations of wave modes which occur over a wide range of frequencies. AE based structural health monitoring relies on detection and analysis of such acoustic waves. The information contained in the signal waveforms could be used to locate the source of damage and identify the type of damage.

The characteristic features of AE signal waveforms such as amplitude, frequency, duration and rise time are dependent on the type of damage and its location in the monitored structure. These features could be used to characterize the relationship between AE behavior and fatigue crack propagation. In this regard, several studies in the past attempted to develop such characterizations. Aggelis et al. [1] conducted tests using aluminum compact tension specimens to characterize fatigue related damage using AE. The observed AE behavior was indicative of shift from tensile to shear type crack propagation modes. Gong et al. [2] found that the cumulative number of AE hits and cumulative amplitudes of AE signal waveforms, within selected window of amplitudes, showed linear variation with crack growth. Linear logarithmic relationships between the stress intensity factor, ΔK , and crack growth rate, da/dN , and between ΔK and hit count rate, dC/dN , were derived by Roberts et al. [3]. The tests were conducted on compact tension specimens and T-section girder specimens. Grandhi et al. [4] were able to develop relationship between AE energy release rate and crack growth rate using AE data from two plate type Aluminum test specimens. From a test on steel bridge material, Hossain et al. [5] reported that early stages of fatigue crack growth produced insignificant AE. A prognostic analysis based on AE signal absolute energy was presented by Yu et al. [6]. It was found that the absolute energy rate was able to characterize fatigue life prediction better than the count rate.

The characterization of fatigue cracks through the use of AE signal waveform features is quite useful in AE based structural health monitoring. In addition to such approaches, other authors

examined different aspects of fatigue crack growth and AE. Sause et al. [7] numerically modeled acoustic signal propagation from crack growth taking into account the dynamic displacement field which occurs during incremental crack growth. The numerical results were validated by experimental results and modeling approaches significantly different from previous approaches were used. Lugo et al. [8] used AE to quantify evolution of microstructural damage. Andreykiv et al. [9] obtained the radiation pattern of longitudinal and transverse acoustic waves from growth of penny shaped cracks in aluminum. Grondel et al. [10] conducted a test combining lamb wave and AE to monitor damage initiation and growth in aluminum. Barsoum et al. [11] applied AE to monitor the development of fatigue-crack growth in steel. Self-organizing map (SOM) to identify failure mechanisms (plastic deformation, plane strain and plane stress fracture). Fatigue life prediction was performed using backpropagation neural network (BPNN). Mukhopadhyay et al. [12] developed new AE based approach to calculate initial fracture toughness in steel specimens. The calculated values of the fracture toughness were compared with values obtained by other methods. Zain et al. [13] conducted fatigue crack growth tests on compact tension specimens to model longitudinal cracks in rail steel. The acoustic behavior was monitored during the tests. A separate study by Kordatos et al. [14] combined thermography and AE to monitor crack growth.

The present paper is concerned with the characterization of fatigue crack related acoustic emissions. The objective has been to examine the relationship between characteristics of AE waveforms and crack growth in an Aluminum 6061 panel. Changes in cumulative and individual distributions of the characteristic features of the signals were examined. The signal waveforms were correlated among each other to identify features which were sensitive to crack growth rate. The details of the crack growth experiment, the analysis, and the obtained results are presented in the following sections.

4.2 Experiments

Fatigue crack growth test was done on an aluminum plate from which over 40000 AE events were obtained. These signals were obtained for crack growth of 84 mm before the specimen failed. In this section, the test setup and procedures of fatigue load application are presented.

4.1.1 Test setup

Figure 1 shows the Al 6061 aluminum plate specimen used for the crack growth test. The dimensions for the plate, as shown in Figure 1, were 225 mm \times 500 mm \times 3 mm. The plate had a notch extending from one edge up to length of 38 mm. The end fixture assembly to mount the plate onto the Material Test System (MTS), and to apply the fatigue load onto the plate was designed such that the maximum stress conditions were near the edge notch tip.

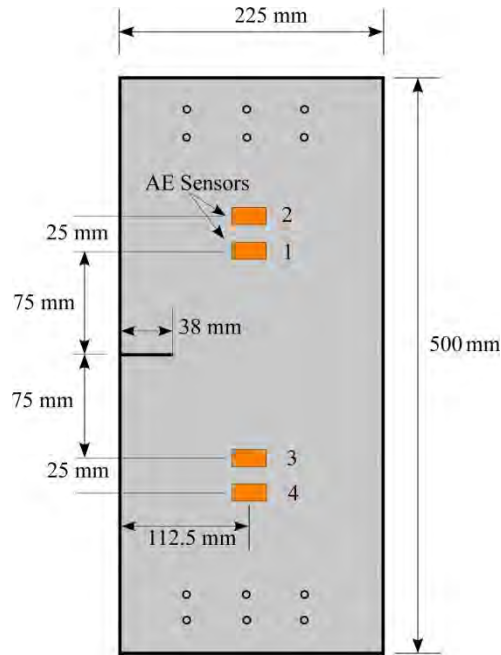


Figure 1. Test specimen

The plate was instrumented with four AE transducers to detect the AE signals from crack growth. The four transducers were rectangular piezoelectric wafers bonded to the surface of the plate. These sensors were shown to have wide band characteristics and could detect signals up to a frequency of 700 kHz. The use of transducers located above and below the path of crack growth enabled filtering of signals that originated from crack growth through comparison of time of arrival at the transducers. The signals from the transducers were amplified by Physical Acoustics Corporation PAC 2/4/6 preamplifiers at 40 dB gain. PCI-2 data acquisition system was used to acquire the signal waveforms at a rate of 10×10^6 samples/second. A 35 dB threshold was set while acquiring the AE signals. The waveforms were recorded for a length of 1 ms and contained a total of 10240 data points per waveform. However, segments of the waveforms beyond 150 μ s were affected by reflections and were not used in analysis. The results discussed in this paper are from the bonded piezoelectric sensor which, in Figure 1, is labelled as 1.

4.1.2 Test procedure

The plate was mounted on 20000 lbs. (90000 N) 810 Material Test System. It was subjected to loads of 2750 ± 2250 lbs. (12250 ± 10000 N) which were applied at a rate of 5 Hz. It took about 10000 cycles to initiate the first noticeable crack from the edge notch tip. The tests continued till the specimen fractured at around 74000 cycles. The acoustic emissions generated due to crack advance were recorded by the system described earlier. Crack growth continued for 84 mm before final fracture occurred.

4.3 Results and discussion

4.3.1 Fatigue crack growth

Figure 2(a) shows the crack growth with the number of cycles from the test. The rate of crack growth is also shown in figure 2(b). The plots are shown on a semi-log y-axis scale. After initiation, the crack propagation continued with declining rates of growth until crack length of 5.5 mm. The crack growth between 5.5 mm and 43 mm appeared to show linear variation on the semi-log scale plot. Between 43 mm and fracture, the crack advanced rapidly with continually increasing growth rates.

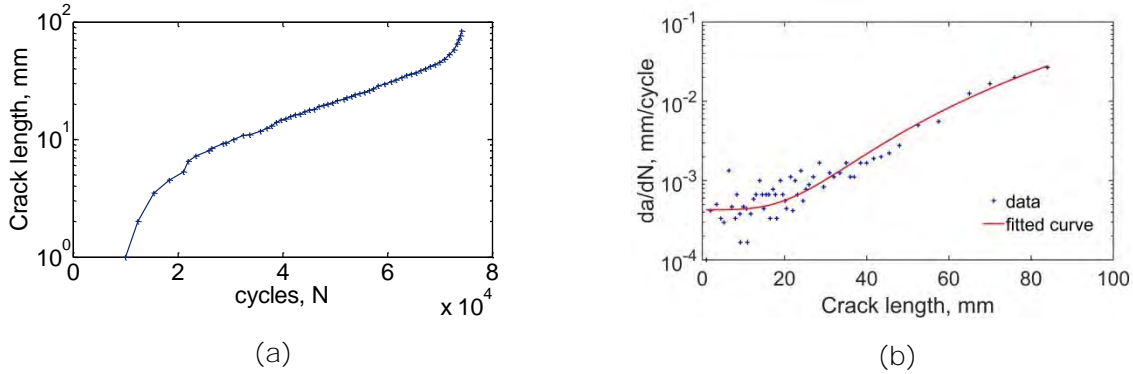


Figure 2. Crack growth with number of cycles (a) and growth rate (b)

The fracture surface indicates three distinct zones of crack propagation shown in Figure 3. The first image represents zone of propagation after crack initiation. The length of this region (labelled zone I) is about 37 mm and it took 68,000 cycles to grow the crack by this length. This region is particularly characterized by striations in the fracture surface which are shown in figure 4. The second image represents crack propagation after zone I. In this region (Zone II), the pattern characterized by the striations is not present and the average rate of crack growth has increased significantly. The crack surface was inclined by approximately 45 degrees with reference to the loading direction. This region extends between crack lengths of 37 mm and 77 mm and it took only about 5700 cycles to grow the crack between the two lengths. The third type (Zone III) represents crack surface which particularly is characterized by v-shaped markings. This region continued for a length of 7 mm, after which complete rupture of the specimen occurred. Such differences in the surface profiles combined with the changing growth rates are likely to produce different AE source mechanisms and AE signal waveforms.

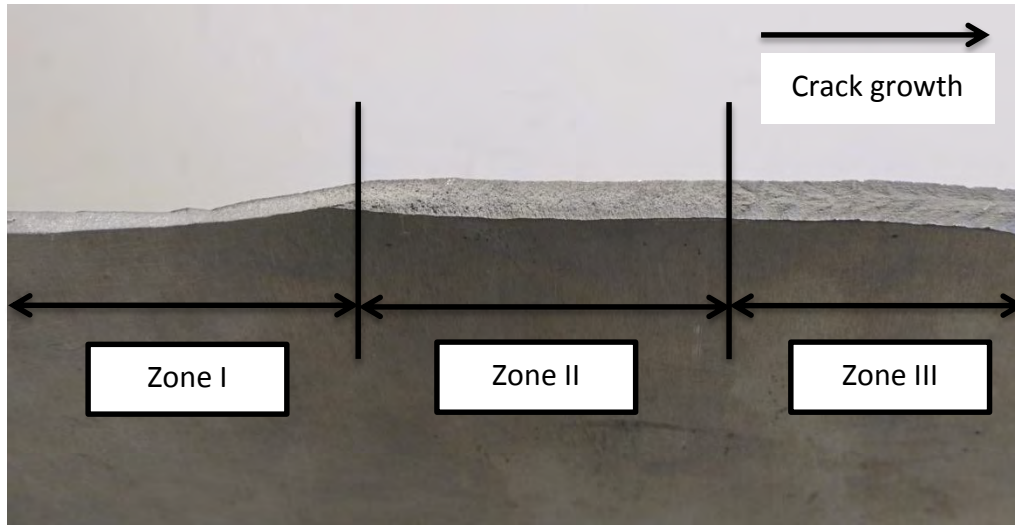


Figure 3. Three different fracture surface profiles

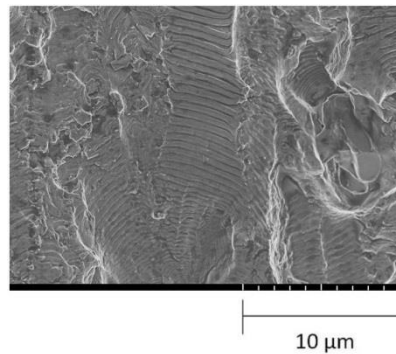


Figure 4. SEM image of Fatigue crack striations during Zone I of crack growth at 5000X

4.3.2 Acoustic emission behavior

During the test, over 40000 signal waveforms were obtained from the four channels (sensors). The signals from crack growth were filtered based on the time of arrival at the sensors located on opposite sides of the crack growth path and based on a load window which was set to select those waveforms obtained at 80% or more of the peak cyclic load. For the purpose of analysis, of the total 40000 waveforms, 6605 signal waveforms which satisfied the time of arrival requirement, which occurred at or above 80% of the peak load and which were detected by channel 1 were selected. Some signal waveforms were identified to originate from the areas where the end fixtures were mounted. These could possibly be associated with friction taking place between the fixture and the plate. Also, minor deformations taking place at the bolt connections could also give rise to AE signals.

Figure 5 shows the cumulative AE hit distribution as function of the number of cycles. The cumulative plot is generated for the filtered crack related AE hits from channel 1. The plot reveals that for longer portion of the curve, i.e, between, 20000 and 65000 cycles, the cumulative number

of AE hits increases at a steady rate on the semi-logarithmic y-scale plot. Above 65000 cycles, the cumulative number grows rapidly with the number of cycles. The total number of events obtained until 68, 000 cycles which corresponds to zone I of crack growth, however, was less than a tenth of the total number of events obtained from the test. Significant portion of the cumulative number was generated during the last 6000 cycles before rupture. This is confirmed by the curve on the plot after 68, 000 cycles.

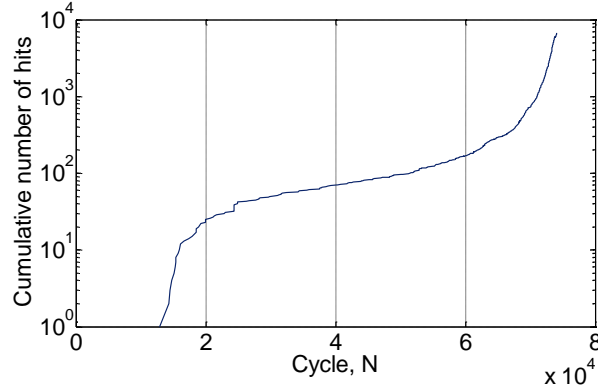


Figure 5. Plot of cumulative hit distribution

In addition to the cumulative occurrence of events, individual and cumulative distributions of features of the waveforms were examined to see the relationship between the crack growth and the features. Figure 6 shows the individual and cumulative distributions of three features: amplitude, duration and counts. It can be seen that, during the first 37 mm of crack growth (68, 200 cycles), the rate at which the events were generated was lower and only about 500 crack growth events were generated. The events during this portion of the test were characterized by lower amplitudes, durations and counts. 63 % of the events from this region had amplitudes less than 40 dB, 72.2 % of the events had duration less than 50 μ s, and 88.4 % had counts of 10 or less. After 68000 cycles, large number of events with amplitudes of 40 dB and above were noticed. During zone II of crack propagation, which is between 37 mm and 77 mm, only 42 % of the events had amplitudes less than 40 dB and 58 % had durations of 50 μ s or less. As the crack advanced into zone III, of those events obtained before rupture, i.e, between crack lengths of 77 mm and 84 mm, only 22 % had amplitudes less than 40 dB. The percentage of those events with durations less than 50 μ s went down to 37 % and 55 % of the events had counts of 10 or less in contrast to 88.4 % during zone I of crack growth.

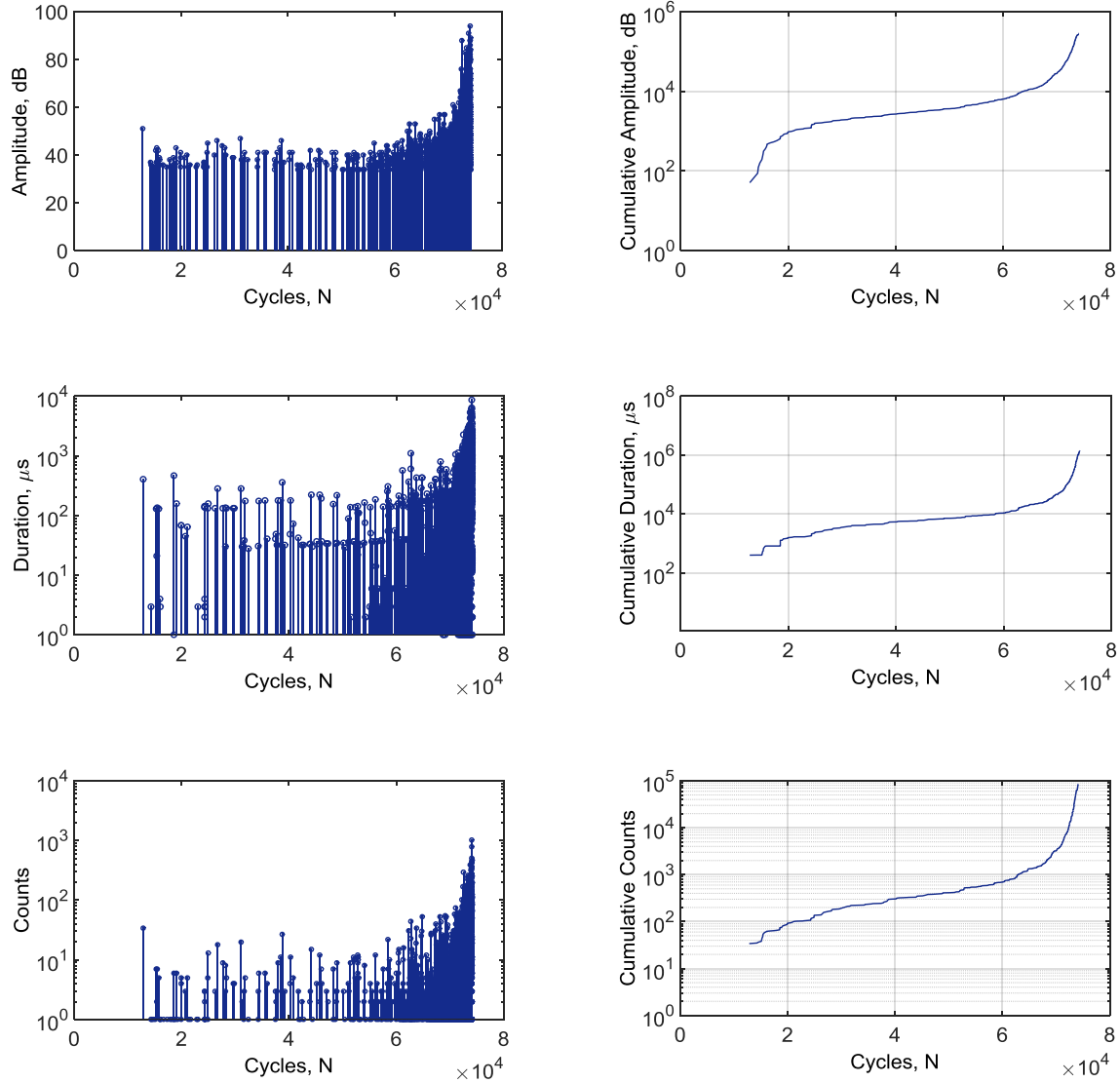


Figure 6. Plots of cumulative and individual distributions of AE features from the test

4.3.3 Evolution of waveforms with crack growth

The waveforms received at later stages of the test appeared to occur with different features. This was explanatory that crack propagation near failure of the specimen produced waveforms with different features than those at earlier stages. This could be explained by evolution of source mechanisms and change of source to sensor distance among others. These changes in the waveform features due to crack propagation were further examined through correlations made among the waveforms. A total of 6605 waveforms were assigned to multiple groups of successive waveforms. A total of 12 groups of 500 signal waveforms and a group of 605 signal waveforms were generated. The waveforms in each group were correlated among each other to determine what type of waveforms occurred in large numbers at each stage of crack growth and identify the distinctive

features of these waveforms. Of particular interest in this case were identifying traits corresponding to the three crack growth zones, Zone I thru Zone III.

The correlations used in the analysis are explained by Figure 7. As shown in the sketch, the first waveform in the group of 500 waveforms is correlated with the rest of the waveforms in the group. Those waveforms that exhibited correlation of 85% or more with the first waveform form a cluster. A new dataset is generated for second set of correlations by eliminating the well correlated waveforms. In the second correlation, the first waveform from the new dataset is correlated with rest of the waveforms in the dataset and, similar to the previous step, the well correlated waveforms form another cluster. This procedure continues until the entire waveform dataset in a group is exhausted. The same set of iterative correlation procedures were applied to each of the 13 groups of waveforms.

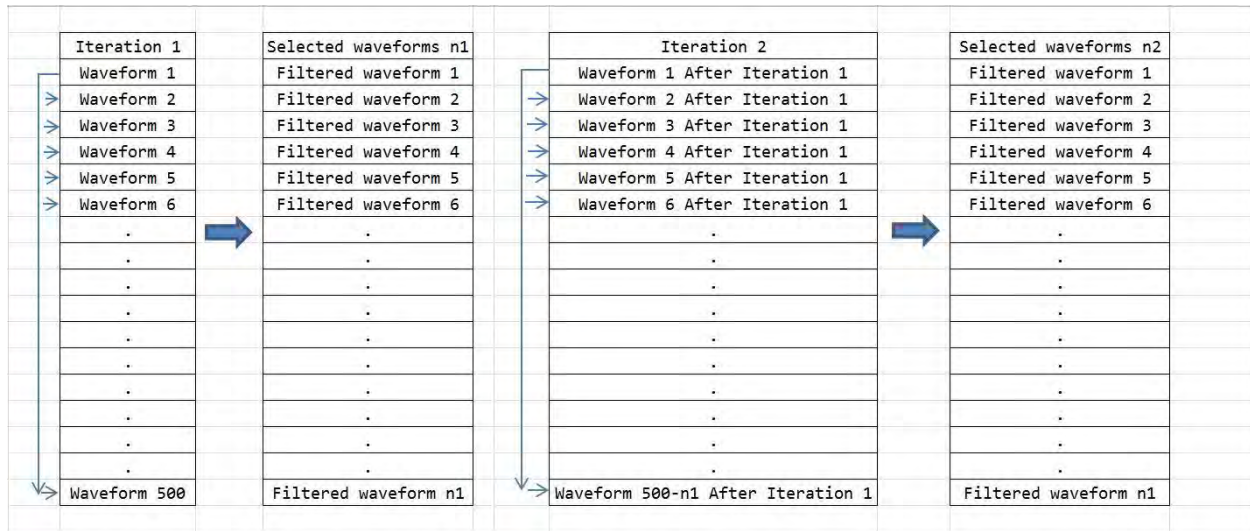


Figure 7. Correlation scheme for each group of 500 waveforms

The application of the correlation algorithms on the waveforms resulted in different number of clusters in each group of waveforms. Some clusters in a given group of 500 waveforms had only one element implying distinctive nature of the source event as compared to the rest of the waveforms in the group. Some clusters have close to 100 waveforms indicating high repetitiveness of successive source events, in particular. In this research, after consideration of several choices, cluster size of 30 or clusters with 30 or more members were considered for further analysis and interpretation.

Figure 8 shows three sample waveforms and their wavelet diagrams. The wavelet diagrams were generated by AGU Vallen wavelet software. The waveforms were selected from the clusters which were obtained at the three crack growth profiles highlighted earlier. The first waveform was obtained from the dominant cluster in the first group of waveforms. This group contains waveforms largely from Zone I of crack growth after crack was initiated. The events in this region were being recorded at a slower rate than later stages primarily because of lower amplitudes. It can be seen that during the initial stages of crack growth (Zone I), the waveforms which occurred in

large numbers as compared to others had weaker antisymmetric (A_0) components which is seen both in the waveform and the wavelet diagram. Other clusters with smaller size were assessed and about 80 % of the waveforms had A_0 components which in amplitude were 25% or less of the symmetric (S_0) amplitude. The frequency of the S_0 part was between 200 and 500 kHz as shown in the wavelet diagram.

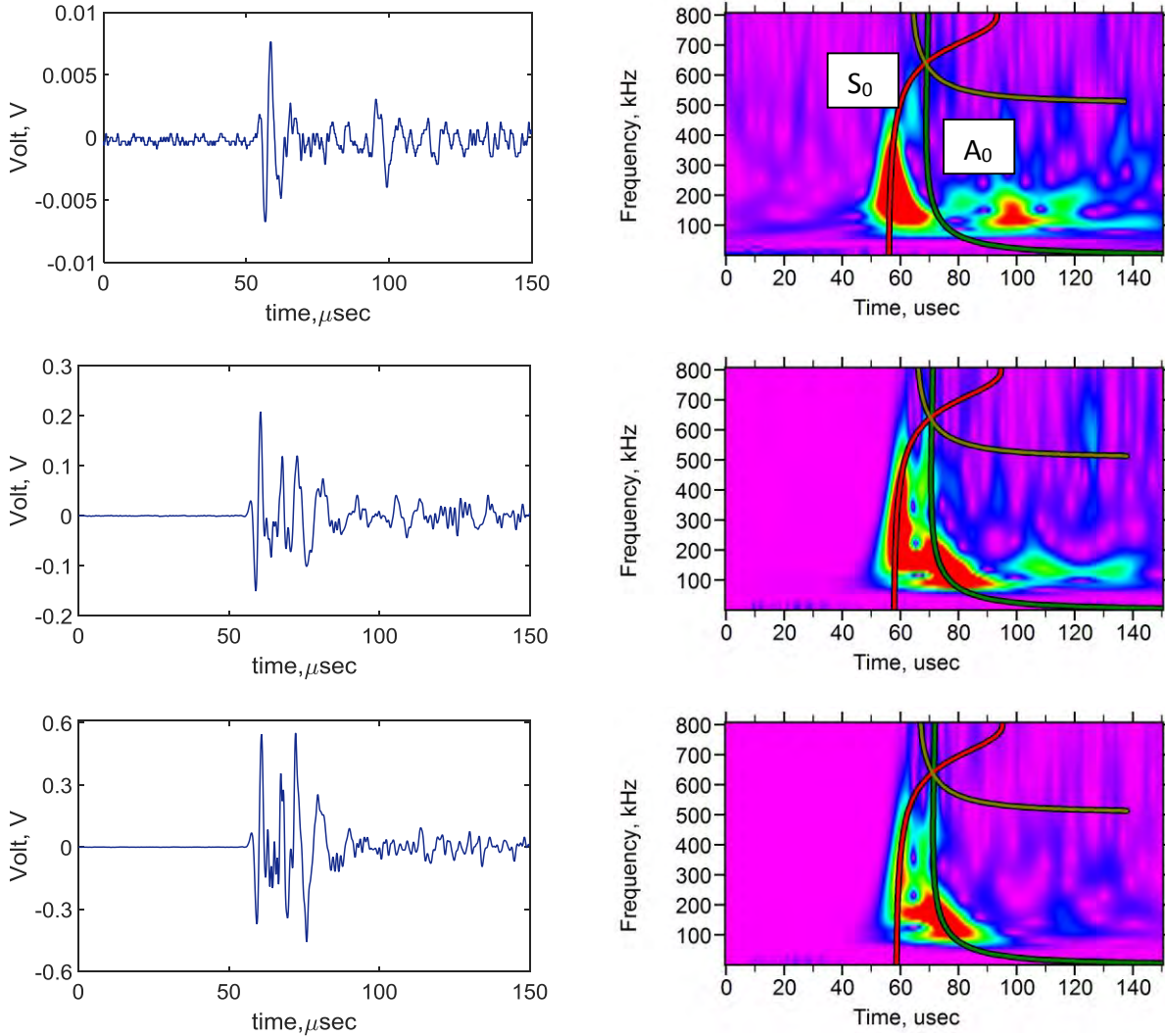


Figure 8. Sample cluster waveforms and their wavelets for events obtained at various stages.

The second waveform was taken from the clusters obtained at the shear type crack propagation (Zone II). Nearly 5500 crack related AE events were obtained during this span of crack length. All of the groups of signal waveforms which fell in this region had multiple clusters. The composition of wave propagation components in the waveforms which occurred in large numbers varied significantly. Between 37 mm and 66 mm of crack growth, the clusters had waveforms in which the A_0 amplitudes varied between 25 to 80 % of the S_0 amplitudes. Beyond this length, i.e. up to crack length of 77 mm, some of the waveforms had A_0 amplitudes which

were larger than the S_0 amplitudes by 10 to 20 %. The frequency of the S_0 components was mostly between 200 kHz and 500 kHz while that of the A_0 components was between 100 kHz and 250 kHz.

The third waveform was obtained from the region which was close to rupture of the specimen (Zone III). The waveforms which occurred in large numbers as compared to others had stronger antisymmetric modes. Most of the groups which fell in this region had multiple clusters. The majority of the waveforms had stronger A_0 modes with amplitude larger than the S_0 modes by up to 70%. Particularly, the last group of 605 signal waveforms had clusters all of which contained stronger A_0 modes. The peak amplitudes of these signal waveforms range between 35 dB and 94 dB. The frequency of the S_0 components was between 200 kHz and 500 kHz while that of the A_0 part was between 100 kHz and 250 kHz.

Such differences in the wave propagation modes and other features are indicative of the changes in the features of received signal waveforms as the crack advances towards rupture. These changes are the result of multiple factors related to location and mechanism type among others. To demonstrate possible sources of variations in the wave components, two different events were numerically simulated and the same two events were experimentally repeated by means of lead break tests. The numerical waveforms were obtained for two events near the neutral plane and close to the surface of an aluminum plate. The results from each of these are shown in figure 9. The waveforms in these waveforms indicate that events near the neutral plane become highly dominated by S_0 wave modes and as the event location moves away from the neutral axis, the resulting A_0 component becomes stronger and tends to increase in peak amplitude. Such details were confirmed by various authors [15, 16] in the past. In addition, the radiation patterns of the respective wave modes combined with the relative locations of the sensors could affect the presence of the components in the detected signal waveforms.

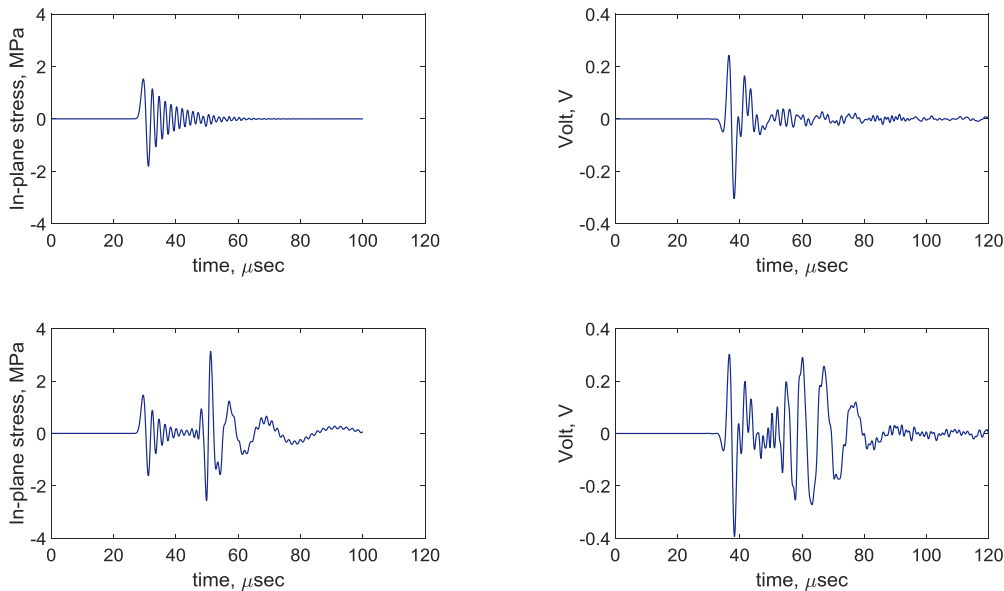


Figure 9. Numerical (left) and experimental (right) waveforms from AE events near the neutral axis (top) and away from the neutral axis (bottom)

4.4 Summary and conclusion

In this paper, the variations which occur in the characteristic features of acoustic emission signals due to crack propagation were examined. A fatigue test was conducted on an aluminum plate by initiating and growing crack up to fracture. The acoustic emission related waveforms were recorded in the process. The waveforms were assigned to multiple groups and correlations were carried out to identify the dominant waveforms in each group. At early stages of crack growth, the waveforms had weaker A_0 components while close to rupture the A_0 modes become dominant in the majority of the waveforms. Apart from the wave modes, the individual characteristics of the waveforms were also indicative of the change in the crack growth rate. Larger amplitude and longer duration events were obtained close to the complete fracture of the test specimen.

Such AE based characterizations of fatigue crack growth are quite useful in AE based structural health monitoring. The variations in signal characteristics are indicators of the rate at which damage is propagating in a monitored structure. These results combined with the works of many other authors are deemed to contribute to the ongoing field of extensive research in the area of AE based structural health monitoring.

References

- [1] Aggelis D, Kordatos E, Matikas T. Acoustic emission for fatigue damage characterization in metal plates. *Mechanics Research Communications*. 2011;38(2):106-10.
- [2] Gong Z, DuQuesnay D, McBride S. Measurement and interpretation of fatigue crack growth in 7075 aluminum alloy using acoustic emission monitoring. *Journal of testing and evaluation*. 1998;26(6):567-74.
- [3] Roberts T, Talebzadeh M. Acoustic emission monitoring of fatigue crack propagation. *Journal of Constructional Steel Research*. 2003;59(6):695-712.
- [4] Grandhi G, Nkrumah F, Sundaresan M, Kemerling J, Thomas D. Monitoring fatigue crack growth in 7075 T6 aluminum using continuous sensor. *Smart Structures and Materials: International Society for Optics and Photonics*; 2005. p. 595-602.
- [5] Hossain M, Yu J, Ziehl P, Caicedo J, Matta F, Guo S, et al. Acoustic emission source mechanisms for steel bridge material. *REVIEW OF PROGRESS IN QUANTITATIVE NONDESTRUCTIVE EVALUATION: VOLUME 32: AIP Publishing*; 2013. p. 1378-84.
- [6] Yu J, Ziehl P, Zárate B, Caicedo J. Prediction of fatigue crack growth in steel bridge components using acoustic emission. *Journal of Constructional Steel Research*. 2011;67(8):1254-60.
- [7] Sause MG, Richler S. Finite Element Modelling of Cracks as Acoustic Emission Sources. *Journal of Nondestructive Evaluation*. 2015;34(1):1-13.
- [8] Lugo M, Jordon J, Horstemeyer M, Tschopp M, Harris J, Gokhale A. Quantification of damage evolution in a 7075 aluminum alloy using an acoustic emission technique. *Materials Science and Engineering: A*. 2011;528(22):6708-14.
- [9] Andreykiv O, Skalsky V, Serhiyenko O, Rudavskyy D. Acoustic emission estimation of crack formation in aluminium alloys. *Engineering Fracture Mechanics*. 2010;77(5):759-67.
- [10] Grondel S, Delebarre C, Assaad J, Dupuis J-P, Reithler L. Fatigue crack monitoring of riveted aluminium strap joints by Lamb wave analysis and acoustic emission measurement techniques. *Ndt & E International*. 2002;35(3):137-46.

- [11] Barsoum FF, Suleman J, Korcak A, Hill EV. Acoustic emission monitoring and fatigue life prediction in axially loaded notched steel specimens. *Journal of Acoustic Emission*. 2009;27:40-63.
- [12] Mukhopadhyay C, Sasikala G, Jayakumar T, Raj B. Acoustic emission during fracture toughness tests of SA333 Gr. 6 steel. *Engineering Fracture Mechanics*. 2012;96:294-306.
- [13] Zain M, Jamaludin N, Sajuri Z, Yusof M, Hanafi Z. Acoustic emission study of fatigue crack growth in rail track material. *National Conference in Mechanical Engineering Research and Postgraduate Studies (2nd NCMER 2010)*, Faculty of Mechanical Engineering, UMP Pekan, Kuantan 2010. p. 3-4.
- [14] Kordatos E, Aggelis D, Matikas T. Monitoring mechanical damage in structural materials using complimentary NDE techniques based on thermography and acoustic emission. *Composites Part B: Engineering*. 2012;43(6):2676-86.
- [15] Gorman MR. Plate wave acoustic emission. *The Journal of the Acoustical Society of America*. 1991;90(1):358-64.
- [16] Hamstad M. Acoustic emission signals generated by monopole (pencil lead break) versus dipole sources: finite element modeling and experiments. *Journal of Acoustic Emission*. 2007;25:92-106.

PART 5: NUMERICAL MODEL OF ACOUSTIC EMISSION GENERATION FROM CRACK EXTENSIONS

Abstract

The objective of the work performed under this section is to better understand important aspects of AE signal generation, propagation, and detection, so as to better relate AE parameters with fatigue crack growth in critical aircraft structures. We analyze the characteristics of crack related signals in thick and complex structures and develop models that accurately capture the physics of AE signal generation during incremental crack growth.

5.1 Introduction

The dynamic force history around the tip of a crack when the crack is experiencing incremental growth such as under fatigue crack results in the generation of acoustic emission signals. The temporal and spatial variation of such forces may be termed “AE source function.” Understanding of the AE source function responsible for the generation of acoustic emission signals (AE) is important in developing accurate numerical models. While attempts have been made in characterizing source functions of idealized sources such as glass capillary break or pencil lead break on the surface of plates, no direct relationship between propagating cracks and acoustic emission characteristics appear to exist.

AE signals due to static, quasi-static and fatigue loading as well as wear and corrosion have been extensively analyzed for different types of structures [1-5]. However, simulation of the AE event source is a challenge that researchers in AE community are attempting to solve [6-11]. In 1985 Scurby proposed that an AE source must be represented as a point source with two main assumptions[10]. Firstly, the source should be self-equilibrating and internal (non-external). Secondly, the force due to the defect extension is simultaneous and equal in each direction, sharing same time history. Numerical approaches such as finite difference, boundary element method, finite element method and finite integral method has been considered in deriving the AE signals this amongst others [11-15]. The Finite Element approach is widely accepted amongst the methods mentioned above. In case of finite element a point source cannot be utilized due to limitation of the type of mesh hence researchers have utilized a band-limited Green’s functions for quantitative acoustic emission evaluations. A detailed understanding of utilizing dipole sources in case of finite element is discussed by various authors [6, 11, 16, 17]. A mono pole type of loads such as lead break and electronic pulser are also utilized to simulate specimen experimentally [14, 18, 19]. Thereby, an attempt is made here in understanding the response of different types of sources on an aluminum 3D sample to compare with the experimental results.

5.2 Finite element source function analysis

A set of numerical simulations were performed to understand the response of the thick aluminum bar to the different types of sources. The aluminum bar considered was of 300mm × 50mm × 9mm size (Figure 10). Since stress waves at the frequencies considered experience negligible attenuation in aluminum an elastic finite element model with no attenuation was

considered. The model was discretized such that 1mm cube consist of eight solid elements. AE waveforms corresponding to five different types of sources were examined. The waveforms were generated for stress and displacement history corresponding to a location 25 mm from the source. Dipole sources of magnitude of 100 Newton and 1 microsecond duration were applied at the crack tip close to the front surface of the thick aluminum sample. The five different types of dipole sources along with the resulting waveforms are shown in Figure 2.

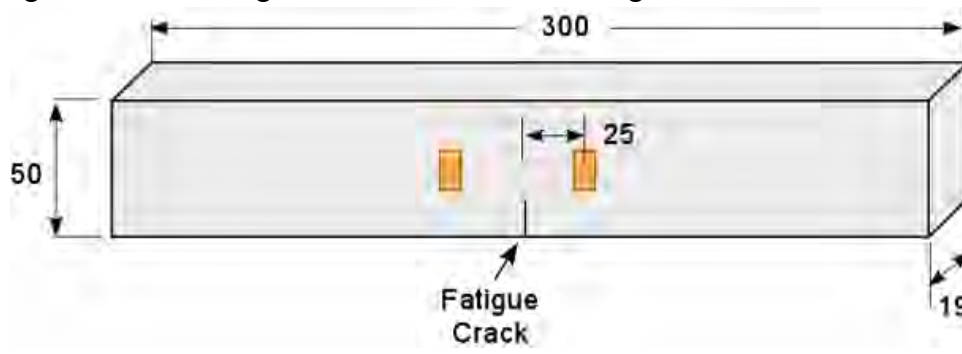
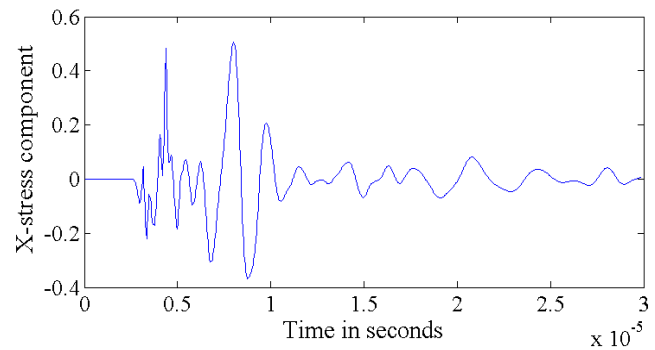
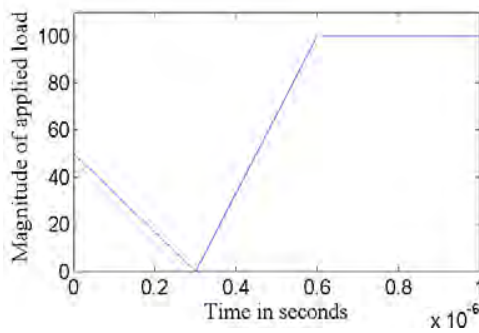
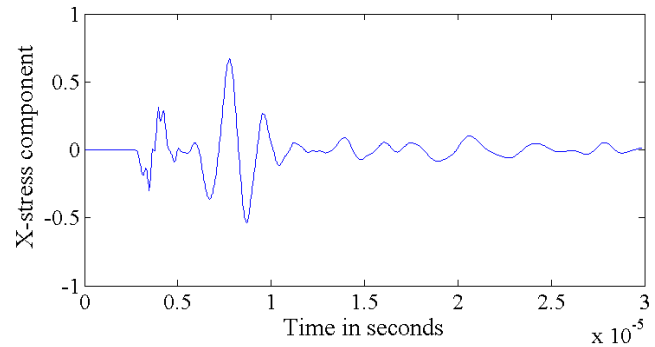
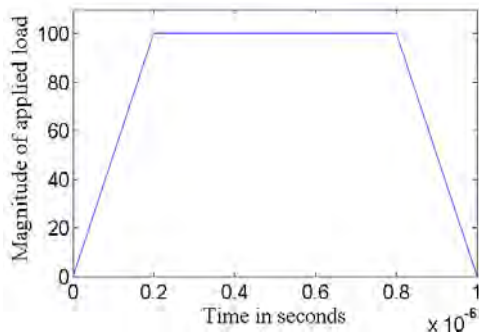


Figure 10 Sketch of the thick sample with sensors on the front surface



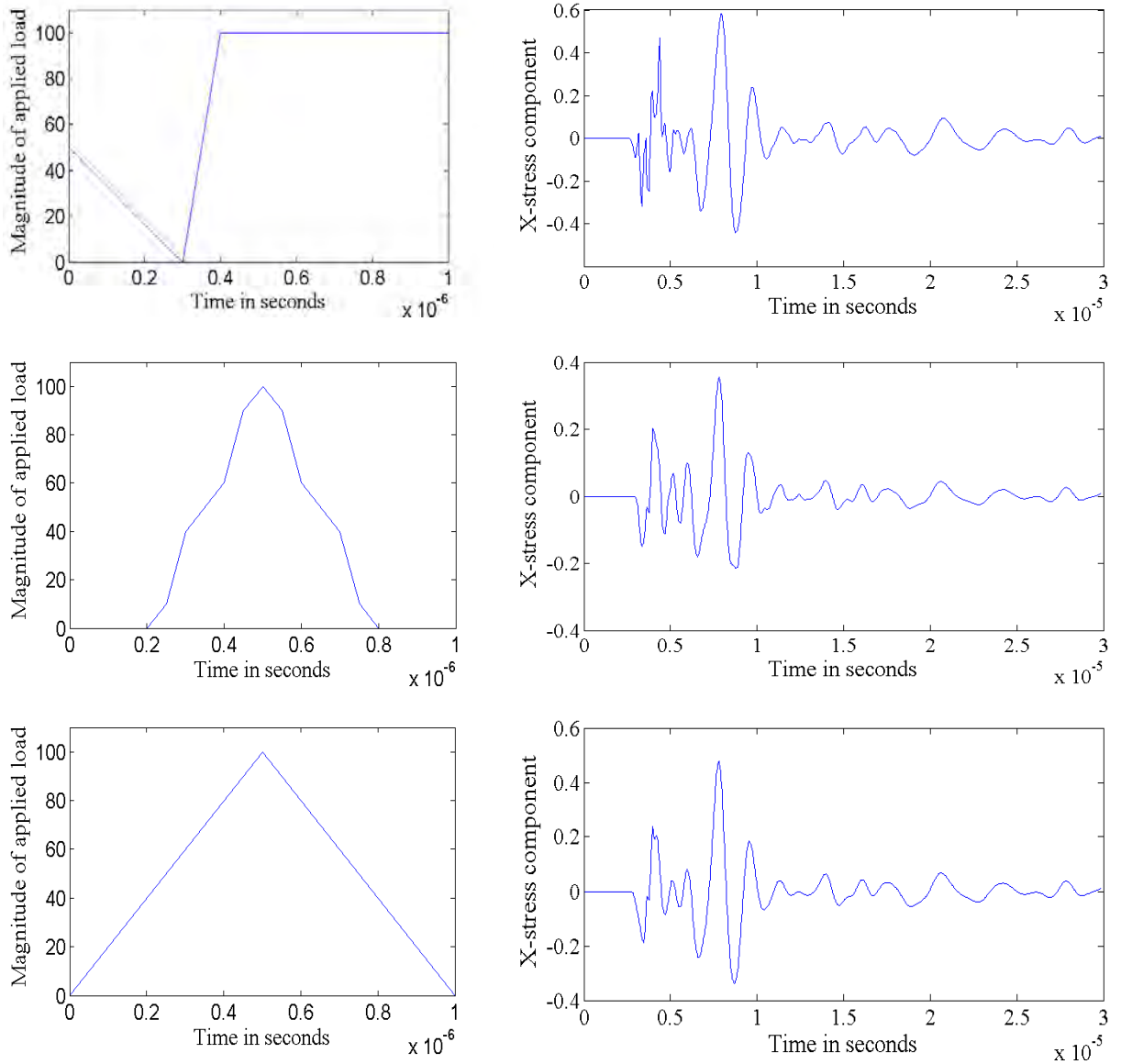
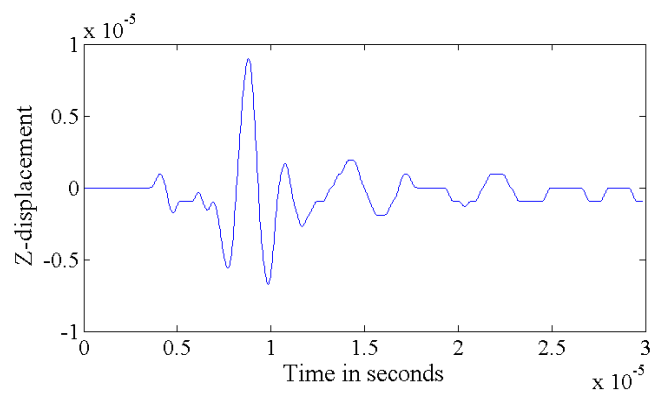
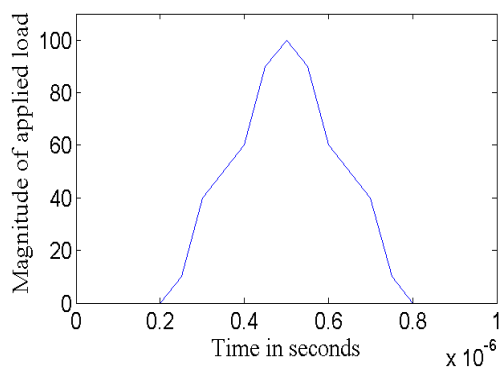
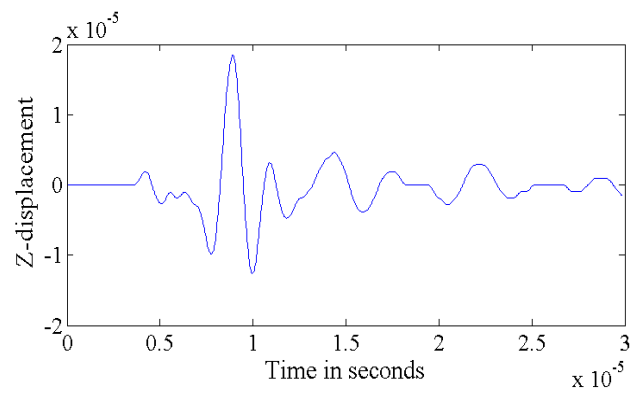
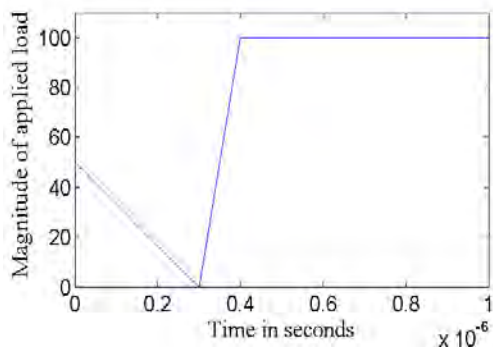
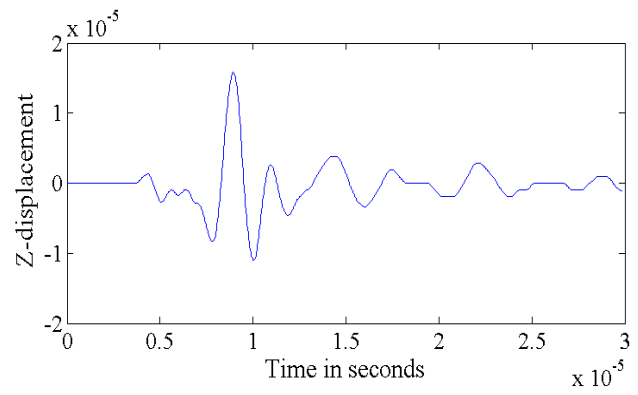
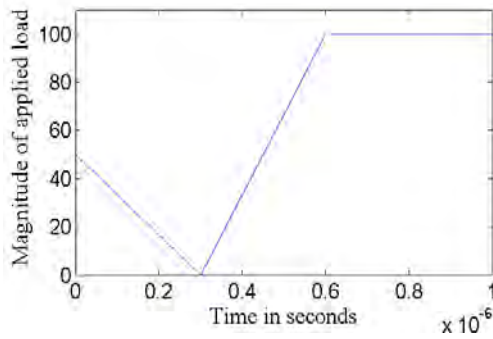
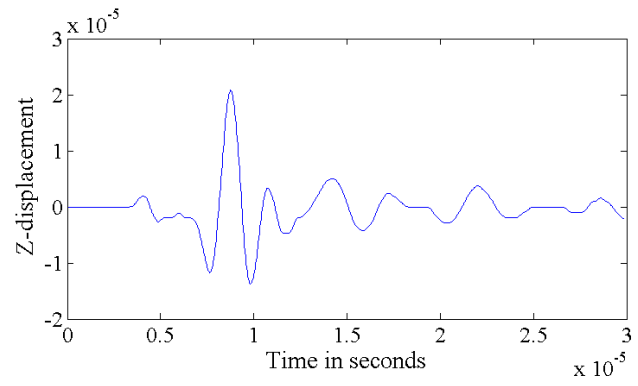
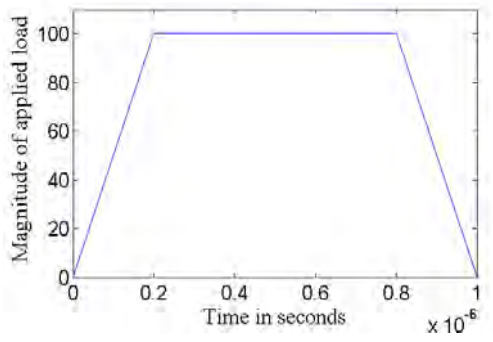


Figure 2 X-stress waveforms (RHS) due to five different types of loads (LHS) as observed at same sensor location

The first three sources were step functions, the next one was similar to Gaussian pulse and the last one was a triangular pulse. The waveforms generated due to these applied dipole sources had different features. Especially the initial pulse of the waveforms carried higher frequency components when excited by step functions. The trailing parts of the waveforms were similar with minor changes in amplitudes. The triangular and Gaussian type of load gave rise to smoother waveforms with lower amplitude signals in comparison.



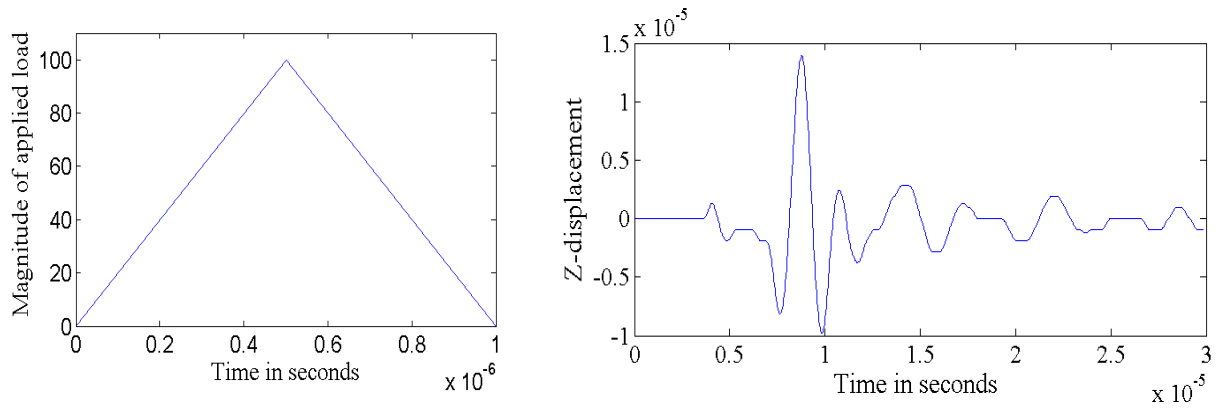


Figure 3 Normal displacement responses of the specimen due to different types of applied loads

Since the commercially available sensors detect out-of-plane displacements, normal displacements were also examined from these numerical simulations for each type of the applied sources. The Figure 3 shows normal displacement solution of the numerical model when five different typed of loads were applied. The changes observed in the displacements were not significant.

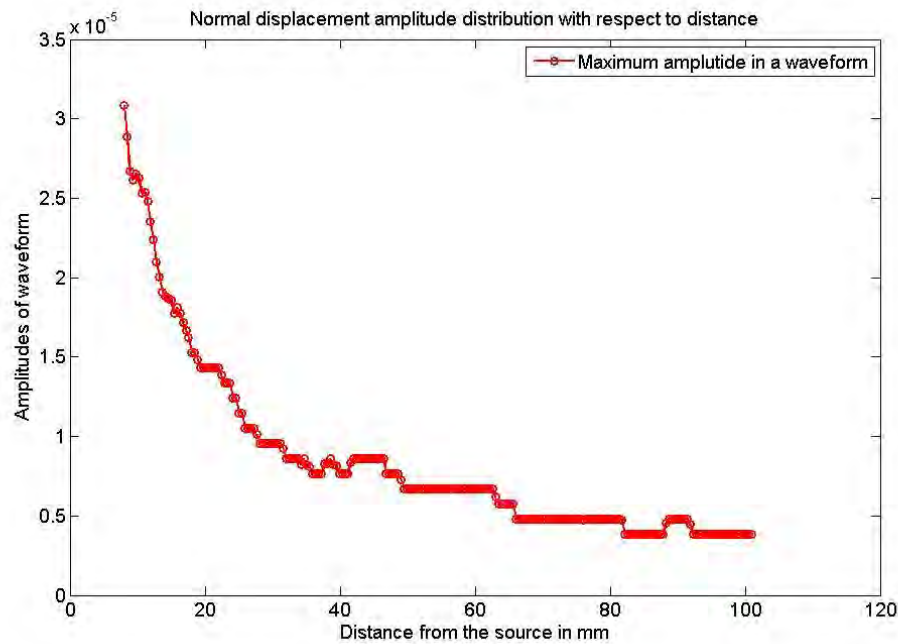


Figure 4 Distribution of amplitude with respect to the distance from the source of the normal displacement component due to the applied triangular load

Figure 4 shows the variation if the peak amplitude of the waveforms corresponding to normal displacements as a function of the distances between the source and sensor. Rapid reduction in amplitude of the signal was seen. The rate of reduction with distance seen in this thick specimen is significantly larger when compared to thin plates.

5.3 Advanced FEM models to simulate crack growth

In the previous section, the sources of AE signals were represented by known functions. The accuracy of such simulations obviously depends on how well such functions represent the time history of resultant force corresponding to the actual crack growth event. This time history is likely to vary based on the local conditions at the crack tip. Hence, it is necessary to simulate the material behavior at the crack tip. In this section results from the initial work on simulating incremental crack growth through finite element technique and the corresponding AE waveforms are reported.

The models used in this section are similar to those used in Fracture Mechanics studies such as Tie-break, element deletion and cohesive zone modeling. The phenomenon of energy release resulting from the process was captured by explicit time integration. In the research, the influence of various finite element formulations, element types, element sizes, boundary conditions was examined. Various options were attempted to execute crack growth including tie break and element deletion. Two dimensional as well as three dimensional finite element models were used in these studies. The analyses mostly involved combining implicit analysis to apply the quasi-static load and explicit time integration for modeling the wave propagation. The first case reported below corresponds to a two dimensional model, 3 mm thick and 600 mm long using 0.5 mm square elements. Two coincident nodes located on two adjacent elements were tied and failure was formulated based on the plastic strain experienced by the two adjacent elements. Figure 5 shows a waveform obtained from a simulation in which damage growth was simulated by release of the two nodes that were initially tied together at the same point, but were released from each other when the strain level crossed a specified failure strain. The waveforms correspond to a point at a distance of 100 mm from the fracture spot. Other than the quasi-static load on the specimen, no other force was applied in this finite element model. The waveform does have the usual symmetric and antisymmetric components of a typical AE signal. However, high frequency noise is superimposed in the signal. At this point, the source of this high frequency noise is not clear. One possibility is the clapping of the released nodes after the tiebreak. Out of plane displacement at the same location is shown in Figure 6.

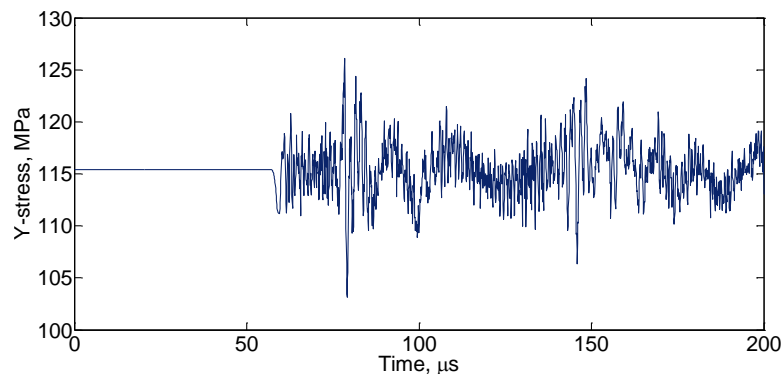


Figure 5 In-plane stress waveform from a 2D model at distance of 100 mm

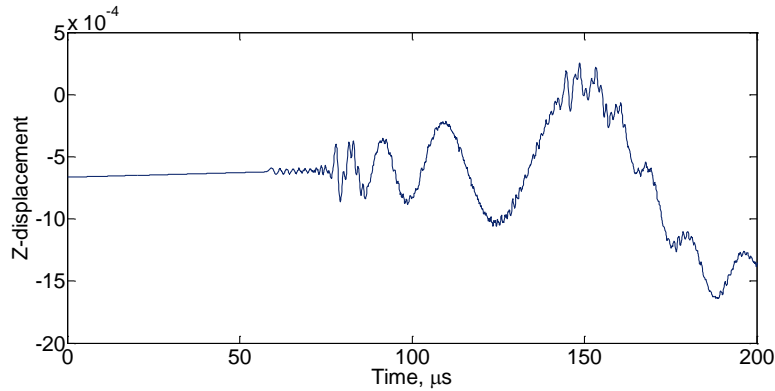


Figure 6 Out of plane displacement waveform from a 2D model at distance of 100 mm

5.4 Crack propagation modeling by element deletion

Among the many options considered, the command which was exhaustively attempted on several 2D models was simulation of crack growth by means of element deletion across a predefined crack path. The 2D model in this case was loaded under a quasi-static type loading. The solution to the problem was performed in two steps. The first stage till the fracture stress was solved using implicit analysis. The solution from the instance of fracture was performed using explicit analysis and the propagation of stress wave was analyzed using explicit time integration. Figure 7 shows the snapshots taken from the animation of stress wave propagating from the occurrence of damage at the center of the specimen. At the scales shown in this figure the stress waves are not clearly visible.

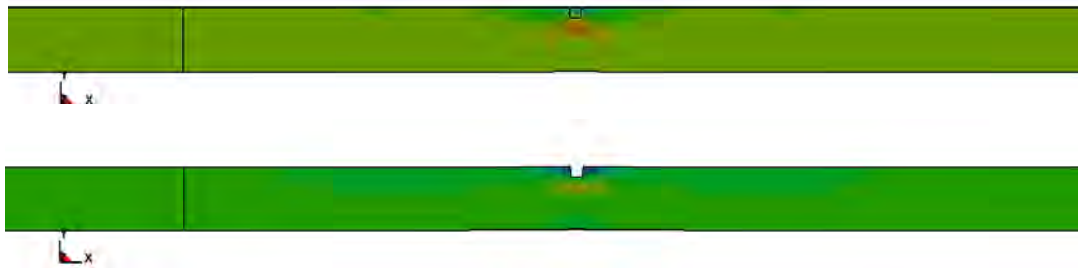


Figure 7 Snapshots from stress waveform simulation of element deletion

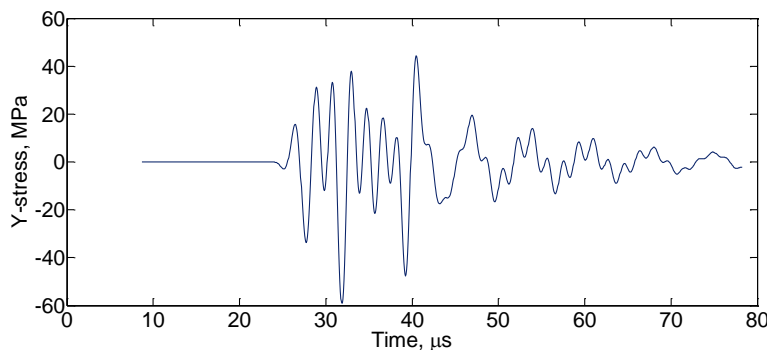


Figure 8 In-plane stress waveform at 50 mm obtained through element deletion

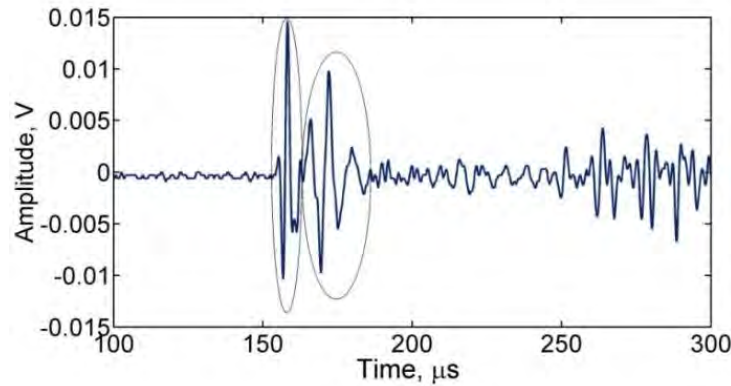


Figure 9 AE waveform from crack growth

Figure shows the waveform corresponding to the horizontal stress component at a location 50 mm from the damage location. The monotonic stress in the element due to the quasi-static loading was removed to reveal the stress wave due to crack advancing. The waveform shown here exhibits some similarity with the waveform from the application of pulse type load. For the purpose of comparison, waveform from actual crack growth experiment is presented in Figure . The fundamental symmetric and antisymmetric modes are contained in the stress waveform over a range of frequencies. The velocity of propagation as well as the dispersion behavior was comparable with defined dispersion curves of Aluminum in literature.

References

- [1] Al-Obaidi SMA, Leong MS, Hamzah R, Abdelrhman AM. A Review of Acoustic Emission Technique for Machinery Condition Monitoring: Defects Detection & Diagnostic. *Applied Mechanics and Materials*. 2012;229:1476-80.
- [2] Dornfeld D. Application of acoustic emission techniques in manufacturing. *NDT & E International*. 1992;25:259-69.
- [3] Lord Jr AE. Acoustic emission-An update. *Physical acoustics*. 2012;15:295-360.
- [4] Mba D, Rao RB. Development of Acoustic Emission Technology for Condition Monitoring and Diagnosis of Rotating Machines; Bearings, Pumps, Gearboxes, Engines and Rotating Structures. *The Shock and Vibration Digest*. 2006;38:3-16.
- [5] Wevers M, Lambrihs K. Applications of acoustic emission for SHM: A review. *Encyclopedia of Structural Health Monitoring*. 2009.
- [6] Sause MG, Horn S. Simulation of lamb wave excitation for different elastic properties and acoustic emission source geometries. *Journal of Acoustic Emission*. 2010;28:109-21.
- [7] Naber R-R, Bahai H. Analytical and experimental validations of a numerical band-limited Green's function approach for modelling acoustic emission waves. *Advances in Engineering Software*. 2007;38:876-85.
- [8] Naber R, Bahai H, Jones B. A reciprocal band-limited Green's function approach for modelling acoustic emission using the finite element method. *Journal of sound and vibration*. 2006;292:802-23.
- [9] Khalifa WB, Jezzine K, Grondel S, LHÉMERY A, CHATILLON S. Modeling of the Far-field Acoustic Emission from a Crack under Stress. *Proceedings of joint 30th European*

Conference on Acoustic Emission Testing and 7th International Conference on Acoustic Emission, EWGAE-ICAE 2012/2012.

[10] Scruby C, Baldwin G, Stacey K. Characterisation of fatigue crack extension by quantitative acoustic emission. *International Journal of Fracture*. 1985;28:201-22.

[11] Leser WP, Yuan F-G, Leser WP. Band-limited Green's Functions for Quantitative Evaluation of Acoustic Emission using the Finite Element Method. 54th AIAA/ASME/ASCE/AHS/ASC Structures, Structural Dynamics, and Materials Conference 2013.

[12] Achenbach JD. *Reciprocity in elastodynamics*: Cambridge University Press; 2003.

[13] Hamstad M, O'GALLAGHER A, Gary J. Modeling of buried monopole and dipole sources of acoustic emission with a finite element technique. *Journal of acoustic emission*. 1999;17:97-110.

[14] Prosser W, Hamstad M, Gary J, O'Gallagher A. Finite element and plate theory modeling of acoustic emission waveforms. *Journal of Nondestructive Evaluation*. 1999;18:83-90.

[15] Schubert F. Numerical time-domain modeling of linear and nonlinear ultrasonic wave propagation using finite integration techniques—theory and applications. *Ultrasonics*. 2004;42:221-9.

[16] Hamstad MA. Contrasts between the acoustic emission signals generated by monopole versus dipole sources. *Advanced Materials Research*. 2006;13:61-8.

[17] Gorman MR. Plate wave acoustic emission. *The Journal of the Acoustical Society of America*. 1991;90:358-64.

[18] Dunegan H. An alternative to pencil lead breaks for simulation of acoustic emission signal sources. The DECI report. 2000.

[19] Sause MG. Investigation of pencil-lead breaks as acoustic emission sources. *Journal of Acoustic Emission*. 2011;29:184-96.

PART 6 SHEAR HORIZONTAL WAVE DETECTION AND ANALYSIS IN FATIGUE CRACK GROWTH RELATED ACOUSTIC EMISSION SIGNALS

Abstract

The article demonstrates an ab-initio configuration of piezoelectric sensors to capture shear horizontal components of the acoustic emission waveform. The acoustic emissions from simulated crack growth and incremental crack growth in a cyclically loaded aluminum panel were detected by various acoustic emission sensors. Thereby, the devised sensor performance was assessed in comparison to other bonded piezoelectric sensors and resonant frequency acoustic emission sensors. Variation of the waveforms as a function of the location of the sensor with respect to the source event was considered. Additionally, advantages of Horizontal-shear wave above A0 and S0 are discussed to show the need of engineered sensors sensitive to detect shear horizontal waveform related to acoustic emission signals.

6.1 Introduction

The elastic stress wave is generated due to origination and/or expansion of defects within a stressed material is referred as acoustic emissions (AE). Over past half century AE signals are utilized for structural health monitoring as a powerful Non-destructive technique for detection, location and monitoring of cracks. The work of Kaiser [1] and Worlton [2] received great enthusiasm by researchers using ultrasonic techniques for nondestructive testing, and the results of this work continue to contribute to ultrasonic applications even as of today. However, research in acoustic emission testing, which began a few years later, largely ignored the applications of Lambs theory in the analysis of acoustic emission data [3-6]. The reasons can be attributed that most of the early AE experiments were conducted on small coupon specimens, where the theory was not applicable. The second reason was that ultrasonic researchers can transmit a harmonic wave to select the mode desired for a given plate thickness, while AE researchers were dealing with waves generated by a transient event, preventing such selection [7]. These transient ultrasonic waves generated as a result of rapid release of energy, resembles to a low strength pulse load or a lead break [8]. Prosser [9, 10] and Gorman [11, 12] discussed the use of plate wave theory in testing thin plate-like specimens with acoustic emission. The equation of motion for the small deformation in an isotropic plate with thickness h , in terms of displacement is given by:

$$(\lambda + \mu) \nabla (\nabla \cdot \mathbf{u}) + \mu \nabla^2 \mathbf{u} + \rho \mathbf{f} = \rho \frac{\partial^2 \mathbf{u}}{\partial t^2} \quad (1)$$

λ and μ in the Eqn 1 are Lamé constants, ∇ is del operator [13], ρ is the mass density and \mathbf{f} being the body force. According to plate wave theory wave propagation occurs in three modes: the extensional mode for which the particle motion is in the plane of the plate and in the direction of propagation; the flexural mode for which the particle motion is perpendicular to the plane of the plate; and the shear mode for which the particle motion is in the plane and perpendicular to the direction of propagation. The velocity for the mode waves are

$$C_e = \sqrt{\frac{\lambda + 2\mu}{\rho}}, \quad C_f = \sqrt[4]{\frac{D}{\rho h}} \sqrt{\omega} \quad \text{and} \quad C_s = \sqrt{\frac{\mu}{\rho}} \quad (2)$$

respectively, where, $D = Eh^3/12(1 - \nu^2)$ is bending stiffness, E is Young's modulus, ν is Poisson's ratio and ω is the circular frequency. Although this is true, in case of AE, only two types of waves: extensional and flexural modes or more widely known symmetric and antisymmetric modes are extensively studied and documented. The restriction was due to the detectability of shear modes. For purpose of this article only existence of Shear Horizontal (SH) wave mode is discussed theoretically. Mostly these AE signals are detected with the help of surface mounted Piezo-electric sensors, optical fibers or resonance sensors. With the present article the authors suggest a strong methodology and approach to identify shear waves detected from AE signals. The parameters of AE signals that has generated large amount of interest thus far are amplitude, duration, counts and energy all related to longitudinal and flexural modes. For the SH modes the information that is known and studied thus far is as follows [14-16]: Consider a plate parallel to the xy -plane, the displacement field for symmetric and anti-symmetric SH mode is given by

$$u_y(x, z, t) = [A \sin(qz) + B \cos(qz)]e^{(kx - \omega t)}. \quad (3)$$

The displacement field is derived from a reduced form of Eqn 1. In Eqn 3 A and B are arbitrary constants whereas term q is defined as $q = \sqrt{(\omega^2/c_s^2 - k^2)}$, where k is the wavenumber of the mode. Additionally, the cutoff frequency, phase velocity and group velocity, respectively, of SH modes can be derived as follows:

$$(fh)_n = \frac{nc_s}{2}, \quad c_{ps}(fh) = 2c_s \frac{fh}{\sqrt{4(fh)^2 - n^2c_s^2}} \quad \text{and} \quad c_{gs} = c_s \sqrt{1 - \frac{(n/2)^2}{(fh/c_s)^2}} \quad (4)$$

where $n = 0; 2; 4; \dots$ represents symmetric SH modes and $n = 1; 3; 5; \dots$ antisymmetric SH modes. It should be noted that when $n = 0$ the phase velocity and group velocity equals the bulk shear wave velocity, i.e. $c_{ps} = c_{gs} = c_s$, meaning the wave is dispersionless. However, it is not same for the cases where $n = 1; 2; 3; \dots$. Thus it could be concluded that although SH mode overall is dispersive the fundamental mode SH_0 is dispersionless. Additionally, as per Mindlin and Yang [17, 18] unlike extensional and flexural waves SH waves do not observe mode conversion upon reflection. Thereby, it is also known that group velocity of fundamental SH mode is higher than extensional mode and is lower than that of flexural mode [19, 20]. The statements above signifies the importance of detection of the SH waves above extensional and flexural.

The structure of the article is as follows, the setup of experiments is described at first place. Secondly the methodology implemented for bonding the sensors which allows the detection of SH modes is narrated. The results signify the working of the sensor array. Furthermore, the results of sensor array are compared with results as observed by other types of sensors. The article is thus concluded after showing the repetitive nature of the signals.

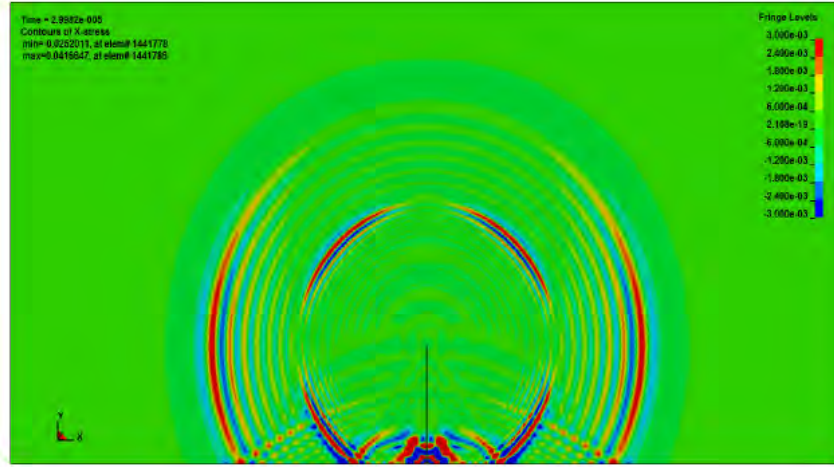


Figure 1. Response of the aluminum plate as observed at 0.3 μ sec due to the applied dipole load

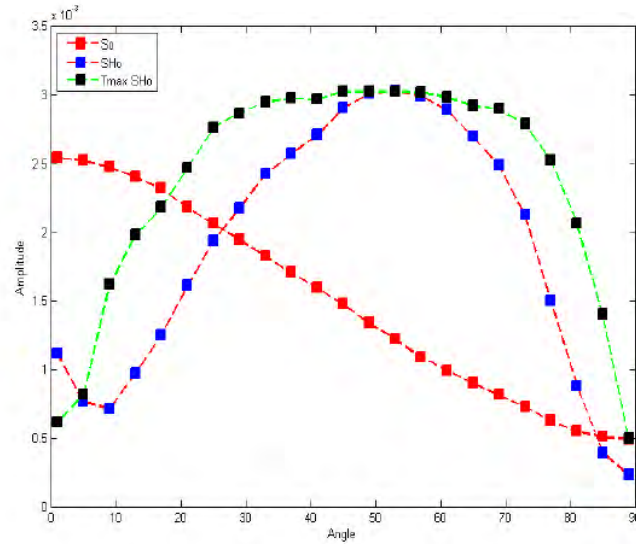


Figure 2. Comparison of magnitude of maximum amplitude of S0, SH0 and τ_{\max} deduced from the numerical results at equidistant elements located at various angles

6.2 Numerical analysis

A three dimensional aluminum plate specimen containing a central crack under tensile loading was modeled using Finite Element approach. The finite element model is a complete replication of the actual physical plate with dimensions 600mm \times 300mm \times 3mm modeled using roughly 3.5 million 8 node brick elements. Temporal and spatial resolution was taken into great consideration in order to accurately represent ultrasonic waves with frequencies up to 1 MHz. Hence, a high time resolution (1ms) and small element size was under prime consideration. In this study, a mesh element size of 0.5mm \times 0.5mm \times 0.6mm was used. The short triangular impulse load was applied along the thickness of the plate over the positive and negative x-direction at the

crack tip to represent a dipole load. The impulse lasted for 1 μ s where, at half of a micro second, the maximum strength was 1N. A response of such load at 0.3 μ s on the given specimen is shown in Figure 1. After careful observations the SH mode sensors were fabricated and configured [21, 22].

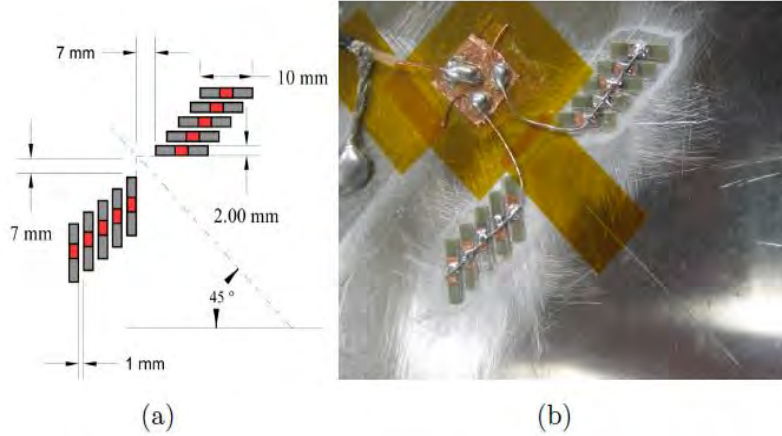


Figure 3. Diagram of the piezoelectric strips arrangement

With the help of numerical analysis a number of important observations were made (Figure 2). Presence of anti-symmetric modes was negligible due to symmetric load over the thickness. The maximum amplitudes of symmetric mode, and shear mode were observed over a range of elements located equidistant from the source at 120mm at different angle. Figure 2 signifies that the magnitude of maximum amplitude of the SH_0 is highest around 45° , whereas, that of S_0 is highest at 0° . Additionally, the magnitude of SH_0 around 45° , as compared to S_0 at 0° is about 16% higher. The PZT sensors as we know are only sensitive to either σ_{xx} or σ_{yy} . To overcome this limitation the magnitude of maximum amplitude for SH_0 was derived from the σ_{xx} and σ_{yy} by:

$$\max\{\text{amp}(SH_0)\} = \sqrt{\frac{\sigma_{xx}^2(SH_0^{\max}) + \sigma_{yy}^2(SH_0^{\max})}{2}}. \quad (5)$$

Furthermore, the graph of SH_0 coincides very well when compared with τ_{\max} at each selected elements, hence justifying the usage of SH_0 in the form narrated above. Thereby, the fabrication of the sensor strip arrays was initiated by etching away the nickel electrode coating on both ends of the top surface of the 10 mm \times 20 mm piezoelectric wafers, leaving a 3 mm \times 2 mm electrical contact in the center. A copper shim stock was then glued with Loctite superglue across the electrical contacts on the piezoelectric wafers. The next procedure was to carefully cut the piezoelectric wafers into 10 mm \times 2 mm strips. Five of these strips were then arranged parallel to one another with a spacing of 1 mm, but with their center points passing through a 45° line as shown in Figure 3. This array was then transferred with a piece of tape to the specimen site which had been roughened with sandpaper before being thoroughly cleaned and dried with 90% isopropyl alcohol. A thin layer of Loctite superglue was spread over the location and the sensor array was

held in place until the adhesive was set. Care was taken to minimize any adhesive welling up into the gaps between individual strips so that the strips would act as individual strips, independent of stresses experienced by adjacent strips in the array. A copper shim stock was then taped down across the electrical contacts on the strips and Kapton tape was used to insulate around the sensor array. It is important to note that shear sensor array 1 and 2 in Figure 3 are polarized in different directions (i.e. the upward face electrode of shear sensor array 1 was glued to the aluminum surface while the downward face electrode of shear sensor array 2 was glued to the aluminum surface).

The configuration and designing of the sensor ensured 1) the piezoelectric strips bonded to the specimen surface enables detection of the shear wave, 2) use a high aspect ratio strips targeted and placed parallel to x and y-planes acquired the respective shear components, and 3) an array of the strips connected together such that a reliable voltage output is generated. It should be noted that in this article the emphasis is on the detection of the SH_0 rather than the configuration of the sensors hence the empirical results are of greater interest.

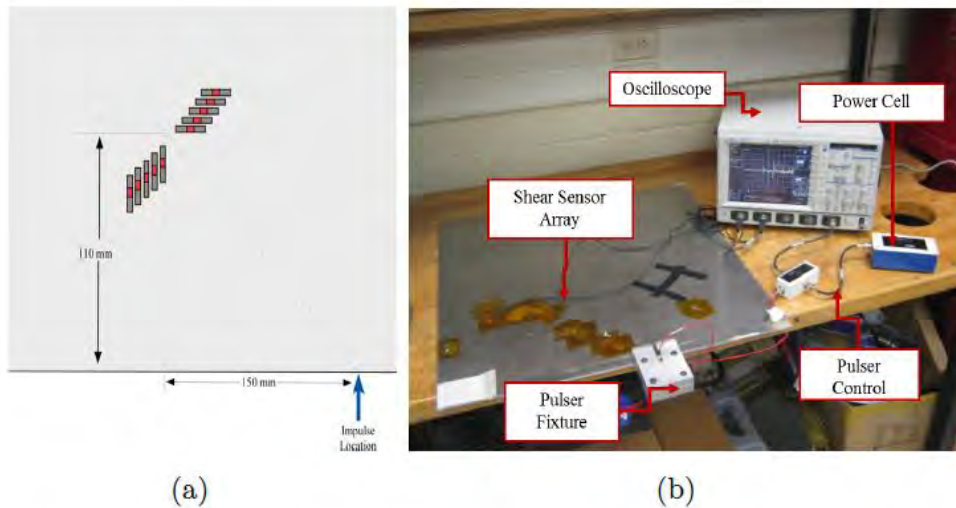


Figure 4. (a) Sketch of the sensor layout (b) experimental setup for pulser simulated emissions

6.3. Experimental setup

6.3.1 Simulated experiment

Prior to testing the ability of the shear sensor array to detect acoustic emissions from fatigue induced crack propagation, the sensor array was tested with simulated emissions from a piezoelectric pulser. The goal of these initial experiments was to establish the sensitivity of the sensor array to impulses arriving at various angles and from varied distances. The sensor array was bonded to an aluminum panel as noted above, and electrical leads were connected to the copper shim stock and the aluminum plate to measure the potential difference caused by the arrival of the acoustic emission wave fronts. The sensor was located 110 mm from the edge and measurements were taken with the pulser located at 15 mm increments along the edge up to a distance of 240 mm, as shown in Figure 4. This arrangement was selected to model the approach of a propagating

crack and the response of the sensor to changing distance and angle. The voltage output of the sensors was read by a LeCroy WaveJet 324 oscilloscope when triggered by the synchronous output from the pulser. A fixture was used to position the pulser along the edge of the specimen, which had been sanded, cleaned, and coated with petroleum jelly to ensure effective transmission of the impulse. The pulser excitation was set to 400V and the fixture ensured application of the impulse at the mid-plane of the specimen. The waveforms were filtered with a 20 MHz bandwidth and averaged over 16 events before being saved for further analysis.

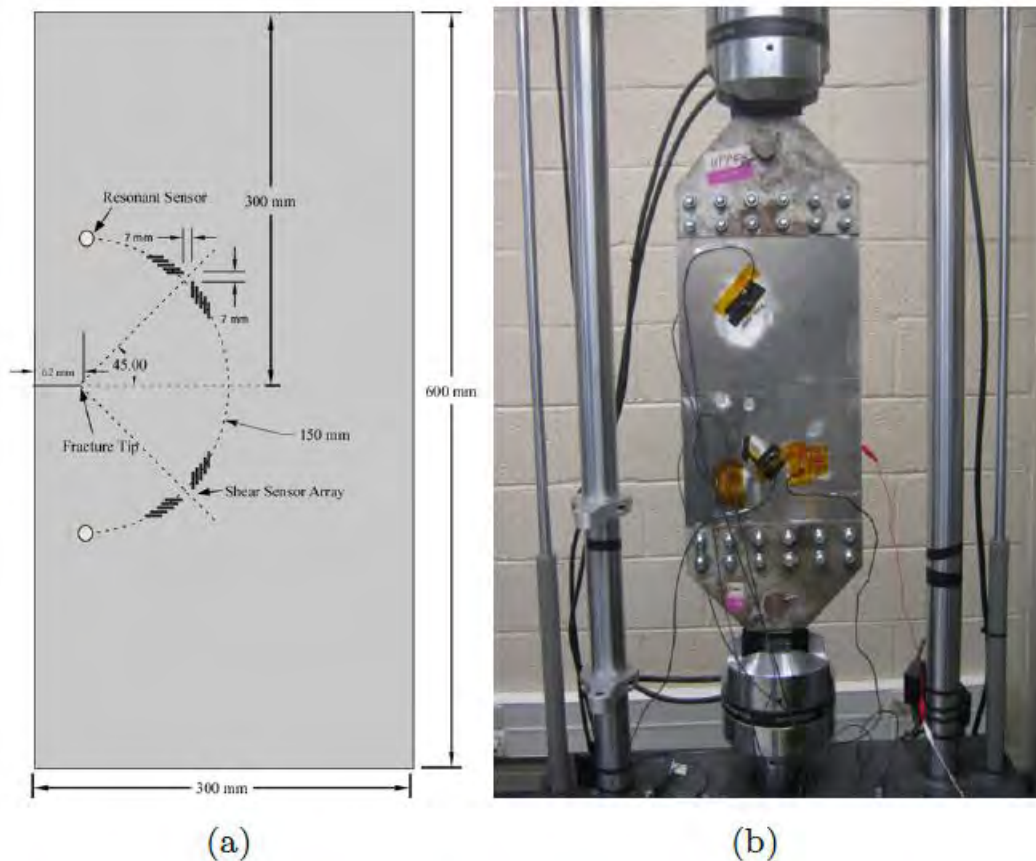


Figure 5. (a) Sensor layout for the test (b) Specimen mounted on the MTS (Material Testing system)

6.3.2 Fatigue test

Following the pulser tests, testing shifted to detection of acoustic emissions resulting from fracture propagation. The experiments were carried out on a panel of 2024-T3 aluminum measuring 600 mm \times 300 mm \times 3 mm thick. A slot 1 mm wide and 62 mm long was cut at the midpoint of the long side and the end of this slot was sharpened to a point, producing a stress concentration to exceed the fracture toughness of 34 MPa/m to promote crack growth. The specimen was clamped tightly into two fixtures, leaving the central 457 mm \times 305 mm portion exposed, and prior to being loaded into the MTS machine (Figure 5(b)). The specimen was subjected to tensile loads cycling from 890N to 43600N with a frequency of 2.5 Hz for a total of 4500 cycles to produce a 12 mm crack extending from the sharpened point of the slot.

The location chosen for the strip sensor array was at a distance of 127 mm from the existing crack tip at a 45 angle to the expected direction of travel (Figure 5(a)). A conventional PZT sensor was bonded to the specimen at a distance of 127 mm and perpendicular to the nominal direction of crack growth. The copper leads from the top of each of these sensors was soldered to the core of a coaxial cable, with the outer strands soldered to copper pads adhered to the sample as grounds. Two R30 resonance based sensors from Physical Acoustics Corporation were attached to the specimen on opposite sides the fracture. The timestamps from two sensors were compared to those of the bonded sensor and shear sensor array to validate that the measured signals were originating in the area of the crack tip. The layout of the various sensors can be seen in Figure 5. The specimen was subject to tensile loads cycling from 2.9 kN to 17.4 kN with a frequency of 1 Hz. The sensors were routed through a preamplifier (set at 40dB) to the AEWIn software where the threshold for collection was set at 35 dB. The waveforms were collected at 5M samples/s for 5000 samples, giving a sample time of 1 ms. The waveforms from the shear sensor array and bonded sensor were then manually screened for events taking place immediately prior to waveforms recorded by both resonant sensors, with the subsequent triggering of the resonant sensors being used to validate the origin as the crack tip and not an external source of noise.

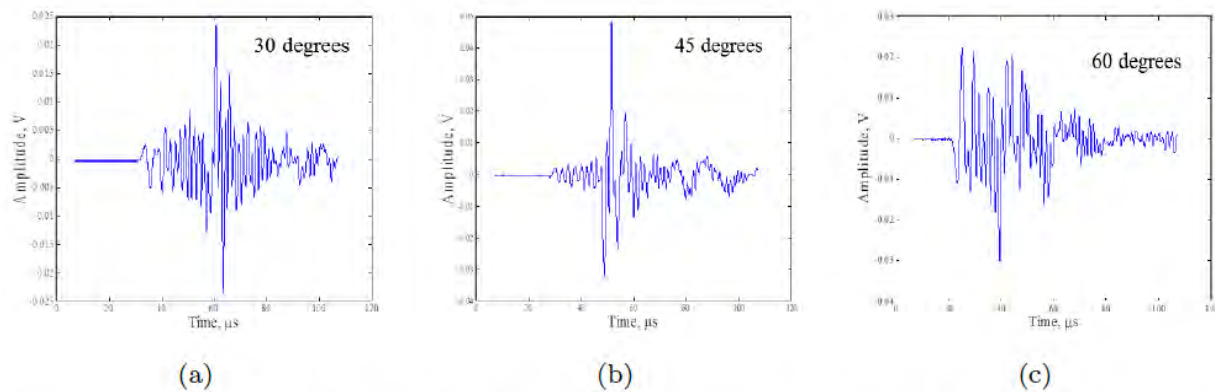


Figure 6. Waveforms at various angles

6.4. Results and discussion

6.4.1 Simulated results

The waveforms in Figure 6 were collected from the pulser experiments at 30, 45 and 60 degrees respectively. The results revealed evidence of the shear wave. As was expected, the shear component was small when the distance to the pulser was the greatest (from Figure 4(a)) and the angle of approach was small (Figure 6(a)). The different velocities of the various modes is also evident in Figure 6(a), where the greater distance has allowed more time for the peaks of the S_0 and SH_0 to separate compared to the shorter distance of Figure 6(c). Hence it can be summarized that between 30 and 60 degrees, the shear horizontal component is evident but as the angle of incidence approaches beyond 45 degrees the shear horizontal component subsides or becomes

nonexistent. From simulations, the peak response of the shear sensor was anticipated along an angle of 45° . The evidence of the same is found in Figure 6(b).

While working with various distances and angles, a number of remarks were made. The waveforms collected at the farthest distance were the noisiest, but the shear mode peak was clearly evident. The shear sensor gave highest peak when located at 51° from the pulser. This discrepancy is attributed to the fact that both distance and angle are changing with pulser movement in this experiment and the combination of sensor sensitivity and distance achieved a maximum response at an angle of 51° and distance of 142 mm. As the distance decreased and the angle increased from 60° to 90° , the magnitude of the shear component was seen to decrease and then disappear completely. The magnitude to the S_0 component however continued to increase in this region and peaked when the angle between the pulser and the sensor array was 90° and the distance between the pulser and the sensor was at its minimum.

6.4.2 Fatigue test results

Fatigue loading of the aluminum panel yielded a large number of events which were registered on the shear sensor array, bonded sensor, and resonant sensors. While noise sources did provide many waveforms that could not be confidently attributed to the crack tip region, there were a significant number of events where the triggering of the bonded sensor and shear sensor array was quickly followed by the triggering of the resonant sensors, indicating an origin at or near the crack tip. That the crack was seen to grow of 1 mm during the cycling that produced these waveforms is seen as further indication that at least some of these emissions can be attributed to crack growth. Furthermore, the waveforms from the wafer sensor, shear sensor array, resonant sensor output, were compared to identify the shear horizontal component of the crack growth related acoustic emission signals. It is well known that incremental crack growth over a microscopic area located at the neutral axis leads to predominantly S_0 mode in the waveform and similar crack growth located far from the neutral axis leads to predominantly antisymmetric A_0 mode in the waveform. These details were observable in bonded wafer sensor due to wide band sensitivity whereas, the resonant frequency sensors lag in providing such information. Hence to identify the proximity of incremental crack growth to the neutral axis, the ratio of peak values of the A_0 component to the S_0 component was determined from the PZT waveform sensor. If the incremental crack growth is close in proximity to the neutral axis, then the ratio of peak values of the A_0 component to the S_0 component should be generally less than one. However, if the incremental crack growth is near in proximity to the surface edge, the ratio of A_0 component to S_0 component should be in general greater than one. In the waveforms resulting from fatigue crack growth, the ratio of A_0 to S_0 ranged from 0.4 to 8.5.

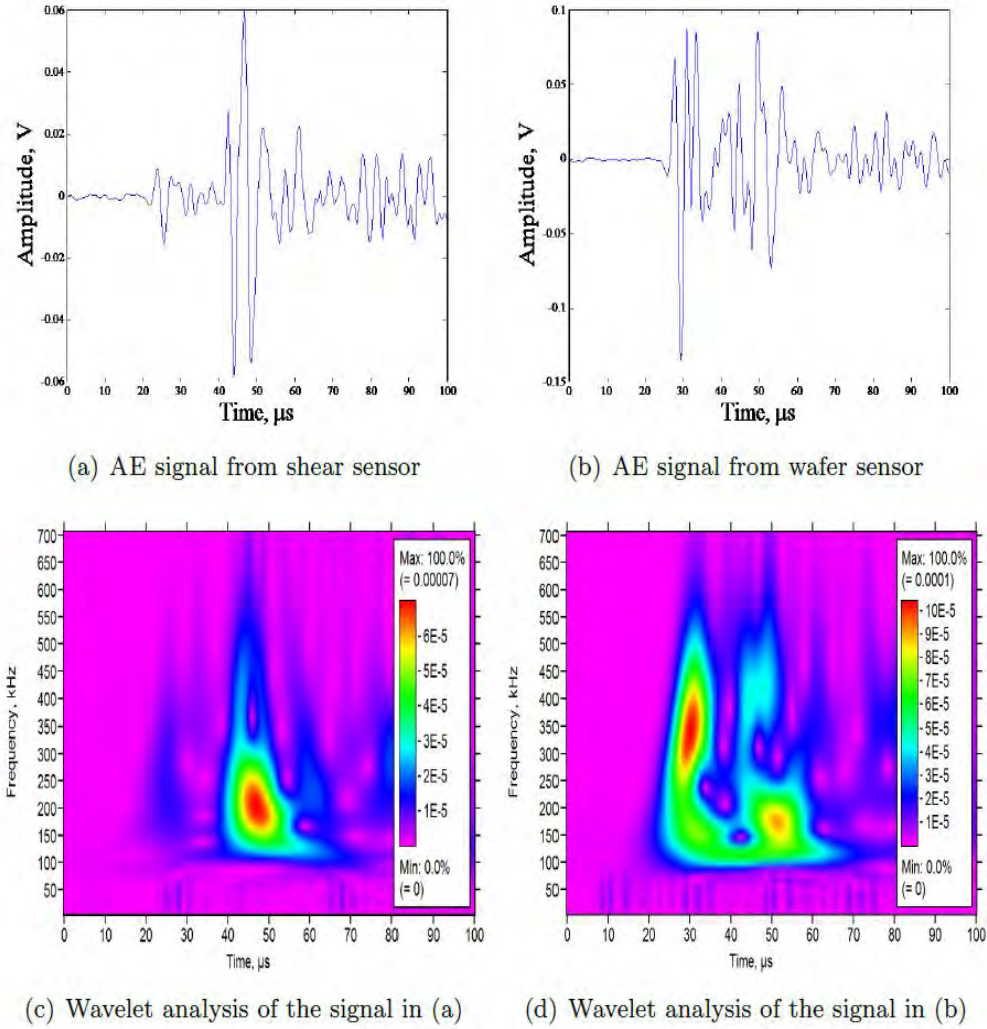


Figure 7. Typical AE waveforms as observed on shear and wavefr sensors due to crack growth at neutral axis

Figure 7(a) and 7(c), compares acoustic emission waveform with its corresponding wavelet analysis of the same event from the shear sensor, where the crack growth appears to be propagating at or near the neutral axis, as the ratio between A_0 to S_0 from the PZT waveform sensor was 0.45. Figure 7(a) delineates a SH component of peak amplitude 0.06 V at around 45 μs at frequency approximately 200 kHz. Additionally, the Figure 7(b) and 7(d), compares acoustic emission waveform with its wavelet analysis of the same event from the wafer sensor.

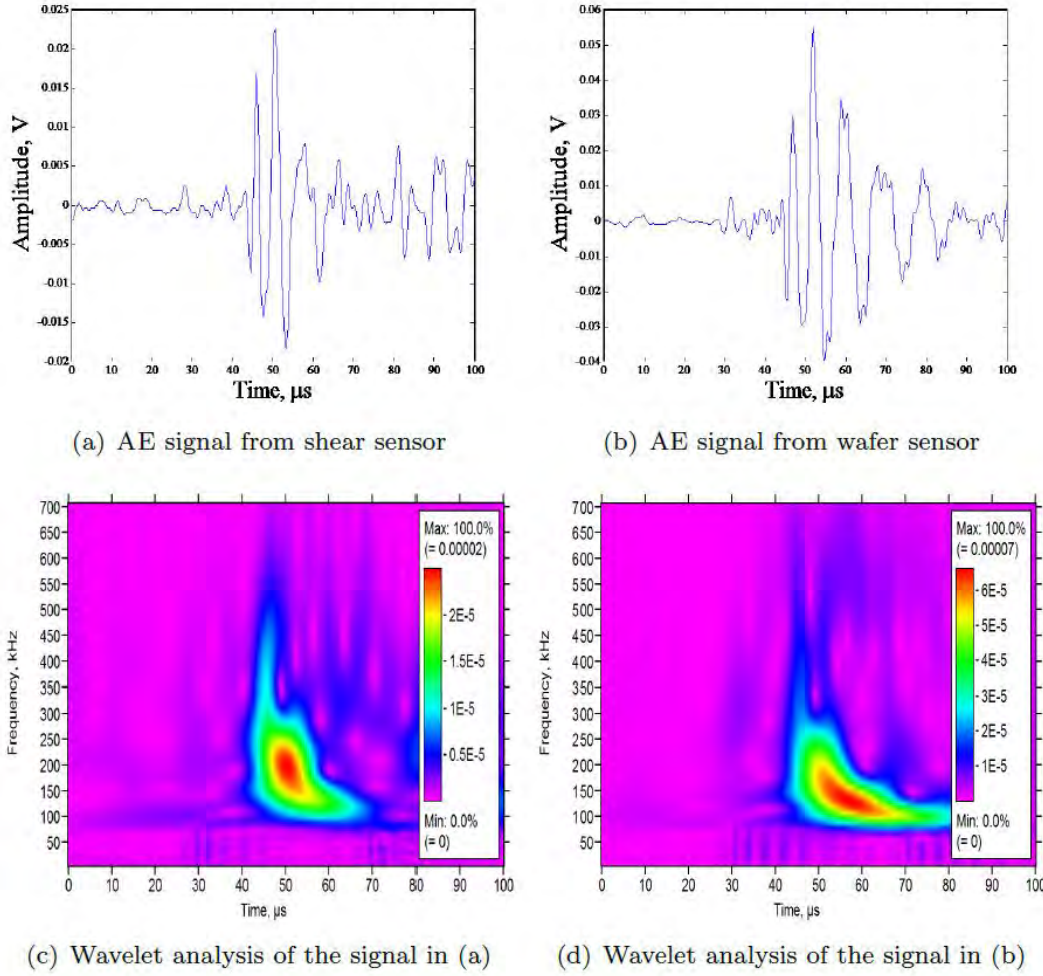


Figure 8. Typical AE waveforms as observed on shear and wafer sensors due to crack growth at or near surface

The acoustic waveform (Figure 7(b)) exhibits S_0 component of peak amplitude 0.15 V at 30 μs and A_0 component at approximately 50 μs . Similarly, Figure 8(a) compares acoustic emission waveform with wavelet analysis (Figure 8(c)) of the same event from the shear sensor, where the crack growth appears to be propagating at or near the surface, as the ratio between A_0 to S_0 from the PZT waveform sensor was 8.3. Consequently, the waveform of the same event from the wafer sensor (Figure 8(b)) exhibits S_0 component of amplitude 0.008 V at 30 μs and A_0 component of peak amplitude 0.05 V at approximately 50 μs . Whereas, Figures 8(c) and 8(d) shows the differences in the frequency pattern generated from their respective signals. Verification of the shear sensor array to produce repeatable shear horizontal waveforms were determined by plotting five consecutive waveforms obtained during fatigue crack growth after their amplitudes were normalized to span the range of -1.0 V to +1.0 V, so that they can easily be compared. To obtain this normalized amplitude, all voltage data points in each of waveforms was divided by the highest voltage value in the waveform. The five normalized waveforms were superposed in Figure 9. The figure shows that the actual shear wave components in AE signals corresponding to close sequence of crack growth events are nearly identical.

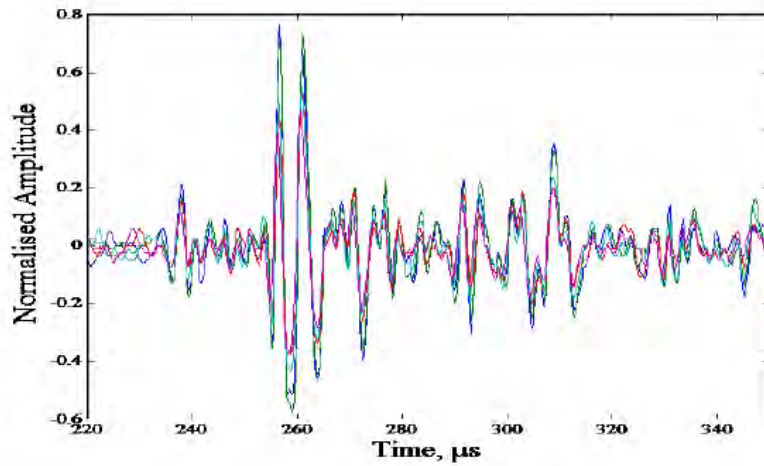


Figure 9. Normalized amplitude plot of the first five consecutive shear waveforms

6.5. Conclusion

The shear sensor array has been shown to clearly capture the shear mode of acoustic emission during both pulser simulation of acoustic emissions and the actual acoustic emissions emanating from the tip of a crack propagating due to cyclical loading. Commercial type sensors are more sensitive to asymmetrical component of the acoustic emission waveform and most noise signals (friction) have large A_0 . Bonded wafers are less sensitive to A_0 and hence have better noise performance, but both are incapable of detecting SH_0 component of the acoustic emission waveform. While this performance shows promise for the sensors, the level of noise present made clear identification of the wave element difficulties. The electrical connections to the sensors, the paths to ground, and the cable shielding are all being refined in an effort to reduce electrical noise in the signals. In addition to the electrical noise, the shear sensor arrays observed increase in noise and decreased sensitivity to the shear component during the later stages of the cyclical loading tests is believed to be a result of degraded bonding between the shear sensor array and the aluminum specimen.

References

- [1] Holcomb DJ. General theory of the Kaiser effect. International journal of rock mechanics and mining sciences & geomechanics abstracts: Elsevier; 1993. p. 929-35.
- [2] Worlton D. Experimental confirmation of Lamb waves at megacycle frequencies. Journal of Applied Physics. 1961;32(6):967-71.
- [3] Lamb H. On the propagation of tremors over the surface of an elastic solid. Philosophical Transactions of the Royal Society of London Series A, Containing Papers of a Mathematical or Physical Character. 1904:1-42.

- [4] Viktorov IA. Rayleigh and Lamb waves: physical theory and applications: Plenum press; 1970.
- [5] Ono K, Shibata M, Dunegan H, Hartman W. Advances in acoustic emission. Proc Int Conf, HL Dunegan and WE Hartman, Ed, Dunhart Publishing 1981.
- [6] Chow T. On the propagation of flexural waves in an orthotropic laminated plate and its response to an impulsive load. Journal of Composite Materials. 1971;5(3):306-19.
- [7] Pao YH, Gajewski RR, Ceranoglu AN. Acoustic emission and transient waves in an elastic plate. The Journal of the Acoustical Society of America. 1979;65(1):96-105.
- [8] William H. The Propagation Characteristics of the Plate Modes of Acoustic Emission Waves in Thin Aluminum Plates and Thin Graphite/Epoxy Composite Plates and Tubes. 1991.
- [9] Prosser W, Gorman M. Plate mode velocities in graphite/epoxy plates. The Journal of the Acoustical Society of America. 1994;96(2):902-7.
- [10] Prosser W, Hamstad M, Gary J, O'Gallagher A. Finite element and plate theory modeling of acoustic emission waveforms. Journal of nondestructive evaluation. 1999;18(3):83-90.
- [11] Gorman MR. Plate wave acoustic emission. The Journal of the Acoustical Society of America. 1991;90(1):358-64.
- [12] Gorman MR, Prosser WH. AE source orientation by plate wave analysis. 1991.
- [13] Auld BA. Acoustic fields and waves in solids: Рипол Классик; 1973.
- [14] Rose JL. Ultrasonic waves in solid media: Cambridge university press; 2004.
- [15] Graff KF. Wave motion in elastic solids: Courier Corporation; 2012.
- [16] Achenbach J. Wave propagation in elastic solids: Elsevier; 2012.
- [17] Mindlin RD, Yang J, Mindlin RD, Mindlin RD. An introduction to the mathematical theory of vibrations of elastic plates: World Scientific; 2006.
- [18] Mindlin RD. Thickness-Shear and Flexural Vibrations of Crystal Plates. Journal of Applied Physics. 1951;22(3):316-23.
- [19] Wang L, Yuan F. Group velocity and characteristic wave curves of Lamb waves in composites: Modeling and experiments. Composites Science and Technology. 2007;67(7):1370-84.
- [20] Neau G, Deschamps M, Lowe M. Group velocity of lamb waves in anisotropic plates: comparison between theory and experiments. REVIEW OF PROGRESS IN QUANTITATIVE NONDESTRUCTIVE EVALUATION: Volume 20: AIP Publishing; 2001. p. 81-8.
- [21] Sundaresan MJ, Williams WB. Structural health monitoring of shear waves in aluminum plates. 2011. p. 79820Z-Z-10.
- [22] Rajendra D, Knighton T, Esterline A, Sundaresan MJ. Physics-based classification of acoustic emission waveforms. SPIE Smart Structures and Materials+ Nondestructive Evaluation and Health Monitoring: International Society for Optics and Photonics; 2011. p. 79833H-H-8.

PART 7 ANALYSIS OF EXPERIMENTALLY GENERATED FRICTION RELATED ACOUSTIC EMISSION SIGNALS

Abstract

Acoustic emission signals generated by sliding friction between two flat steel surfaces are characterized. A test fixture to simulate the reciprocating motion between the two surfaces under controlled conditions is developed. Sliding friction under several combinations of surface roughness, relative velocity, and normal pressure was examined. Wideband AE sensors and instrumentation were used for acquiring and analyzing the acoustic emission signals. Acoustic emission events occurred primarily during the slip portion of the stick-slip cycles. AE waveform features obtained during these experiments were indicative of the tribological conditions. Frequency components in excess of 700 kHz were seen during these experiments. The characteristics of the experimentally observed acoustic emission signals were in general agreement with earlier numerical predictions. Friction related acoustic emission signals were distinguishable from those from other sources such as fatigue crack growth. The characterization of friction related acoustic emission signals is likely to be of value in many tribological and structural health monitoring applications.

7.1 Introduction

Acoustic emissions (AE) are stress waves generated in solids due to release of strain energy by a variety of mechanisms. A number of mechanical processes, including incremental crack growth, slip between surfaces that are in contact, and phase transformations in crystalline materials, can generate acoustic emission signals. AE signals carry information about the details of the physical processes that are responsible for such signals. Analysis of acoustic emission signals have been traditionally used for nondestructive testing and monitoring structures during qualification tests. A number of studies in the past have analyzed AE signals to understand the individual processes involved in damage growth in materials such as crack growth. Machinery condition monitoring using AE technique has received significant attention in the recent past. In such studies, AE signals have been used to recognize the extent of degradation of the contact surfaces, such as those in bearings and gears.

AE signals are generated during sliding motion in bearings, gears, and turbine blade root joints as well as bolted and riveted joints. Changes in the pattern of AE signals have been used in the past to indicate surface damage. These surfaces, while smooth on a macroscopic scale, have roughness or asperities whose dimensions may be of the order of microns. During the relative motion between two surfaces in contact, the asperities on one surface attempt to slide past the asperities on the opposite surface, which results in the collision between these asperities and sudden loading and unloading of regions in their immediate vicinity. The interactions between pairs of asperities may last a very short duration, of the order of few microseconds. The transient forces accompanying such interactions between asperities are a prolific source of elastic waves that are sensed as acoustic emission signals. Further, such relative displacement between surfaces can also lead to plastic deformation and fracture of asperities and accumulation of wear particles

between surfaces, each of which can also generate acoustic emission signals. Baranov [1] summarizes the sources of AE during friction conventionally into three groups: impact of friction surface at microscopic level (asperity collision), surface damage, formation and rupture of adhesion junctions.

Repetitive relative motion of the surfaces over longer periods leads to change in the roughness and texture of the surface, and it can be expected that acoustic emission signals may be indicative of these changes. The first group of papers reviewed here examines the relationship between the acoustic emission signal characteristics and the conditions prevailing at the contacting surfaces. Dornfeld [2] performed early studies to understand the relationship between the AE signals and sliding friction. Jibiki et al [3] studied AE signals generated by friction over a small contact area between two cylinders arranged such that their axes were 90 degree apart. The friction noise for repetitive cycles of sliding at “point” contact of the cylinders was recorded using a microphone. The main frequency component of the detected acoustical signal was a little over 1 kHz. The amplitude of the AE signal was found to increase as the fretting stroke or the frequency was increased. Further, the amplitude of the AE signal was also found to increase with the level of surface wear. Ferrer et al [4] studied the acoustic emission waves generated during transition from static to dynamic friction. Resonant frequency AE sensors were used in these experiments to record the signals. They experimentally simulated stick-slip conditions between a pair of pads and a flat plate during a single stroke and recorded the resulting acoustic emission signals. The different segments of the recorded waveforms were related to different segments of the slip process including micro-slip, partial slip and gross slip. Abdelounis et al [5] examined noise generated by friction between two flat surfaces using microphones. As the surface roughness was increased, the amplitude of the acoustical signal was found to increase as a logarithmic function of the surface roughness. The relationship between AE signal characteristics and friction and wear was also studied by Hase [6] and Hisakado [7]. Parameters of the signals such as count, count rate, amplitude were considered in the analyses.

Theoretical models of acoustic emission signal generation due to friction are also available. Fan et al [8] analyzed the relationship between AE energy and the surface characteristics, contact load, and sliding velocity. Baranov et al [9] determined the AE activity levels in terms of acoustic emission counts, count rate, energy corresponding to different conditions that exist at the contact surfaces. Alam et al [10] numerically simulated the AE signal generation and propagation in a flat plate. Detailed characteristics of AE signals corresponding to different conditions prevailing at the contact surface were determined.

The second group of papers is on the use of acoustic emission for diagnosis of the condition of machinery, specifically surface degradation in bearings and gear trains. Li [11] used pattern classification to monitor defects in bearings using AE signals. Al-Dossary [12] investigated the variation in RMS voltage of AE bursts to quantify implanted defects in roller bearings. Measurement and analysis of AE signals were used in condition monitoring of gears [13-14]. Experiments based on back-to-back gearbox setup were used to monitor changes in AE RMS voltage and energy.

Jayakumar [15] provided a review of application of AE technique for online monitoring of a variety of manufacturing processes. It was found that acoustic emissions generated during different forming processes provide useful information for detecting die wear and cracking, friction properties, state of lubrication, and others. Meriaux [16] studied crack propagation mechanisms in fretting fatigue using acoustic emissions. In addition, AE signals resulting from sliding motion, friction and wear in different mechanical elements were studied. [17–21]

The above studies specifically considered acoustic emission signals due to relative motion between surfaces in contact. In addition, some findings from other studies, which directly look at the relationship between the surface features and coefficient of friction, are also relevant for interpreting acoustic emission signals. Menezes [22] examined the effect of surface texture and wear on the coefficient of friction. The coefficient of friction was found to be independent of the value of roughness but showed significant dependence on texture. Philippon [23] studied the coefficient of friction at high sliding velocities, typical of a projectile sliding against a surface. Other studies dealt with the friction-velocity relationship [24], modeling of multi-asperity contacts [25-26], and fretting fatigue analysis [27-28]. The analysis of the frictional processes operating at various length scales, ranging from nanometers to macro scale, has been studied using a variety of tools [29-31]. Preliminary results from the current study [32] provided an understanding of friction related AE signals.

In the present paper, sliding motion between two dry flat steel surfaces in contact is examined. AE signals generated by the friction between the two surfaces are measured and analyzed. The objective of this work is to examine if AE signals carry recognizable features that can reveal the conditions prevailing at the interface where frictional sliding is taking place. The conditions include surface roughness, normal pressure as well as the duration and velocity of sliding. AE signals were acquired for eight different combinations of these parameters. Features of acoustic emission waveforms due to sliding motion such as amplitude, frequency, and duration for different combinations of test conditions are examined. These results are likely to be of relevance for AE based machinery diagnostics and structural health monitoring. Details of the work are presented in the following sections.

7.2 Experimental test setup

7.2.1 Test fixture

Figure 1 shows the test fixture designed for studying acoustic emission signals generated due to friction. This fixture is capable of simulating friction between surfaces under controlled conditions including normal pressure and sliding velocity. The fixture consisted of two identical friction pads pressed against the opposite surfaces of a long steel bar near its midpoint. The relative motion between the friction pads and the steel bar could be controlled from about five microns to several millimeters. The fixture is mounted on 810 Material Test System (MTS) machine and the friction pads could be subjected to either unidirectional or oscillatory motion with respect to the steel bar, as shown in figure 2. The results reported in this paper were obtained while the pads were subjected to sinusoidal motion relative to the steel bar.

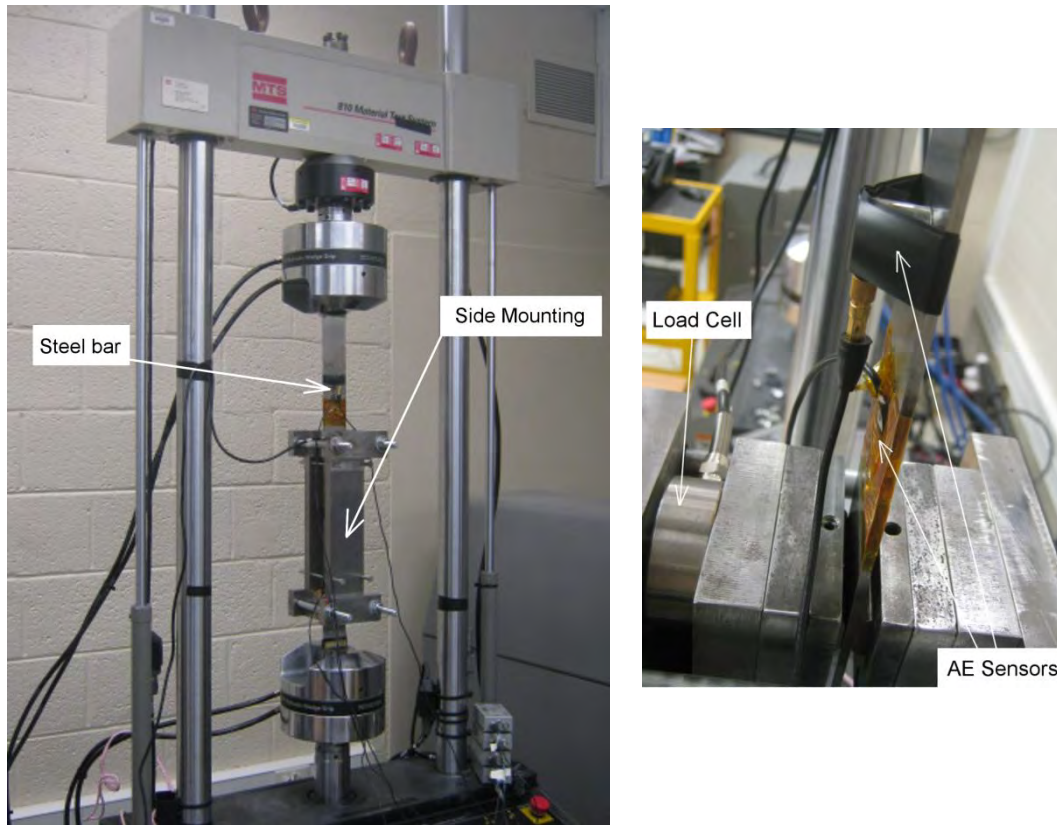


Fig. 1. Friction test fixture

Cyclic loading resulted in repeated stick-slip motion between the pads and the bar. The bar's dimensions were 530 mm X 50 mm X 3 mm, as shown in figure 3, and it was cut from precision ground A2 tool steel bar with surface roughness, R_{ab} , of $0.48\ \mu\text{m}$ and R_{zb} of $2.76\ \mu\text{m}$. Pairs of friction pads with two different surface roughness values were used in this study. The surface roughness, R_{ap} , of the first and second pairs were respectively $0.15\ \mu\text{m}$ and $1.54\ \mu\text{m}$. These surface roughness measurements were taken parallel to the direction of relative sliding between the pads and the bar. The steel friction pads were 50 mm long and their contact surfaces were flat with round corners, as shown in figure 4. The Rockwell hardness values for the pads and the steel bar were respectively HRB 123 and HRB 96.

The bar was instrumented with wide band and resonant frequency acoustic emission sensors placed on either side of the friction region. The side mountings which held the friction pads were designed to be stiff compared to the steel bar participating in the friction process. The contact pressure between the pads and the bar was monitored using a load cell. The readings of the load cell during the cyclic motion were monitored on an oscilloscope.

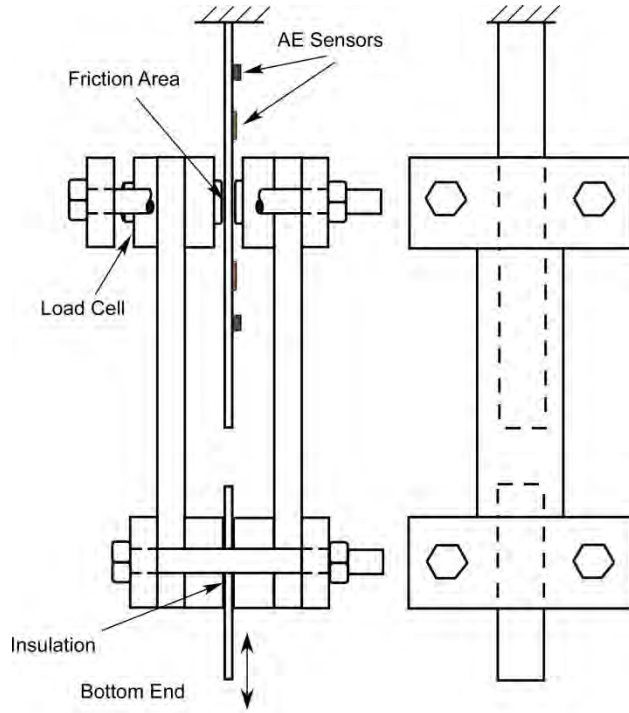


Fig. 2. Schematic representation of the test fixture

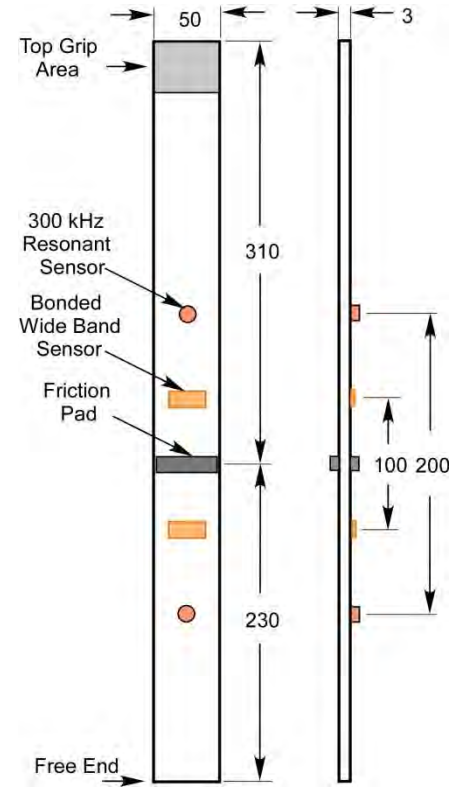


Fig. 3. Steel Bar Dimensions

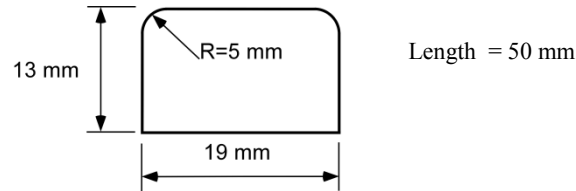


Fig. 4. Dimensions of friction pads

7.2.2 AE instrumentation

Four AE transducers were used to detect the friction related acoustic emission signals. The first set of transducers were Physical Acoustics Corporation R30 sensors with a resonant frequency of 300 kHz. The second set of transducers were rectangular piezoelectric wafers bonded to the surface of the steel bar as shown in figure 3. These sensors were shown to have wide band characteristics [33] and could detect signals up to a frequency of 700 kHz. The performance of the sensors was verified using pencil lead break tests before each data acquisition. The two types of sensors had comparable sensitivities, but their frequency responses were widely different. Sensor locations are shown in figure 3. AE source location capability with sensors positioned on opposite sides of the friction region helped in isolating signals of interest in the present study. The results included in this paper were obtained using the bonded piezoelectric wafer sensors. Most of the

data acquisition was performed using Physical Acoustics Corporation preamplifiers with 40 dB gain and PIC-2 data acquisition system. The frequency response of this instrumentation was calibrated in the laboratory to interpret the AE waveforms that will be presented in the following sections. The gain for the PAC preamplifiers was highest and flat between 200 kHz and 400 kHz. The gain at 100 kHz was found to be 37% of the gain at 200 kHz. At frequencies of 500, 600 and 700 kHz, the gain for the preamplifiers was respectively 60, 33, and 21% of the gain at 200 kHz. Physical Acoustics Corporation PIC-2 data acquisition system was used to acquire the complete waveforms at a rate of 5×10^6 samples/second. These waveforms were further processed on a personal computer. A 35 dB threshold was set for acquiring AE signals.

7.2.3 Test procedure

The results included in this paper correspond to sinusoidal motion of the friction pads while the steel bar was held stationary by gripping at its top end. The steel bar was free at the bottom end. Acoustic emission signals corresponding to different combinations of parameters such as surface roughness, normal pressure, stroke length, and velocity were recorded and examined. The range of variations in these parameters governing the friction condition is listed in table 1. Table 2 lists the eight different combinations of friction parameters for which acoustic emission data were acquired. The first four tests with prefixes RS, involved the steel bar with relatively rough surface ($R_{ab} = 0.48 \mu\text{m}$) and friction pad with relatively smooth surface ($R_{ap} = 0.15 \mu\text{m}$). The last four tests with prefixes RR involved the same steel bar with relatively rough surface and friction pads of comparable roughness ($R_{ap} = 1.54 \mu\text{m}$). These four tests had the same pattern of normal pressure, stroke length applied at the lower grip, and cyclic frequency as the first four tests. The axial load generated in the bar depended on the contact pressure, surface roughness, axial displacement, and the stick-slip conditions prevailing at the frictional interface. The axial load was measured by the MTS load cell. The relative displacements of the lower grip as well as the frictional force transferred through the friction pads during the reciprocating motion were recorded by the acoustic emission data acquisition system.

Two sets of experiments, termed Set A and Set B, were performed separately to measure different parameters of interest. The contact surfaces used in these two sets had nominally identical roughness values. Tests on Set A were performed to check if measurable surface degradation was taking place during the tests RST1 to RST4 listed in Table 2. Surface roughness values at the initial condition as well after 1000, 1300, 1600, 1900, and 2200 cycles were measured. Both R_a and R_z values were measured for the pair of pads and the bar at 40 different spots distributed over the contact area. These results, presented in the next section, indicate that the surface roughness values remained essentially unchanged during these experiments. Further since the hardness of the bar was significantly lower than the friction pads (HRB 96 for the bar versus HRB 123 for friction pads), if measurable wear occurred during these experiments, the bar surface would have been the first to indicate such changes. Hence at the end of eight segments of cyclic loading used in Set B, the final roughness values of the steel bar, were measured at 40 locations and was found to be substantially same as that of its initial value.

Individual tests corresponding to each of the eight combinations of parameters listed in Table 2 lasted only 300 cycles of reciprocating motion to ensure that the surface roughness remained nearly constant during these tests. The pair of surfaces comprising of the bar ($R_{ab} = 0.48 \mu\text{m}$) and smooth pad ($R_{ap} = 0.15 \mu\text{m}$) were subjected to 1000 cycles for initial test setup and four segments of 300 cycles each for the four tests RST1 to RST4. Similarly the pair of surfaces comprising of the bar ($R_{ab} = 0.48 \mu\text{m}$) and rough pad ($R_{ap} = 1.54 \mu\text{m}$) were subjected 1000 cycles for initial test setup and four segments of 300 cycles each for the four tests RRT1 to RRT4. Further, these surfaces were also cleaned before the fixture was reassembled for the next segment of the test.

Table 1. Parameters for which AE signals were generated

Friction Parameter	Value 1	Value 2
Contact pressure, P, MPa	2	4
Loading frequency, F, Hz	0.5	1
Axial grip disp. amplitude, A, mm	0.25	0.5
Bar surface roughness, R_{ab} , μm	0.48	---
Friction pad roughness, R_{ap} , μm	0.15	1.54

Table 2. Combinations of parameters for which AE signals were generated

Test	Roughness, R_{ap}, μm	Pressure, P, MPa	Frequency, F, Hz	Amplitude, A, mm
RST1	0.15	2	0.5	0.25
RST2	0.15	2	1	0.5
RST3	0.15	4	0.5	0.25
RST4	0.15	4	1	0.5
RRT1	1.54	2	0.5	0.25
RRT2	1.54	2	1	0.5
RRT3	1.54	4	0.5	0.25
RRT4	1.54	4	1	0.5

7.3 Results and discussion

7.3.1 Surface roughness of contact surfaces

The results from cyclic loading of surfaces in set A are shown in Figure 5. The surface roughness values R_a and R_z were measured for the friction pads corresponding to the conditions in tests RST1 to RST4, each lasting 300 cycles, and their variation is plotted in Figure 5 (a) and (b). The percentage variation in the values of R_a and R_z over the 1200 cycles, respectively were 5.8 % and 5.4 %, suggesting that the surface conditions remained nearly constant. This level of variability was seen between different regions of the same surface.

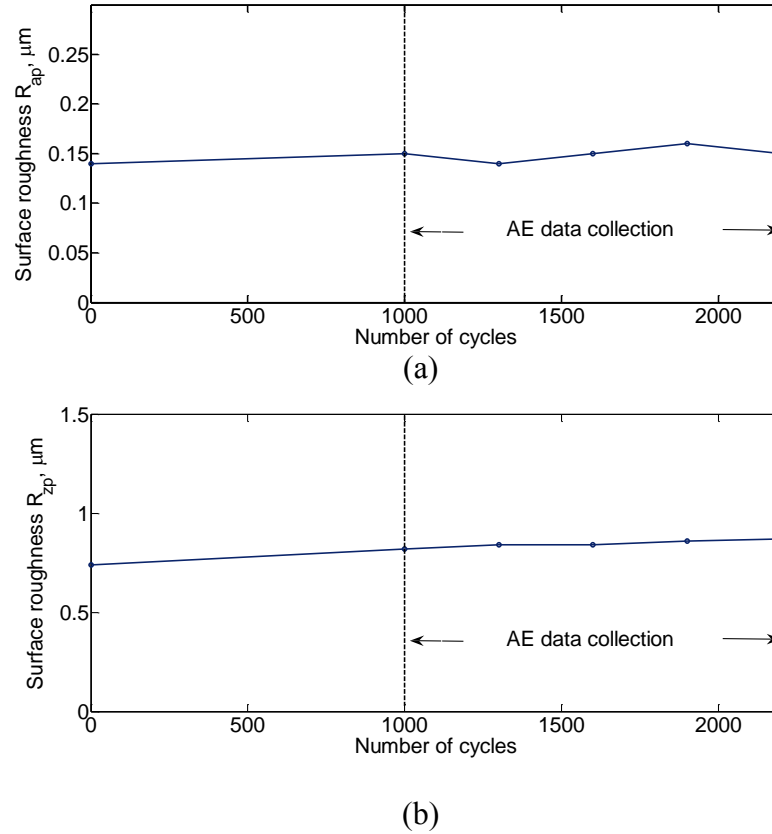


Fig. 5. Surface roughness measurements (a) R_a and (b) R_z

7.3.2 Stick-slip and acoustic emission events

Figure 6 shows the variation of bottom grip displacement as well as the load transferred through the frictional interfaces for different test conditions. While the bottom grip was undergoing sinusoidal displacement, the load transferred across the frictional interface, as measured by the MTS load cell, was deviating significantly from the sinusoidal shape, indicating slip at the frictional interfaces. In these figures, downward displacements are considered positive. In figure 6(a), as the bottom grip moves from point A to point B, there is a proportional increase in axial load induced in the bar, indicating that the steel bar's surface that is in contact with the friction pad was experiencing essentially the same displacement as the pad – stick phenomenon. However, at point B, the proportionality between the displacement and the load ceases. In the segment B to C, the axial load induced in the steel bar essentially remains constant while the displacement keeps increasing – this is the slip phenomenon. As the grip reverses direction at point C and moves towards point D, the load starts following the displacement in a proportional manner – this is the stick phenomenon. At point D, there is slip between the plate and the friction pad in the reverse direction. This stick-slip phenomenon repeated itself without recognizable variation throughout the nearly 300 cycles applied at this load. Stick-slip phenomenon for other combinations of surface roughness and normal pressure are shown in figures 6 (b) to (d). A comparison of figures 6(a) and (b) or (c) and (d) indicates that the surface roughness of the friction pad ($R_{ap} = 1.54 \mu m$ vs. $R_{ap} = 0.15 \mu m$) has a small influence on the load level at which gross slip begins.

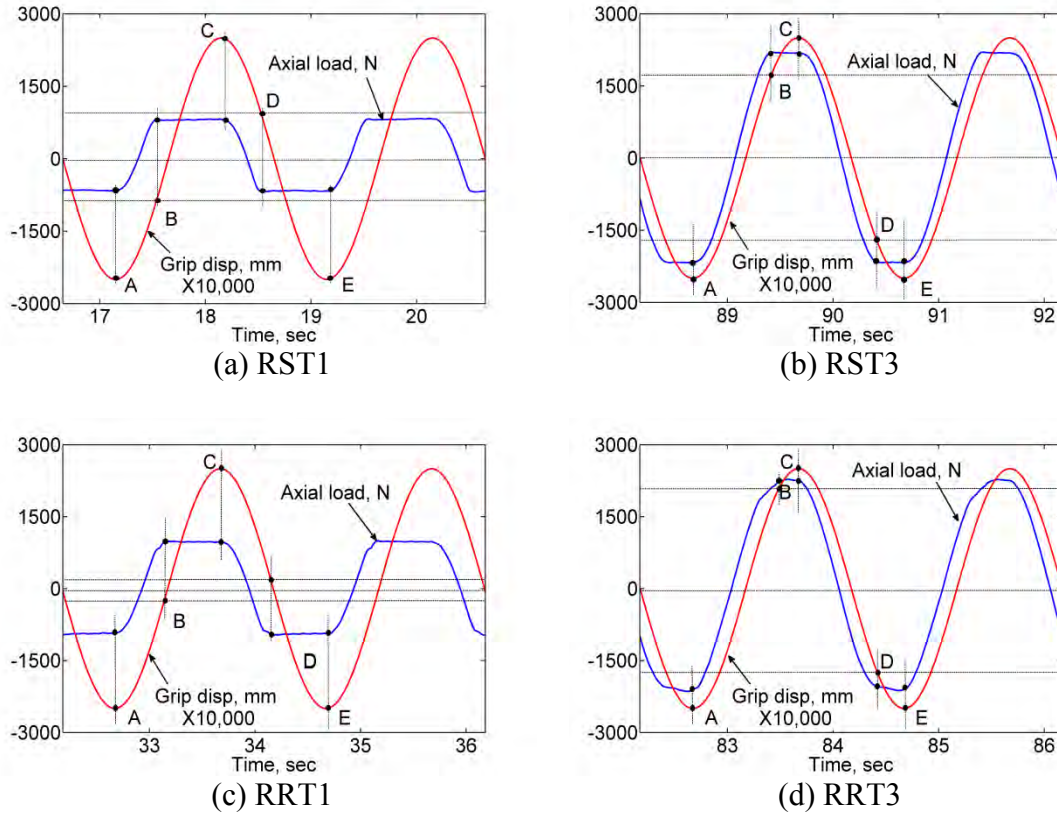


Fig. 6. Relationship between the lower grip displacement and the axial load in the steel bar indicating the repetitive stick and slip intervals during cyclic loading of four different tests

The displacement of the friction pads appeared to follow the same sinusoidal shape of the bottom grip. However, the magnitude of displacement was much smaller because during the “stick” period, the bar was extending and contracting due to the applied load. Based on the maximum load generated on the steel bar and corresponding displacement of the steel bar’s surface that is in contact with the friction pads, the amplitude of displacement of the friction pads for each of the cases RST1 and RRT1 shown in figure 6 is estimated to be about $27 \mu\text{m}$. The estimated distance of slip for the cases of RST1 and RRT1 is about $18 \mu\text{m}$; for the cases of RST3 and RRT3 is about $4 \mu\text{m}$.

Figure 7 shows the plot of the time of occurrence of AE events during the stick-slip cycles for the case of RRT2 ($F = 1 \text{ Hz}$, $R_{ap} = 1.54 \mu\text{m}$, $A = 0.5 \text{ mm}$, $P = 2 \text{ MPa}$). Red circles on the load curve indicate the instants at which AE events were recorded. AE events occurred predominantly during the slip portions. No significant variation of the AE pattern was seen over the nearly 100 cycles, corresponding to the duration of the test.

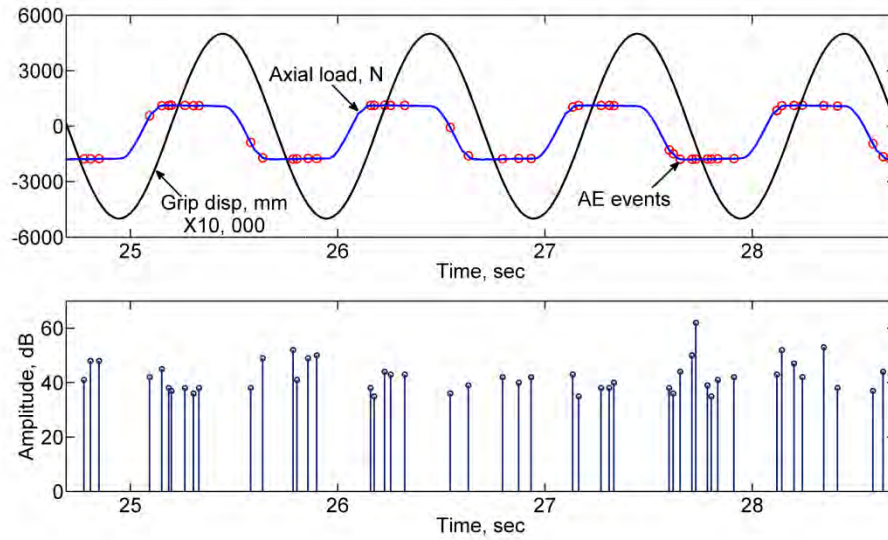


Fig. 7. The time of occurrence and amplitudes of AE events for RRT2

During each of the slip segments of the cyclic motion, such as BC in figure 6(a), whose duration is one second, a large number of acoustic emission events are likely to be generated because of the numerous collisions of asperities present on the friction pads with those on the steel bar. However, in these tests, on average about 5 acoustic emission events of varying amplitudes and durations were recorded per half cycle. It is likely that among many AE events generated during this period, only a few that exceeded the threshold value were recorded. In addition, for the events recorded, there might be a superposition of a number of acoustic emission signals corresponding to numerous individual collisions occurring either simultaneously or in short succession within a few tens of microseconds of each other.

7.3.3 Waveforms corresponding to lead-break

Acoustic emission waveforms are determined by the characteristics of the source event, the geometry of the medium through which the stress waves travel before reaching the sensor, and the frequency response of the sensor and instrumentation. Acoustic emission waveforms are a complex superposition of signals with a range of frequencies. The individual frequency components are not readily recognizable from the waveforms. However, the wavelet diagrams indicate the presence of different frequency components as well as their arrival times. Even though all the frequency components are generated at the same time at the source, they travel with different velocities and hence arrive at different times at the sensor.

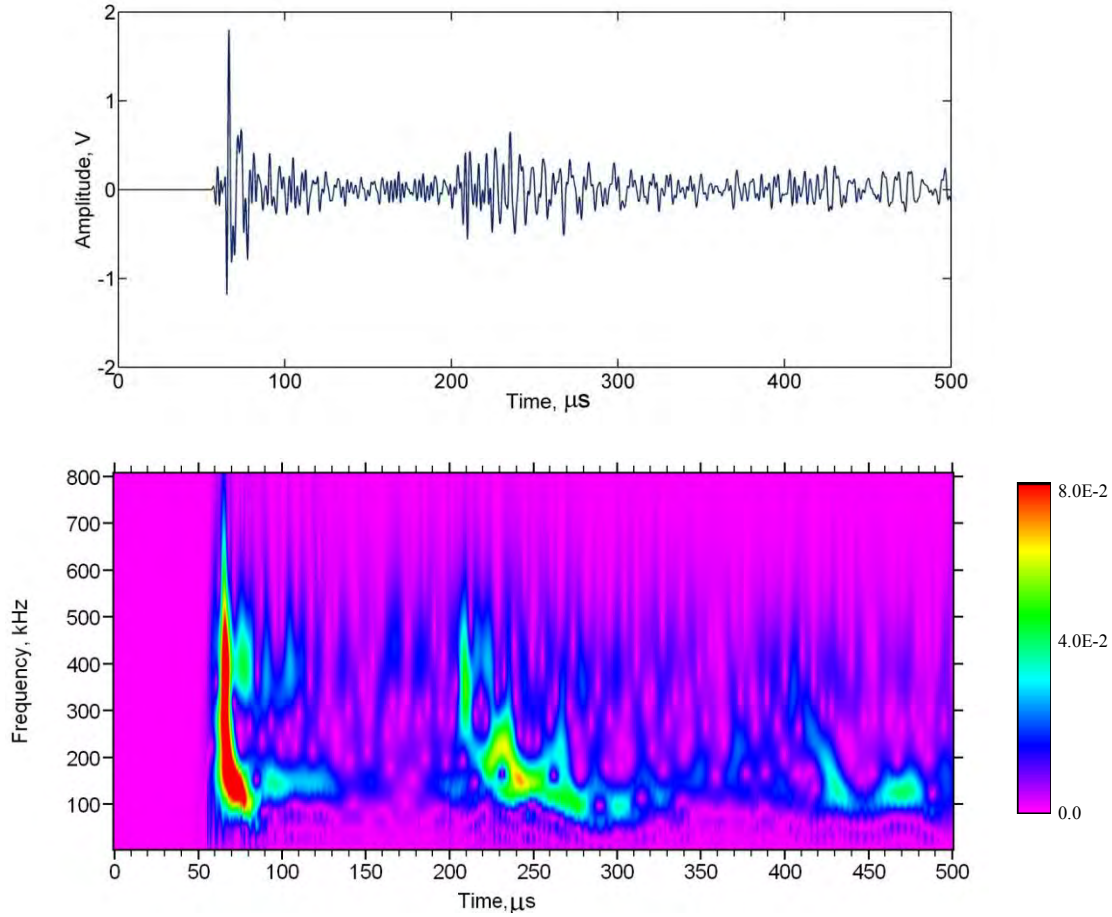


Fig. 8. AE waveform and wavelet diagram for Lead break event

In order to have a baseline for interpreting the friction related waveforms, the signal characteristics corresponding to a lead break test are first presented in figure 8. This comparison is helpful in isolating the features related to the source events. Here both the waveform and the wavelet diagram are included. AGU Vallen wavelet software is used to obtain the wavelet diagrams [34]. A lead-break test is commonly used to verify the acoustic emission test setup and is assumed to simulate discrete events such as an incremental crack growth. A 2 mm long 0.5 mm diameter HB pencil lead was broken at the center of the steel bar's friction area to generate the waveform. These waveforms had peak amplitude of nearly 2 volts and started with large initial amplitude, after which there was a rapid drop in amplitude. There is a second segment after about 110 μ s, due to the reflections from the ends of the bar. In particular, there is a period of very little signal amplitude between the initial signal and the reflections. The different frequency components of the signal and their arrival times are clearly seen in the wavelet diagram.

7.3.4 Friction related waveforms

Nearly 70% of the AE events recorded during these tests originated from the region of frictional contact between the friction pads and the steel bar. Signals originating from other locations were excluded from this analysis based on source location. Figure 9 shows a typical waveform corresponding to friction related AE event obtained during the slip phase of test RST4 ($R_{ap} = 0.15 \mu\text{m}$, $P = 4 \text{ MPa}$, $A = 0.5 \text{ mm}$, $F = 1 \text{ Hz}$). Most waveforms are characterized by large amplitude at the start of the waveform followed by gradually decreasing amplitude, which extended to a little over $500 \mu\text{s}$. Further, as in lead-break tests, the arrival of the reflections from the ends of the bar could also be observed. A major difference is that the quiet period between the initial pulse and reflections in lead-break events was not present in the friction events.

The peak amplitudes of individual friction related AE events rarely exceeded a level of 50 dB for the frequency band above the 100 kHz used in these tests. The amplitudes of friction related events corresponding to RRT2 are shown in figure 7. Friction related events under other conditions reported in this paper were also having similar amplitude distributions. The relatively low amplitudes seen in these experiments can be attributed to the modest normal pressures used in these experiments, chosen mainly to avoid surface damage during these experiments and the deliberate choice of frequency band above 100 kHz to avoid ambient noise.

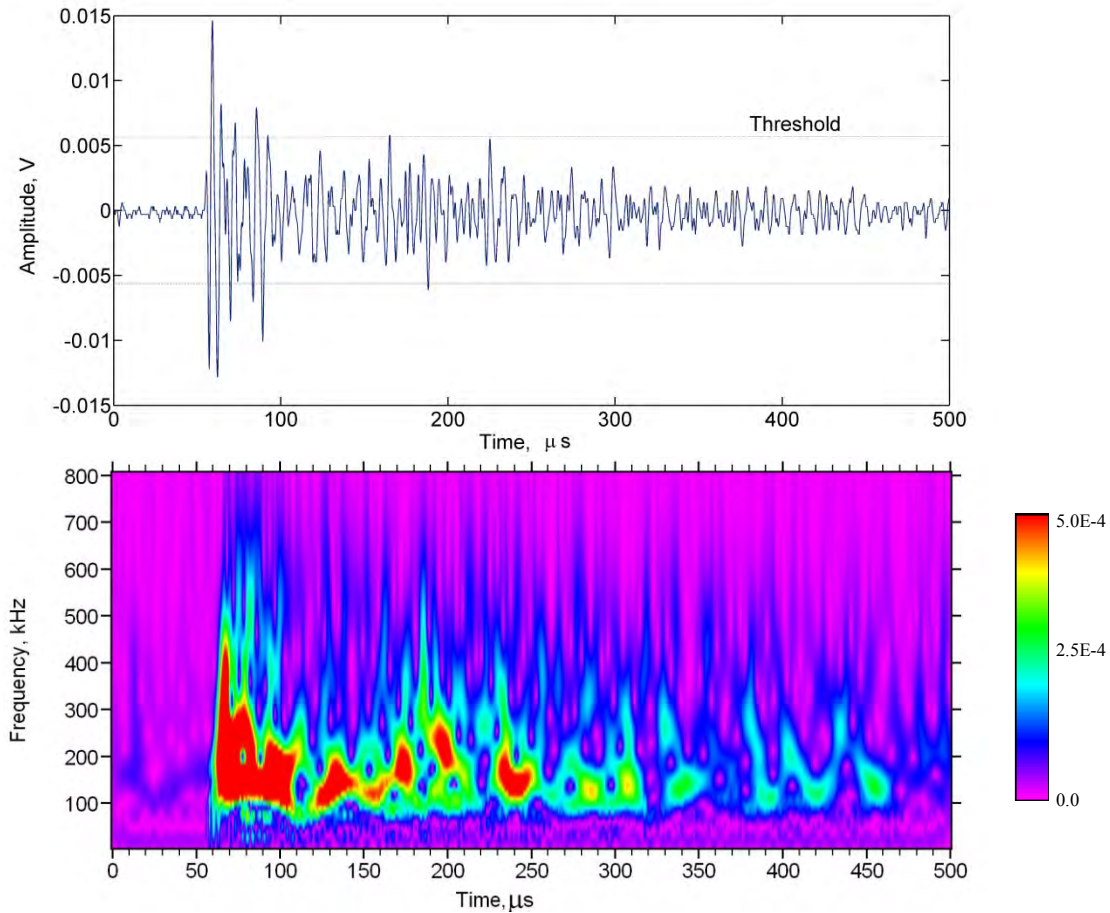


Fig. 9. AE waveform and wavelet diagram for friction related event from test RST4

7.3.5 Crack related waveforms

In sections 3.2 and 3.3, waveforms from lead-break and friction related acoustic emission events were described. For comparison, figure 10 shows a waveform and its wavelet diagram obtained from incremental crack growth in a steel bar of the same geometry as the one used in the friction tests and instrumented with the same type of sensors. The steel bar used is 75 mm longer than the one used for the friction experiment.

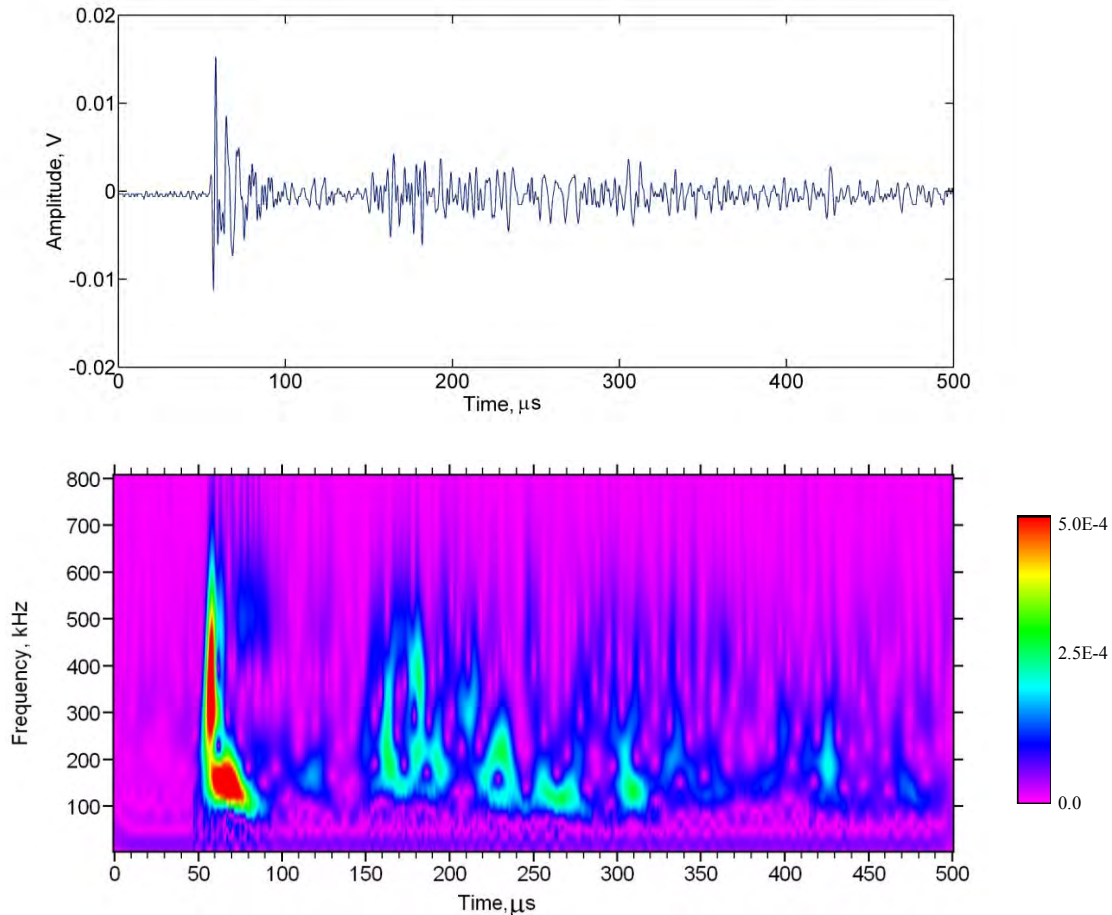


Fig. 10. AE waveform and wavelet diagram for crack growth event

Crack related events were, in some respects, similar to that of lead-break waveforms. These waveforms are characterized by a strong initial component followed by a relatively quiet period after which reflected signals are seen. This, however, is in contrast to friction related signals for which there is sustained signal amplitude between the initial segment and the segment due to reflections. Comparison of the wavelet diagrams corresponding to the lead break test and the crack growth tests with the wavelet diagram due to the friction related signal is useful in understanding the source mechanisms in these three cases. The first two types of events are generated by a single impulse and the resulting initial segment is well separated from the segment corresponding to reflections from the specimen ends, as seen clearly in the waveforms as well as wavelet diagrams. In the case of friction related signals, the sustained activity between the initial segment and the reflected segment is indicative of multiple impulses occurring within microseconds of each other.

Such a process of simultaneous or sequential interaction of asperities belonging to the contact surfaces has been postulated in the literature [1, 8-10].

7.4 Characterization of the friction related acoustic emission waveforms

Recent studies have revealed that acoustic emission technique can be useful tool to monitor surface damage in bearings and gears. In the following section, we will examine whether the features embedded in the acoustic emission waveform are indicative of differences in the operating conditions at the interface of such surfaces during their relative motion. The study included the acquisition and analysis of AE signals corresponding to different combinations of the parameters listed in Table 1. The effect of the surface roughness of the friction pad, the normal pressure between the contact surfaces, and the sliding velocity on the acoustic emission waveform and its frequency content are examined.

The amplitude distributions of AE events did not have recognizable variations for the different tests performed under this study. Figure 11 shows the amplitude distribution for the cases RST2 and RRT2. However, it should be noted that the normal pressure values used in these experiments were relatively small with limited range of variation. Further, the frequency range that is considered here is above 100 kHz for the most part so as to avoid ambient sources of acoustical signal which dominate in the lower frequencies.

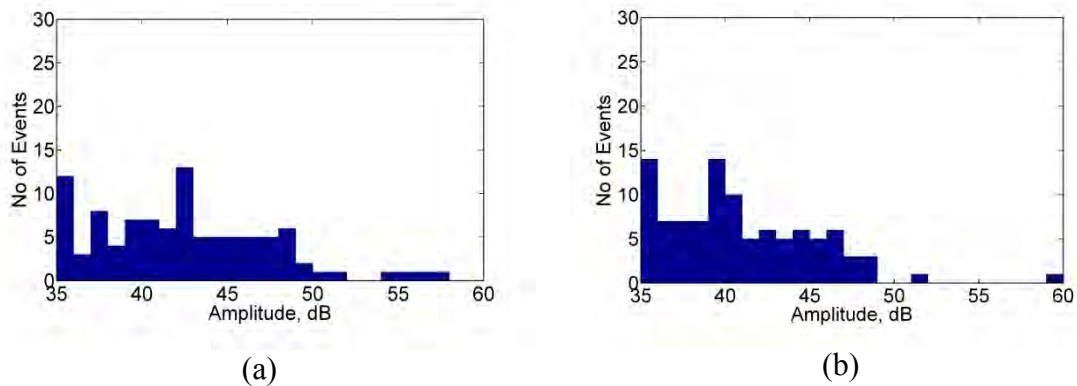


Fig. 11. Comparison of amplitude distribution for different tests (a) RST2 and (b) RRT2

7.4.1 Effect of surface roughness

The features of the AE signals corresponding to variations in the operating conditions such as surface roughness, normal pressure, and sliding velocity that are highlighted in the following sections were identified after examining a collection of waveforms and their wavelet diagrams corresponding to each type of test. To obtain a consistent interpretation, for each test condition, the average pattern seen in 25 randomly selected waveforms was used.

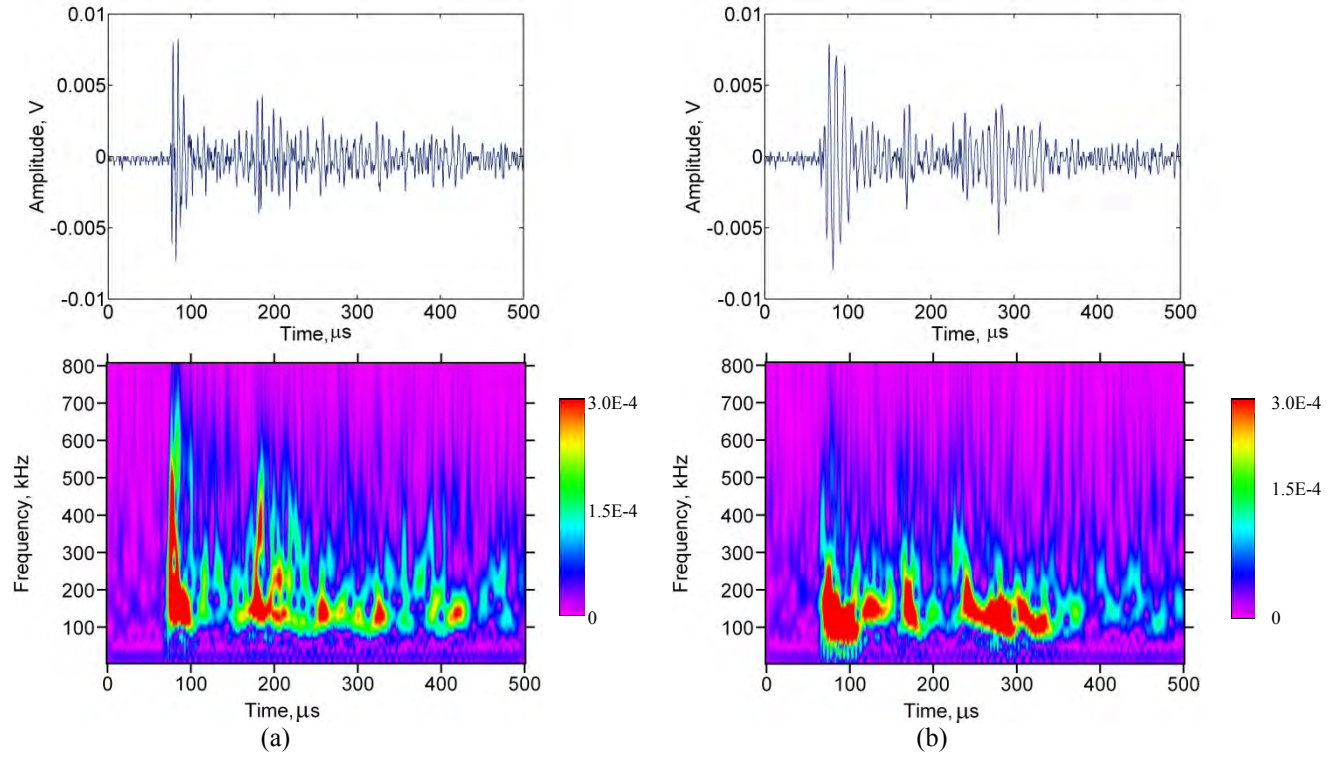


Fig. 12. Effect of surface roughness shown by wavelet diagrams (a) test RST1 (b) test RRT1

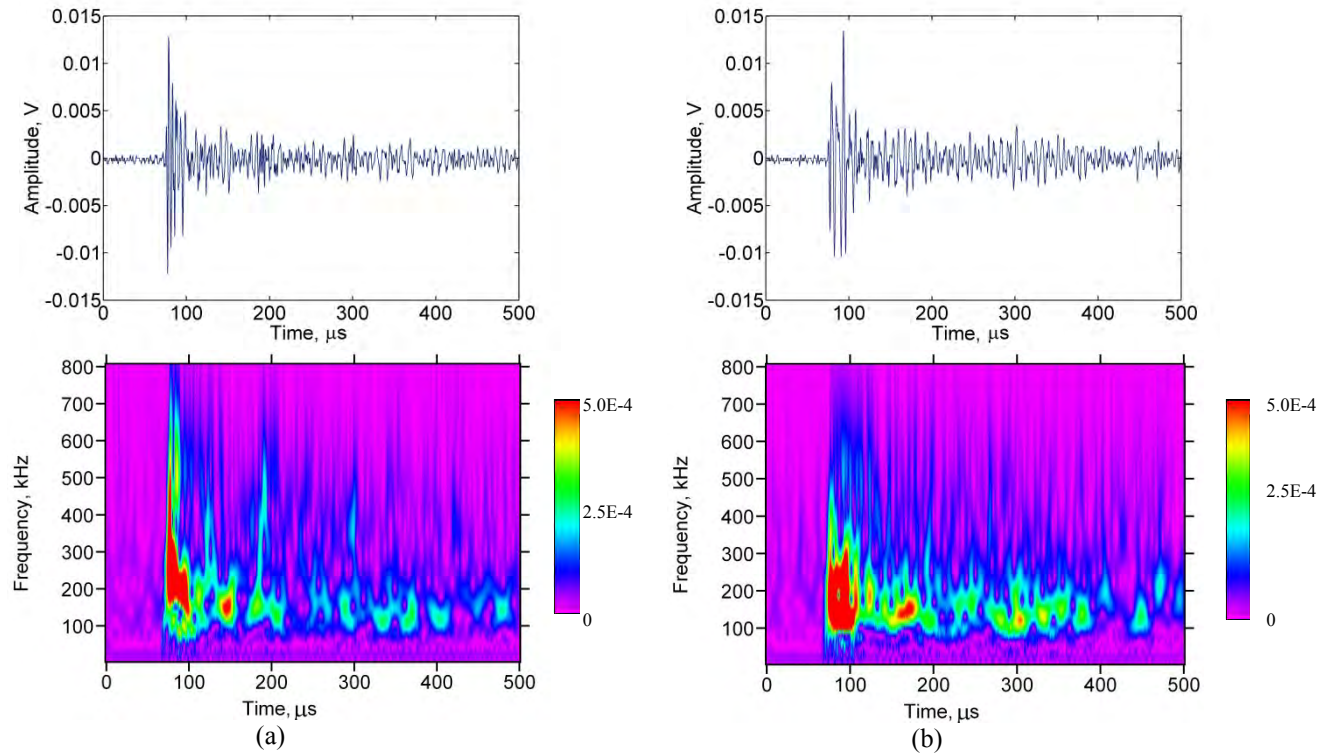


Fig. 13. Effect of surface roughness shown by wavelet diagrams (a) test RST3 (b) test RRT3

The differences between the acoustic emission signals generated in test RST1 ($R_{ap} = 0.15 \mu\text{m}$) and test RRT1 ($R_{ap} = 1.54 \mu\text{m}$) are considered first. The only difference between these two tests was the surface roughness of the friction pads. Twenty-five randomly selected waveforms obtained during each of the two tests were used to examine the frequency-time patterns of the AE signals. To highlight the common features found in these sets, a representative waveform and its wavelet diagram from each test are shown in figure 12. A similar comparison is also between the two tests and the results are shown in figure 13.

The wavelet diagrams corresponding to AE signals from the RS cases included in figure 12 and figure 13 show the presence of components in excess of 500 kHz at the leading edge of the signals whereas the wavelet diagrams corresponding to AE signals from the RR cases had no significant amplitude above this frequency range. It was found that, for tests involving smooth pads, more than 70% the signals had this distinct high frequency component while only 20% of the waveforms for rough pads had such components, irrespective of the amplitude of the signal.

It should also be noted that the sensors used in these experiments were not sensitive to frequencies greater than 700 kHz. Further, as noted earlier, the instrumentation used for these experiments had reduced sensitivity for frequency components outside 200 kHz to 400 kHz band. The presence of frequency components from 600 kHz to 700 kHz for RST1 and RST3 are significant considering that the gain at 600 and 700 kHz were only 33% and 21% of the gain in the frequency band spanning 200 to 400 kHz. These differences in the frequency content seen in the wavelet diagrams were not easily observable in the FFT diagram of these signals. The dependence of the frequency content of the AE signal on the surface roughness was predicted from an earlier numerical simulation of friction process [10].

Another observation from these tests is that RS combination gave rise to larger number of AE signals compared to RR combinations for otherwise similar conditions. The envelopes connecting the peaks of individual oscillations in the AE signal indicate the presence of multiple events and reflections of the waveforms from specimen ends. There were only minor differences in the envelopes of the AE signals obtained within each test. In addition, apart from the differences observed in the frequency content described above, there were no other recognizable differences between the envelopes obtained for the smooth pad versus those for rough pads.

7.4.2 Effect of sliding velocity

The velocity during the relative motion between the mating surfaces in the present study depended on the frequency and amplitude of the reciprocating motion while the other parameters were held constant. For such a comparison, the wavelet diagrams corresponding to the RRT1 case ($F=0.5 \text{ Hz}$, $A = 0.25 \text{ mm}$) is presented with those for the RRT2 case ($F=1 \text{ Hz}$, $A = 0.5 \text{ mm}$). The doubling of the loading frequency and displacement amplitude for RRT2 results in quadrupling of the average sliding velocity from RRT1 to RRT2. Corresponding waveforms and wavelet diagrams are shown in figure 14(a) and (b). These figures show that signals with frequency content in the range of 100 to 300 kHz decrease and those in the range of 400 kHz and above increase as the sliding velocity is increased. A similar influence of the increase in the sliding velocity on the increase in the AE frequency components was observed also between RST1 and RST2. These

tendencies were seen in a majority of the signals collected. However, there were exceptions to these trends in a few of the AE signals. These trends were also predicted in the in finite element simulation of friction related AE signals in the earlier study [10].

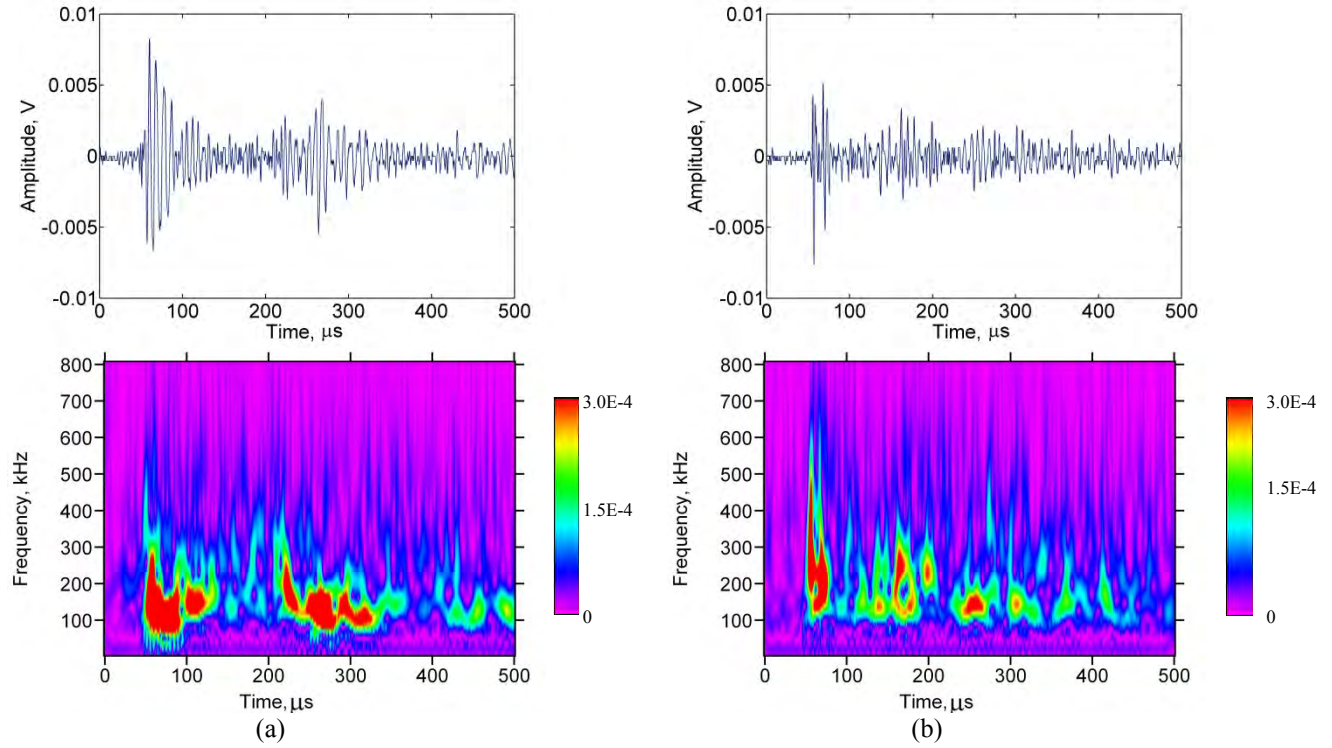


Fig. 14. Effect of sliding velocity shown by wavelet diagrams (a) test RRT1 (b) test RRT2

7.4.3 Effect of normal pressure

The influence of the normal pressure on the AE signal is examined by comparing the results for RRT1 for which the normal pressure was 2 MPa with those of RRT3 for which the normal pressure was 4 MPa. These results are shown in figures 15 (a) and (b). In these cases, the other parameters had identical values. The main difference between the two waveforms was in the intensity of the AE signal between the first arrival and the reflections from the specimen ends. For the case of RRT3, there was significantly greater signal strength before the arrival of the reflection. Increase in the normal pressure also appeared to cause a small increase in the frequency content of the AE signals. At higher normal pressures, greater interference between the asperities in the surfaces in contact is likely to be present. As a result, a greater number of asperities are likely to participate in generating the AE signals.

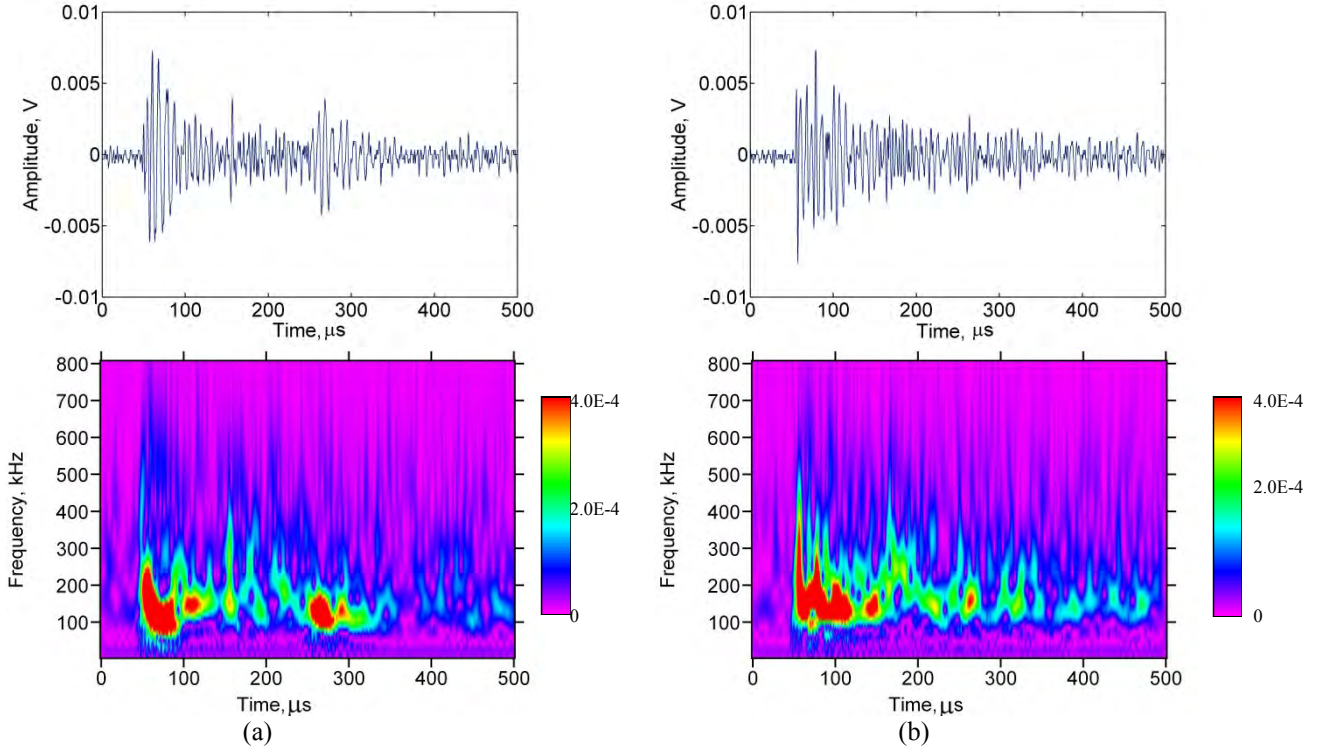


Fig. 15. Effect of normal pressure shown by wavelet diagrams (a) test RRT1 (b) test RRT3

7.5 Friction parameters and AE signal characteristics

By limiting the number of cycles used for each of these tests, surface damage and accumulation of wear particles was kept at a minimum. As mentioned earlier the surfaces were cleaned in between the tests to remove loose particles. Hence, the majority of AE events from these tests are attributed to interaction of asperities. Acoustic emission instrumentation used in these experiments used a frequency range of 100 kHz to 700 kHz. This frequency range was selected to avoid saturation of the amplifier by lower frequency components and to minimize signals from ambient noise. In these tests, variations of the tribological parameters such as surface roughness, sliding velocity, and normal pressure were only very modest. The results presented in this section show that even for these modest changes in the friction conditions, clearly recognizable differences in the features of the AE waveforms were present. In addition, the friction related acoustic emission signals were distinguishable from signals from other sources such as crack growth.

Summary and conclusion

In this paper we explore if the parameters controlling the interaction of two contacting surfaces during the friction process are recognizable in the acoustic emission waveforms and if those features could be clearly identified. A test fixture to simulate the reciprocating motion between two flat surfaces in contact was developed. In this fixture, the parameters such as normal pressure, surface roughness, sliding velocity could be closely controlled. Acoustic emission signals

generated by the friction process for different combinations of surface roughness, normal pressure, and the velocity of sliding were evaluated. Friction related waveforms, in general, depicted patterns that were consistent with multiple asperity interactions during slip. The basic features of friction related AE signals were distinct from those of other AE sources. Clear and systematic changes in the signal characteristics that could be related to the parameters operating at the frictional interface were found. Acoustic emission frequency components well in excess of 700 kHz were generated by the friction process. Frequency component of the signals was found to increase as the roughness of one of the surfaces was decreased. In addition, the frequency content was also found to increase with the increase in sliding velocity. AE signal duration appears to increase with an increase in normal pressure. AE behavior of the friction process observed during these experiments was mostly in agreement with the earlier numerical predictions [10]. The results obtained in this research indicate that acoustic emission technique can be a sensitive tool for monitoring the condition of surfaces.

References

- [1] V. Baranov, E. Kudryavtsev, G. Sarychev, V. Schavelin, Acoustic emission in friction , Elsevier Science, Great Britain, 2007.
- [2] D. Dornfeld, C. Handy, Slip detection using acoustic emission signal analysis, IEEE Proc. Int. Confer. Robotics and Automation 4 (1987) 1868-1875.
- [3] T. Jibiki, M. Shima, H. Akita, M. Tamura, A basic study of friction noise caused by fretting, Wear 251 (2001) 1492-1503.
- [4] C. Ferrer, F. Salas, Discrete acoustic emission waves during stick–slip friction between steel samples, Tribology International 43 (2010) 1-6.
- [5] H. Abdelounis, A. L. Bot, J. Perret-Liaudet, H. Zahouani, An experimental study on roughness noise of dry rough flat surfaces, Wear 268 (2010) 335-354.
- [6] A. Hase, M. Wada, H. Mishina, The relationship between acoustic emissions and wear particles for repeated dry rubbing, Wear 265 (2008) 831-839.
- [7] T. Hisakado, T. Warashina, Relationship between friction and wear properties and acoustic emission characteristics: iron pin on hardened bearing steel disk, Wear 216 (1998) 1-7.
- [8] Y. Fan, F. Gu, A. Ball, Modeling acoustic emissions generated by sliding friction, Wear 268 (2010) 811-815.
- [9] V. Baranov, E. Kudryavtsev, G. Sarychev, Modeling of the parameters of acoustic emission under sliding friction of solids, Wear 202 (1997) 125-133.
- [10] Md. T. Alam, M. Sundaresan, Characterization of fretting related acoustic emission signals, Proceedings of the SPIE 7650, San Diego, 2010.
- [11] C. James Li, S. Y. Li, Acoustic emission analysis for bearing condition monitoring, Wear 185 (1995) 67-74.
- [12] S. Al-Dossary, R. I. R. Hamzah, D. Mba, Observations of changes in acoustic emission waveform for varying seeded defect sizes in a rolling element bearing, Applied Acoustics 70 (2009) 58-81.
- [13] K. R. Al-Balushi, B. Samanta, Gear fault diagnosis using energy-based features of acoustic emission signals," Proc. Inst. Mech. Eng., Part I: J. Systems and Control Engineering, 216 (2002) 249-263.

- [14] T. Toutountzakis, C. K. Tan, D. Mba, Application of acoustic emission to seeded gear fault detection, *NDT & E International* 38 (2005) 27-36.
- [15] T. Jayakumar, C. K. Mukhopadhyay, S. Venugopal, S. L. Mannan, B. Raj, A review of the application of acoustic emission techniques for monitoring forming and grinding processes, *Journal of Materials Processing Technology* 159 (2005) 48–61.
- [16] J. Meriaux, M. Boinet, S. Fouvry, J. C. Lenain, Identification of fretting fatigue crack propagation mechanisms using acoustic emission, *Tribology International* 43 (2010) 2166-2174.
- [17] T. Skare, P. Thilderkvist, J. E. Stahl, Monitoring of friction processes by the means of acoustic emission measurements – deep drawing of sheet metal, *Journal of Materials Processing Technology* 80 – 81 (1998) 263 – 272.
- [18] J. Sun, R. J. K. Wood, L. Wang, I. Care, H. E. G. Powrie, Wear monitoring of bearing steel using electrostatic and acoustic emission techniques, *Wear* 259 (2005) 1482 – 1489.
- [19] B. Kilundu, X. Chiementin, J. Duez, D. Mba, Cyclostationarity of acoustic emissions for monitoring bearing defects, *Mechanical Systems and Signal Processing* 25 (2011) 2061 – 2072.
- [20] G. Kalogiannakis, J. Quintelier, P. De Baets, J. Degrieck, D. Van Hemelrijck, Identification of wear mechanisms of glass/polyester composites by means of acoustic emission, *Wear* 264 (2008) 235–244.
- [21] J. Miettinen, V. Siekkinen, Case Study Acoustic emission in monitoring sliding contact behavior, *Wear* 181-183 (1995) 897-900
- [22] P. L. Menezes, Kishore, S. V. Kailas, Influence of surface texture and roughness parameters on friction and transfer layer formation during sliding of aluminum pin on steel plate, *Wear* 267 (2009) 1534-1549.
- [23] S. Philippon, G. Sutter, A. Molinari, An experimental study of friction at high sliding velocities, *Wear* 257 (2004) 777-784.
- [24] F. Van de Velde, P. De Baets, The relation between friction force and relative speed during the slip-phase of a stick-slip cycle, *Wear* 219 (1998) 220-226.
- [25] B. Bhushan, Contact mechanics of rough surfaces in tribology: multiple asperity contact, *Tribology letters* 4 (1998) 1-35.
- [26] I. J. Ford, Roughness effect on friction for multi-asperity contact between surfaces, *J. Phys. D-Applied Physics* 26 (1993) 2219-2225.
- [27] A. Hutson, T. Nicholas, R. Goodman, Fretting fatigue of Ti–6Al–4V under flat-on-flat contact, *International Journal of Fatigue* 21 (1999) 663-669.
- [28] A. Hutson, T. Nicholas, R. John, Fretting fatigue crack analysis in Ti–6Al–4V, *International Journal of Fatigue* 27 (2005) 1582-1589.
- [29] B. Bhushan, *Handbook of micro/nano tribology*, Springer, USA, 1999.
- [30] P. J. Blau, *Friction science and technology: from concepts to applications*, CRC Press, 2009
- [31] G. W. Stachowiak, A. W. Batchelor, G. B. Stachowiak, *Experimental methods in tribology*, Elsevier Science, The Netherlands, 2004.
- [32] K. Asamene, W. Williams, M. Sundaresan, Experimental analysis of fretting related acoustic emission signals, *Proceedings of the SPIE* 7981, San Diego, 2011.
- [33] M. Jacques, P. Desai, F. Salih, M. Sundaresan, Evaluation of bonded piezoelectric AE sensor for structural health monitoring, *Proceedings of the SPIE* 6935, San Diego, 2008.
- [34] M. A. Hamstad, An Illustrated overview of the use and value of a wavelet transformation to acoustic emission technology, Oct 2011, www.vallen.de/wavelet/index.htm.

PART 8: MACHINE LEARNING TECHNIQUES FOR STRUCTURAL HEALTH MONITORING

Abstract

We report on work that is part of the development of an agent-based structural health monitoring system. The data used are acoustic emission signals, and we classify these signals according to source mechanisms, those associated with crack growth being particularly significant. The agents are proxies for communication- and computation-intensive techniques and respond to the situation at hand by determining an appropriate constellation of techniques. It is critical that the system have a repertoire of classifiers with different characteristics so that a combination appropriate for the situation at hand can generally be found. We use unsupervised learning for identifying the existence and location of damage but supervised learning for identifying the type and severity of damage. The supervised learning techniques investigated are support vector machines (SVM), naive Bayes classifiers, and feed-forward neural networks (FNN). The unsupervised learning techniques investigated are k-means (with k equal to 4, 5, and 6) and self-organizing maps (SOM, with 4, 5, and 6 output neurons). For each technique except SOM, we tested versions with and without principal component analysis (PCA) to reduce the dimensionality of the data. We found significant differences in the characteristics of these machine learning techniques, with a general trade-off between accuracy and fast classification runtime. This trade-off can be exploited by the agents in finding appropriate combinations of classification techniques. The approach followed here can be generalized for exploring the characteristics of machine-learning techniques for monitoring various kinds of structures.

8.1 Introduction

Threats to the integrity of a structure, such as corrosion and cracking, produce challenges for the safety and operational capability of the structure as well as costs involved in monitoring and maintaining it. Structural health monitoring (SHM) provides real-time data and consequently information on the condition of the monitored structure. The research reported here has been carried out as part of the NASA Center for Aviation Safety (CAS) at North Carolina A&T State University. The structures of interest are aircraft although experiments at the stage reported here are performed on laboratory specimens. SHM is particularly important for aircraft as structural failure can result in massive loss of life. In our approach, agents typically serve as proxies for techniques with intensive communication or computation requirements. Agents negotiate to determine a team of techniques for solving the task at hand, and they communicate a workflow to a workflow engine, which actually carries out the tasks on the data streams provided. The agents provide flexibility and intelligence so that combinations of techniques suitable for the situation at hand may be determined. It is thus important that a variety of classifiers with different characteristics be available. For example, some will be fast but not very accurate while others will be slow but very accurate. The data we use are acoustic signals, and the condition we address is crack growth. As the source of the signals is unobservable, classifying acoustic signals by their source must be based on machine learning. Note that sensing here is passive: there is no energy

input required to generate or sense the signals (although energy is required to store and communicate the data).

In SHM, data is interpreted using parameters that are trained with machine-learning techniques. For our experiments, a correlation coefficient is computed between an observed waveform and seven reference waveforms which are generated from numerical simulations of acoustic emission events. The vector of all seven correlation coefficients characterizes the waveform. Our training set consists of 108 samples from the work reported by Esterline and his colleagues [1]. Our test set consists of 1169 signal waveforms (samples) coming from crack growth experiments in a steel bar.

Worden and his colleagues [2] have formulated seven axioms for SHM that capture general aspects that have emerged in several decades of experience. Of particular interest is their Axiom III, which states that unsupervised learning can be used for identifying the existence and location of damage but identifying the type and severity of damage can only be done with supervised learning. Supervised learning tries to generalize responses based on a training set with the correct responses indicated. Unsupervised learning tries to categorize the inputs based on their similarities. Note that unsupervised learning does not assume that we have already identified categories and, in fact, comes up with categories for classifying data points.

Following Axiom III, our research uses two unsupervised and three supervised learning techniques for different aspects of the SHM problem. The results of machine learning provide a more sophisticated level that will allow us to look at the problem of damage identification. We may then address a multitude of issues and provide diagnoses of the problems. The unsupervised learning techniques are k-means and self-organizing maps (SOM). Supervised learning techniques are support vector machines (SVM), naive Bayes classifiers, and feed-forward neural networks (FNN). For each technique except SOM, we tested a version with principal component analysis (PCA) as a frontend to reduce the dimensionality of the data (usually to three principal components), and we tested another version without PCA. The objective is to explore these techniques and note their characteristics so that various combinations of them may be used appropriately in various circumstances.

The approach followed here can be generalized for exploring the characteristics of machine-learning techniques for monitoring various kinds of structures. One must first determine what signals are appropriate for monitoring the structures, (For example, acoustic signals are appropriate for metallic structures while signals propagated through optical fiber are appropriate for concrete structures.) One then determines the sensor and communication infrastructure. Finally, as per this paper, one determines the characteristics of various supervised and unsupervised learning techniques for monitoring the structures in question (given the signals and infrastructure chosen). Admittedly, the repertoire of techniques explored here is far from complete, but we have included the ones most often encountered in structural health monitoring.

The remainder of this paper is organized as follows. The next section looks into previous work in machine learning for SHM, and Section 3 provides an introduction to SHM. Section 4 presents our approach, Section 5 presents our results, and the last section concludes.

8.2 Previous Work in machine learning for

Most previous work on machine learning for SHM has targeted bridges; we consider mature, representative work in this area and then turn to research that has targeted aircraft, which is our domain. Figueiredo and his colleagues performed an experiment on bridges that used four accelerometer sensors [3]. For each test of state conditions, the features were estimated by using a least squares technique applied to time-series from all four sensors and stored into feature vectors. They used four machine learning techniques in an unsupervised learning mode: 1) auto-associative neural network (AANN), 2) factor analysis (FA), 3) singular value decomposition (SVD), and 4) Mahalanobis squared distance (MSD). First the features from all undamaged states were taken into account. Then those feature vectors were split into training and testing sets. In this case, a fed-forward neural network was used to build-up the AANN-based algorithm to perform mapping and de-mapping. The network had 10 nodes in each of the mapping and de-mapping layers and two nodes in the bottleneck layer. The network was trained using back-propagation. The AANN- and MSD- based algorithms performed better at detecting damage. The SVD- and FA- based algorithms performed better at avoiding false indications of damage.

Tibaduiza and his colleagues [TTM2013], in investigating SHM for aircraft fuselages, made use of multiway principal component analysis (MPCA), discrete wavelet transform (DWT), squared prediction error (SPE) measures and a self-organizing map (SOM) for the classification and detection of damage. Each PCA model contains 66 percent of whole data set from the undamaged structure. The remaining 34 percent plus 80 percent of the damage structure to be classified by the SOM. This approach had an accuracy of 99.88%.

Esterline and his colleagues [1] (also targeting aircraft) ran an experiment with two approaches. Their first approach used as training instances experimental data with eighteen traditional acoustic emission features to train a SVM, while their second approach used six correlation coefficients between basic modes and waveforms from simulation data also to train a SVM. The SVM with the second approach performed as well or better than the SVM using the first approach, suggesting the superiority of a set of correlation coefficients over a substantial set of traditional acoustic emission features for learning to identify the source of acoustic emissions.

8.3 Structural health monitoring

In general, damage is defined as change introduced into a system that will adversely affect its current or future performance [5]. This idea of damage is meaningless without a comparison between two states of the system, one assumed to be the unloaded and undamaged state. For mechanical structures, damage can be defined more narrowly as change to the material and/or geometric properties. SHM provides real-time information on the integrity of the structure. It allows better use of resources than scheduled maintenance, which may take place when there is no need.

In characterizing the state of damage in a system, we can ask whether there is damage, where in the system it is, what kind of damage it is, and how severe it is. Damage prognosis is the

estimation of the remaining useful life of a mechanical structure [6]. Such an estimation may be the output from models that predict behavior.

The field of SHM has matured to the point where several fundamental axioms or general principles have emerged. Worden and his colleagues [2] suggest seven axioms for SHM. The following are the axioms most relevant to this paper.

Axiom III: Identifying the existence and location of damage can be done in an unsupervised learning mode, but identifying the type of damage present and the damage severity can generally only be done in a supervised learning mode.

Axiom IVa: Sensors cannot measure damage. Feature extraction through signal processing and statistical classification is necessary to convert sensor data into damage information.

Axiom IVb: Without intelligent feature extraction, the more sensitive a measurement is to damage, the more sensitive it is to changing operational and environmental conditions.

Axiom V: The length- and time-scales associated with damage initiation and evolution dictates the required properties of the SHM sensing system.

Axiom III is particularly relevant here. Supervised learning together with either analytic models or data from the structure can be used to determine damage type and extent. Statistical methods may also be used.

8.4 Approach

Our overall architecture involves a multiagent system where the agents are typically proxies for computation- or communication-intensive techniques. These techniques are executed on one or more high-performance platforms structured as a workflow engine. Wooldridge defined an agent as an autonomous, problem-solving, computation entity that is capable of effectively processing data and functioning singularly or in a community with in dynamic and open environments [7]. The agents in our system negotiate to determine what techniques in what combinations will be used in a monitoring task, thus determining a workflow that is executed on the workflow engine. The multiagent system is thus the “brains” and the workflow engine the “brawn” of our SHM system. Much of the intelligence here is finding the appropriate techniques for the situation at hand. In one situation, we might want a given task done quickly with only rough accuracy, while in another situation accuracy may be paramount and speed of only secondary importance. Regarding the results of machine learning for SHM, we would like an assortment of classifiers to provide a range of possibilities for the diversity of situations that arises in SHM.

Machine learning is generally facilitated by reducing the dimensionality of the data, and this is certainly the case here. For this, we use PCA [8]. PCA is an algorithm that centers the data by subtracting off the mean then choosing the eigenvector of the data covariance matrix with the largest eigenvalue [8]. It places an axis in that direction, and then incrementally and similarly places the other axes orthogonally to the first in a way maximizing the possible variation. The number of axes is chosen to be fewer than the number of axes (dimensionality) of the original data set. The data is thus reduced in dimensionality while most of the variation is retained.

Recall that the unsupervised learning techniques we investigated are k-means and SOM. The k-means algorithm [8] classifies n observations into k clusters. The value of k is set by the

user. The cluster centers are distributed randomly at first, and a data point is assigned to the cluster nearest it in terms of Euclidean distance. Each cluster center is then updated to be the average of the points assigned to it. The data points are reassigned to clusters and the cluster means are recomputed until the distance of the data points and the centers are within some threshold or some maximum number of iterations is reached.

A SOM [8] is a type of neural network used to produce a low-dimensional, discretized representation of the space of the training data. A SOM identifies features across the range of input patterns. Neurons compete to be activated, and only one is activated at any one time. A SOM needs very little to no preliminary data cleansing [9].

Recall that the supervised learning techniques we investigated are FNN, SVM, and naïve Bayes classifiers. An artificial neural network (ANN) is a computational model based on the structure and functions of a biological neural network [8]. In a FNN, or multilayer perceptron, input vectors are put into input nodes and fed forward in the network. The inputs and first-layer weights will determine whether the hidden nodes will fire. The output of the neurons in the hidden layer and the second-layer weights are used to determine which of the output layer neurons fire. The error between the network output and targets is computed using the sum-of-squares difference. This error is fed backward through the network to update the edge weights in a process known as back propagation.

SVMs rely on preprocessing to represent patterns in the data in a high dimension, usually higher than the original feature space, so that classes that are entangled in the original space are separated by hyper-planes at higher dimension. Training a SVM [9] involves choosing a (usually nonlinear) function that maps the data to a higher-dimensional space. Choices are generally decided by the user's knowledge of the problem domain. SVMs can reduce the need for labeled training instances.

Naïve Bayes classifiers form a supervised learning technique that belongs to a family of classifiers based on Bayes' theorem with a strong assumption about the independence of features [9]. Assumptions and the underlying probabilistic model allow us to capture any uncertainty about the model. This is generally done in a principled way by determining the probabilities of the outcomes. Bayes classifiers were introduced to solve diagnostic and predictive problems. Bayesian classification provides practical learning through the use of algorithms, prior knowledge, and observation of the data in combination. A Gaussian naïve Bayes classifier assumes that the conditional probabilities follow a Gaussian or normal distribution.

8.5 Results

The learning techniques were run on a machine running Windows 7 64-bit operating system with a 2.4 GHz quad core processor and 16 GB of RAM. Software from scikit-learn [10] was used for PCA, k-means, SVM, and Gaussian naïve Bayes classifiers. Software from PyBrain [11] was used for the FNN, and software from Weka [12] was used for the SOM. Weka is written in Java while scikit-learn and PyBrain are written in Python. We recorded the time taken by the classifiers produced by each technique to classify the data points in our test set. For the SOM, this involved executing Java code, while for the others Python code was run. We first present the results

for the supervised learning techniques, and then we present the results for the unsupervised learning techniques.

4.5.1 Supervised-Learning Results

To compare supervised learning techniques, we used the classification accuracy. The classification accuracy is the number of samples classified correctly over the number of samples in the dataset.

We ran a SVM with four different types of kernel functions: linear, radial basis (RBF, with $\gamma = 0.5$), and polynomial. Table 1 displays the accuracy that which our SVMs classified the 1169 data points in the test set mentioned above. The SVM was also trained with a PCA frontend and run on the same data. Table 2 displays the resulting classification accuracy.

Table 1: The classification accuracy of the SVM

Kernel	Linear	Radial Basis	Polynomial
Accuracy	0.326	0.286	0.714

Table 2: The classification accuracy of the SVM with PCA

Kernel	Linear	RBF	Polynomial
Accuracy	0.675	0.287	0.292

A Gaussian naïve Bayes classifier was trained and run with and without PCA. Table 3 shows the resulting classification accuracy.

Table 3: The accuracy of the Gaussian naïve Bayes classifier

Technique	Gaussian NB	Gaussian NB w/ PCA
Accuracy	0.714	0.287

A FNN classifier was trained and run with and without PCA. Table 4 shows the resulting classification accuracy.

Table 4: The classification accuracy of the FNN

Technique	FNN	FNN with PCA
Accuracy	0.9996	0.9996

Out of the four types kernel functions the SVM with a polynomial kernel function performed the best without PCA but the SVM with a linear kernel function performed the best

with PCA. The Gaussian naïve Bayes performed well without PCA but this inverted with PCA, but the FNN performed well with and without PCA.

Table 5 and 6 shows the time for each of the kernel functions of our SVM with and without PCA. Out of the four kernel functions used, the radial basis function performed the fastest but not as accurately without PCA. But with PCA, the polynomial kernel function performed faster than the other function, but was less accurate than the linear kernel.

Table 5: Timing of the SVM kernel functions without PCA

Kernel	Linear	Radial Basis	Polynomial
Timing	18	8	12

Table 6: Timing of the SVM kernel functions with PCA

Kernel	Linear	RBF	Polynomial
Timing	18	8	3

Table 7 shows the timing in milliseconds for the rest of our supervised learning techniques with and without PCA. Thus, the fastest classifier (Gaussian naïve Bayes with PCA) is also the least accurate, and the most accurate classifier (FNN with and without PCA) is also the slowest.

Table 7: Timing of the rest of our supervised learning techniques with and without PCA

Technique	Gaussian NB	Gaussian NB with PCA	FNN	FNN with PCA
Timing	19	1	450	470

4.5.2 Unsupervised-Learning Results

Regarding unsupervised learning techniques, we first ran k-means clustering without PCA with k equal to 4, 5 and 6. Then we ran k-means clustering with PCA with k again equal to 4, 5 and 6. For all values of k , with and without PCA, the k-means classifiers took very nearly 1 millisecond, with very little variation, to classify all 1169 data points in our test set. Figures 1-3 show the clusters produced when k equals 4, 5, and 6 (respectively) and PCA is used to reduce the data to three dimensions.

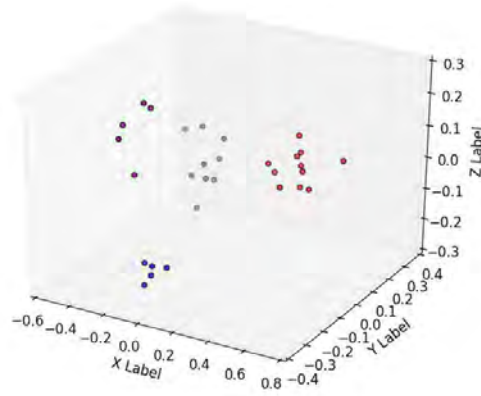


Figure 1: k-means with 4 clusters with PCA

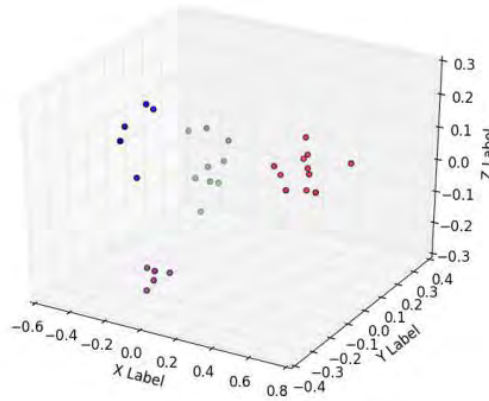


Figure2: k-means with 5 clusters with PCA

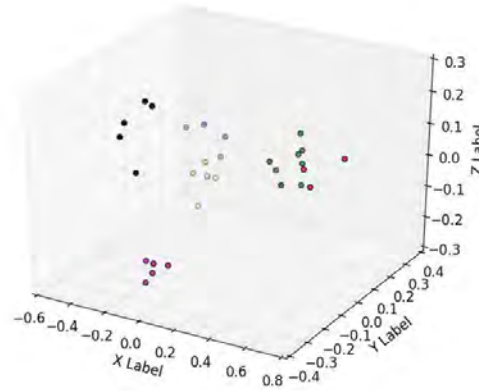


Figure 3: k-means with 6 clusters with PCA

We ran a SOM with 4, 5 and 6 neurons. Table 7 shows the time (in milliseconds) it took each of the SOM instances to classify all 1169 data points in our test set. Clearly, the SOM took much longer to classify data points than did the k-means classifiers.

Table 7: Timing of the SOM

Technique	SOM 4	SOM 5	SOM 6
Time	8640 ms	12240 ms	24170 ms

The SOM with four output neurons gave four particularly sharp clusters. Such clustering can be anticipated given our experimental set-up, as we expect signals from four different sources. First of all, there are signals from the crack growth itself, but crack growth deeper in the specimen produces waveforms with rather different characteristics from those produced on the surface, and this difference is enough to pull the crack data into two distinct clusters. Next, there is friction where the specimen is attached, accounting for a third cluster. Finally, the electrical environment produced a consistent kind of noise, giving rise to a fourth cluster. The k-means classifier with $k = 4$, whether with or without PCA, identified four similar clusters, but they were much less distinct. This suggests that, in some situations at least, the greater accuracy of the SOM may be worth the wait.

8.6 Conclusion

This paper reports on work that is part of our development of an agent-based structural health monitoring (SHM) system. The data used are acoustic signals, and one attempts to classify these signals according to source, those associated with crack growth being particularly significant. The agents are for the most part proxies for communication- and computation-intensive techniques. Given a situation of interest, they negotiate to determine a pattern of techniques for understanding the situation. Such a pattern determines a workflow. The agents respond in an intelligent way by determining a constellation of techniques appropriate for the situation at hand. It is critical that the system have a repertoire of classifiers with different characteristics so that a combination appropriate for the situation at hand can generally be found.

Following Worden and his colleagues [2], we use unsupervised learning for identifying the existence and location of damage but supervised learning for identifying the type and severity of damage. Our objective at this stage is to explore various machine-learning techniques and note their characteristics so that various combinations of them may be used appropriately in various circumstances. The supervised learning techniques investigated are support vector machines (SVM), naïve Bayes classifiers, and feed-forward neural networks (FNN). The unsupervised learning techniques investigated are k-means (with k equal to 4, 5, and 6) and self-organizing maps (SOM, with 4, 5, and 6 output neurons). For each technique except SOM, we tested a version with principal component analysis (PCA) as a frontend to reduce data dimensionality to three principal components, and we tested another version without PCA.

Turning to the results, first of all for the supervised learning techniques, FNN with or without PCA was the most accurate and the slowest while naïve Bayes without PCA was the second most accurate and second slowest. Indeed, FNN is much more accurate and much slower than even naïve Bayes without PCA: 0.9996 vs. 0.71 and 470 ms to process the 1169 samples vs. 19 ms. SVM with a polynomial kernel function and without PCA was just as accurate as naïve Bayes without PCA (0.71) but faster (12 ms to process the 1169 samples). Some of techniques were so inaccurate as not to be useful: SVM with an RBF kernel function (with and without PCA), naïve Bayes with PCA, and SVM with a polynomial kernel function and PCA all had accuracies of only about 0.29. SVM with a linear kernel function was quite slow (18 ms with and without PCA) and straddled the middle of the accuracy range: PCA here increased accuracy immensely:

0.68 vs. 0.33. Regarding unsupervised learning techniques, k-means classified all data points in our test set in about 1 millisecond regardless of the value of k and whether PCA was used. SOM took much longer, in the range of 10-20 seconds, increasing significantly with increasing number of output neurons. The much greater running time, however, might be compensated for as there is reason to think that SOM provides clusters that are more distinct and meaningful than those provided by k-means. Note that PCA sometimes improves accuracy and sometimes reduces it; it results in faster classification in one case and no significant change in run time in the others. This suggests that reducing data dimensions to three as we did with PCA can often obscure information needed for classification.

We can consider combinations of classifiers trained in unsupervised and supervised learning mode, the first to find existence and location of damage and then the second to determine the extent and type of damage. In a practical situation, we look at a large number of events and watch for when hundreds are classified as originating from crack growth. So we can tolerate a certain amount of inaccuracy. Cracks, however, grow over months, so generally processing speed is not an issue for continuous monitoring, and it would be natural to use SOM then FNN. But if an entire aircraft or other extensive structure is scanned periodically, processing speed might be multiplied by factors in the hundreds, and we might consider, for example, k-means and SVM with a polynomial kernel function and without PCA.

These results are generally encouraging for our multiagent system as they reveal significant differences in the characteristics of the machine learning techniques investigated. For both supervised and unsupervised techniques, there is a trade-off between accuracy and fast runtime, and this trade-off can be exploited by the agents in finding a combination of techniques appropriate for a given situation. We indicated how the approach followed here can be generalized for exploring the characteristics of machine-learning techniques for monitoring various kinds of structures.

Future work will include investigation of the physical reality behind the clusters found with unsupervised learning. We are tagging the waveforms as they are classified so that we may get full information on the waveforms that end up in each cluster. Future work will also consider which classifiers work best in combination with which other classifiers.

Finally, we will investigate various approaches to dimensionality reduction. We will investigate what dimensionalities provided by PCA are most efficient in various situations. And we will consider alternatives to PCA. We are looking at coalition game theory as a way to select combinations of feature that do the best job distinguishing the data by class. We are also considering GEFWS (Genetic and Evolutionary Feature Selection and Weighting), which evolves linear combinations of feature values (over a certain threshold) that optimize classification accuracy.

References

- [1] A. Esterline, K. Krishnamurthy, M. Sundaresan, T. Alam, D. Rajendra, & W. Wright, "Classifying Acoustic Emission Data in Structural Health Monitoring using Support Vector Machines," *In Proceedings of AIAA Infotech@ Aerospace 2010 Conference*, 2010.

- [2] K. Worden , C. Farrar, G. Manson, & G. Park, “The fundamental axioms of structural health monitoring,” *Proceedings of the Royal Society A: Mathematical, Physical and Engineering Science*, vol. 463, no.2082, pp.1639-1664, 2007.
- [3] E. Figueiredo, G. Park, C. Farrar, K. Worden, & J. Figueiras, “Machine learning algorithms for damage detection under operational and environmental variability,” *Structural Health Monitoring*, vol. 10, no. 6, pp. 559-572, 2011.
- [4] D. Tibaduiza, M. Torres-Arredondo, L. Mujica, J. Rodellar, , & C. Fritzen, “A study of two unsupervised data driven statistical methodologies for detecting and classifying damages in structural health monitoring”. *Mechanical Systems and Signal Processing*, vol. 41 no. 1, pp. 467-484, 2013.
- [5] C. Farrar, & K. Worden, “An introduction to structural health monitoring,” *Philosophical Transactions of the Royal Society A: Mathematical, Physical and Engineering Sciences*, vol. 365, no. 1851 , pp. 303-315, 2007.
- [6] C. Farrar, & N. Lieven, “Damage prognosis: the future of structural health monitoring,” *Philosophical Transactions of the Royal Society A: Mathematical, Physical and Engineering Sciences*, vol. 365, no.1851, pp. 623-632, 2007.
- [7] M. Wooldridge, “An introduction to multiagent systems,” John Wiley & Sons, 2009.
- [8] C. Bishop, *Pattern recognition and machine learning*, Vol. 1, New York: springer, 2006.
- [9] R. Duda, P. Hart, & D. Stork, *Pattern classification*. John Wiley & Sons, 1999.
- [10] F. Pedregosa, G. Varoquaux, A. Gramfort, V. Michel, B. Thirion, O. Grisel, & É. Duchesnay, “Scikit-learn: Machine learning in Python”, *The Journal of Machine Learning Research*, vol. 12, pp. 2825-2830, 2011.
- [11] T. Schaul, J. Bayer, D. Wierstra, Y. Sun, M. Felder, F. Sehnke, & J. Schmidhuber, “PyBrain,” *The Journal of Machine Learning Research*, vo l. 11, pp. 743-746, 2010.
- [12] Weka: *Practical machine learning tools and techniques with Java implementations*, 1999.

PART 9: A MULTIAGENT-BASED STRUCTURAL HEALTH MONITORING SYSTEM

Abstract

The overall architecture involves motes (battery-powered devices with processors, memory, attached sensors. And wireless communication capability) that feed data streams to workstations on which a multiagent system allocates resources to interpret and fuse the data. Agent services are made available as Web services, resulting in an end-to-end architecture, extending from the sensors to the users consuming the information to support decisions. Prototypes have been developed for interpreting individual datastreams, for hierarchical integration of monitoring agents, and for publishing status and alerts on the Web and rendering them on a user's "dashboard."

9.1 Introduction

The overall architecture involves motes (small battery-powered devices with processors, memory, and wireless communication capability and that can be equipped with a variety of sensors) that feed data streams to workstations on which a multiagent system allocates resources to interpret and fuse the data. An agent is autonomous and generally capable of reactive and proactive behavior. Agents communicate via a special agent communication language and negotiate to determine what tasks are carried out and how they are carried out in achieving system-wide goals. In this architecture, most agents serve as advocates for data- or communication-intensive techniques. Once the agents have negotiated an approach to a task, processes carrying out the respective techniques are activated in a workflow. This results in a very flexible and responsive system (due to the agents) that processes data efficiently (thanks to the workflow). Certain agents perform specialized tasks, such as feature extraction and classification of events based on extracted feature vectors. Other agents, called monitor agents, coordinate activities or advocate for analytic techniques. Negotiation among monitor agents results in a hierarchy where agents higher up monitor parts of the structure that cover several of the parts monitored by agents lower down in the hierarchy. This hierarchy reconfigures itself as the parts of the structure requiring additional attention vary over time. Certain agent services are made available as Web services, which are available to users or analytic software running on remote sites, and agents can push alerts to users who subscribe to them. This results in an end-to-end architecture, extending from the sensors to the users consuming the information to support decisions.

The following begins with a section describing an initial prototype that involves a single datastream and a single monitor agent that finds agents to perform subtasks in interpreting the events whose effects are recorded in the datastream. This section also outlines the work done with feature extraction and machine learning (for classifying events given feature vectors). The next section describes a simple prototype with a very small hierarchy of monitor agents. This is followed by a section outlining how the multiagent monitoring system makes Web services available. Next, we describe a prototype dashboard for displaying to a user the information provided by the Web services as well as alerts and warnings sent by the agents using a messaging

system. The last section is a brief summary of miscellaneous topics addressed in the past that are still of interest.

9.2 A prototype for handling datastream

An initial prototype (see Figure 1) handles just one stream of data from sensor mote and thus requires just one monitor agent to find agents to perform its subtasks [7]. A LabVIEW application superposes several decaying sinusoids and sends the result over a data socket to an Imote2 mote, which transmits the data stream wirelessly to an Imote2 connected to the workstation hosting the multiagent system. (The motes are programmed in nesC.) A special data agent controls this data stream and sends control signals to the mote from which the data stream originates. This prototype assumes that one or more feature extractors will extract from the data stream feature vectors that will be input to a classifier to produce a stream of classifications of events detected by the simulated sensor.

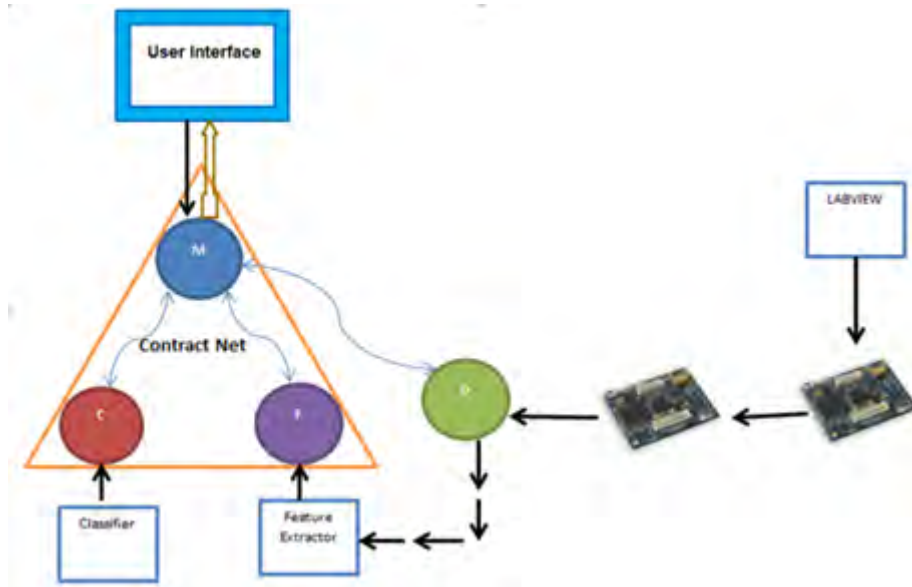


Figure 1: A prototype for handling one data stream.

Figure 1 has a square icon labeled “Feature Extractor” that stands for the collection of feature-extraction techniques available. There is an arrow from this icon to a round icon labeled “F”; this is the collection of feature-extraction agents, each advocating for one of the feature-extraction techniques. Similarly, there is a square icon labeled “Classifier” that stands for the classifier techniques available and an arrow from it to a round icon labeled “C”, standing for the collection of corresponding classifier agents. The round icon on the right labeled “D” stands for the data agent; the arrow into it represents the datastream it controls (which does not literally “pass through” it). The round icon labeled “M” (above the icons for the feature-extraction and classifier agents) stands for the monitor agent tasked with classifying events detected by the sensors that are

the source for this data stream. Under different circumstances, different ways of classifying these events are appropriate. The input arrow from the user-interface icon to the

Monitor-agent icon indicates input specifying context-related attributes of the classification task. The arrow in the opposite direction indicates classification-related information relevant to the current context; this is generally just a time-stamped classification but could also be an alert or information about the state of the sensors or of the interpretation of the datastream. The two-headed arrow between the monitor-agent icon and the data-agent agent indicates direct communication between the two agents, allowing the monitor agent to track the state and activity of the data agent and the datastream, and allowing it to influence the data agent's control of the mote and sensors.

The two-headed arrow between the monitor-agent icon and the icon for the classifier agents indicates use of the contract net protocol to allow the monitor agent to find a classifier agent for the classify-given-feature-values subtask of the classify-given-raw-data task in the current context. The contract net protocol is a widely used announce-bid-award problem-solving protocol. An agent with a task (or problem) decomposes it into subtasks (or subproblems) for each of which it becomes the manager. For a given subtask, the manager broadcasts an announcement containing information about the subtask. An agent receiving this message has the option of sending a bit with information on how it would perform the subtask. The manager then evaluates the bids and sends an award message (possibly including further information) to the agent submitting the winning bid (which becomes the contractor for the subtask) and reject messages to the other bidders. Note that this is a simple form of negotiation (the manager and contractor select each other), keeping with the autonomy of agents.

The two-headed arrow between the monitor-agent icon and the icon for the feature-extraction agents likewise indicates use of the contract net protocol to allow the monitor agent to find one or more feature-extraction agents for the feature-extraction subtask of the classify-given-raw-data task. At this point, the subtask is qualified not only by the current context but also by the classifier already selected: the feature extractor(s) must provide values for the features used by the selected classifier. The way the contract net protocol proceeds here is slightly more involved than the way it proceeds with finding a classifier since the monitor might have to award the subtask to more than one feature extractor since there may be no single feature extractor that provides values for all features required by the classifier.

Once a classifier agent and one or more feature-extraction agents have been found for the current context, the monitor agent sends a message to the workflow system to set up a workflow involving the techniques advocated by these agents. It also sends a message to the data agent. The stream of time-stamped event classifications flows into the monitor agent, which processes it as appropriate.

The single-monitor, single-datastream prototype described above in fact just communicates the LabVIEW-generated signal and, downstream, a sequence of integers through a workflow consisting of stubs corresponding to the agents selected in the instances of the contract net protocol.

This was appropriate as the point of the prototype was to implement the agents and have them negotiate as described above.

Current work involves implementing the workflow system, allowing it to activate and coordinate instances of the techniques, and creating an interface so that agents and other external actors may specify workflows along with their inputs and outputs. The current version allows simple workflows to be set up semi-automatically.

The software for the classification techniques is written in Python and uses the parameters established by machine learning techniques that were implemented last year. Training for a given technique is done offline with stored data, and the learned parameters are written to a file. When the technique is needed for classifying live data, the classifying software reads these parameters. The machine learning techniques used have generally been paired with code that uses principal component analysis (PCA) to reduce the dimensionality of the feature space. When classification is done on live data, the linear transformations used with a given machine-learning technique must be used when the corresponding classifier is used on live data. Therefore, the coefficients for these linear transformations are also written to file when training is complete and read when the corresponding classification technique is used. We think of a given classification technique and the accompanying PCA-derived linear transformations as a single unit, advocated for by a given classifier agent.

The machine learning techniques covered include neural networks and techniques for unsupervised learning, including k-means algorithms and self-organizing maps. The website for the Marsland machine-learning text [6] provides implementations in Python. More sophisticated Python implementations of a vast range of machine-learning techniques are provided online by at the scikit-learn site [3], which is supported by Google and INRIA. The open source code is being enhanced for our specific purposes. The open source code with which we start uses Python's NumPy numerical library and relevant modules from Python's SciPy library.

Feature extraction techniques are being developed using NumPy and SciPy. Some features (such as rise time and amplitude) are easily derived from the time-domain signal. Most of the features used by our mechanical engineering collaborators fall into this category. Our collaborators also find the correlations between an input signal and a set of signal templates as a kind of finger print of the input signal; this has been prototyped. We will also explore extracting features from the frequency-domain representation of a signal, although such features are not used by our collaborators. We are also looking at Kalman for filter estimating state variables from times series of feature values

9.3 A prototype with hierarchy of monitor agents

When multiple data streams are available from various parts of the monitored structure, possible interactions and vulnerabilities must be considered. In addition, computational resources might not be adequate to maintain a consistently high level of interpretation of all datastreams. Finally, meaningful interpretation may depend on fusing data from several streams.

compositions of agent services and Web services to be created, managed, and administered by the DF (directory facilitator) agent in the JADE framework. The WSIG architecture is composed of two elements: the WSIG servlet and the WSIG gateway agent. Current implementation [8] makes several agent services available as Web services, and the list of such services being considered includes the following.

- Status of the overall structure, status of the components (hierarchical)
- Information about services available in the context of a given monitor agent (or component)
- Values of specific features from specific data streams (sensors)
- Results of analytic routines applied to values from the sensors
- Histories of status and specific feature values (for given sensors) (e.g., over the last 4 minutes or over a 3 month period)
- Manufactures' nominal values of components (static; lookup)
- Alert service that displays via the dashboard (Qpid—only tangential here)

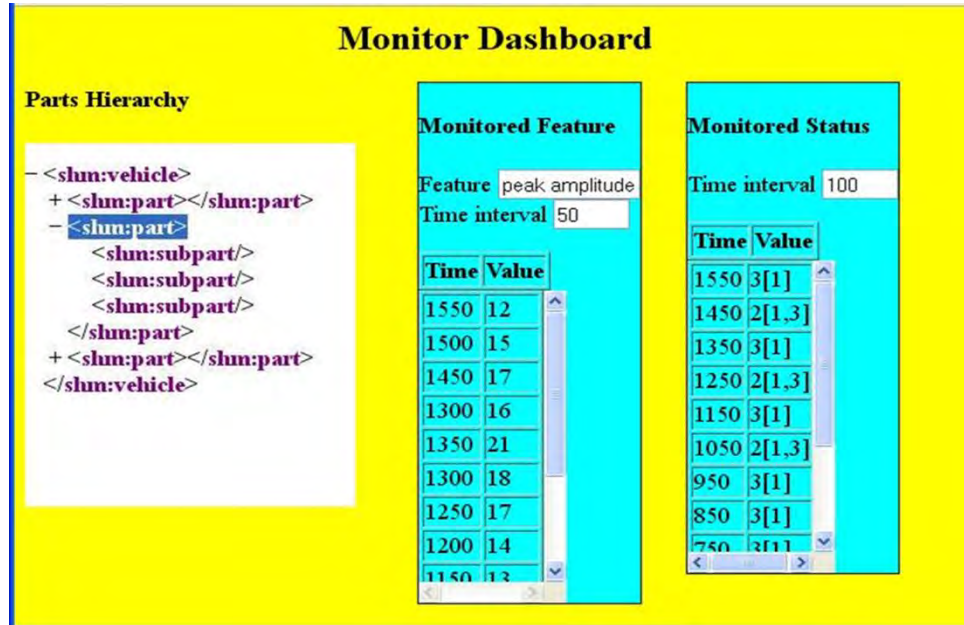


Figure 3: A snapshot of the dashboard prototype

The WSIG-provided Web services are being supplemented for communicating alerts and warnings with messaging capability provided by the Queue Processor Interface Daemon (Qpid) [1], an Apache capability enabling entities to communicate with each other via queues called topics. Qpid is an implementation of the Advanced Message Queuing Protocol (AMQP). A client that subscribes to a “topic” provided by a server is automatically provided with any message that the server puts on that topic. This provides “push” communication (initiated by the server) in contrast to the “pull” communication (initiated by the server) of Web services.

Dashboard: The dashboard [4] allows the user to view the status of system components in a meaningful and efficient way—see Figure 3. XML data documents that are provided by the sensor web are converted via XSLT stylesheets to HTML documents that can be rendered on a variety of devices, including workstations to hand-held devices. There are three parts on the dashboard: a parts hierarchy, the monitored status of a part, and the value of a selected feature of the monitored part. The parts hierarchy is for selecting what part is to be monitored at certain time intervals. In the Monitored Status column, values for the monitored part are listed followed by the values of interest for the subparts in brackets. These values denote categories identified by the classification agents. The time interval (in seconds) between values is specified in a textbox. Finally, in the Monitored Feature column, the user selects a feature of the signal analyzed for the selected part and interval between samples. Ajax technology is being used to update fields in the dashboard window without the need to update the entire window. In the current prototype, an alert pushed out by the multiagent system to dashboard users causes an alert box to appear. Future work will incorporate alerts in a meaningful way into the layout of the dashboard. Future work will also allow some control of the monitor system through the dashboard.

Miscellaneous Topics: The Gaia agent-oriented analysis and design methodology [9] was used to come up with designs for agent roles, and it will continue to be used. We are exploring elements of coalition game theory (see Chapter 13 of [10]) as a possible complement to the contract net protocol. Coalition game theory investigates settings in which groups of agents (“coalitions”) may enforce cooperative behavior. The contract net protocol essentially results in a greedy approach to finding agents to perform subtasks: the best agent for the subtask first announced is awarded that subtask even though an overall better allocation of subtasks to agents might award a different subtask to that agent. Coalition game theory avoids this greedy strategy by taking all subtasks into consideration at once.

Finally, we continue to experiment with a variety of wireless sensor motes and customized hardware configurations. We are also continuing to experiment with Agilla mobile agents on more advanced motes.

References

- [1] Apache Software Foundation. 2004-2008. Apache QPID: Open source amp messaging. Retrieved 2-20-2013 from <https://cwiki.apache.org/qpid/index.html>.
- [2] Bullock, Gina, “Applying the Contract Net Protocol to the Monitoring of Structural Health of Aircraft,” ADMI 2013 (2013 Symposium on Computing at Minority Institutions), Virginia Beach, VA, April 11 - 13, 2013.
- [3] Cournapeau, D. et al., *scikit-learn: Machine Learning in Python*, INRIA, accessed Aug. 2012 at <http://scikit-learn.org/>
- [4] Etim, David, “A Dashboard for Viewing Web-services Data for Structural Health Monitoring,” ADMI 2013 (2013 Symposium on Computing at Minority Institutions), Virginia Beach, VA, April 11 - 13, 2013.
- [5] JADE Board (2011). *JADE Web Services Integration Gateway (WSIG) Guide*. Retrieved 2-18-2013 from http://jade.tilab.com/doc/tutorials/WSIG_Guide.pdf.

- [6] Marsland, Stephen, *Machine Learning: An Algorithmic Perspective*, Chapman and Hall/CRC, 2009
- [7] Patterson, Tori, “Wireless Sensor Networks and Data Fusion for Structural Health Monitoring of Aircraft,” ADMI 2013 (2013 Symposium on Computing at Minority Institutions), Virginia Beach, VA, April 11 - 13, 2013.
- [8] Rocker, Charnae, “Web Services for a Structural Health Monitoring System,” ADMI 2013 (2013 Symposium on Computing at Minority Institutions), Virginia Beach, VA, April 11 - 13, 2013.
- [9] Wooldridge, Michael, Jennings, Nicholas R., & Kinny, David. (2000). The Gaia Methodology for Agent-Oriented Analysis and Design. *Autonomous Agents and Multi-Agent Systems*, 3, 285-312.
- [10] Wooldridge, Michael, *An Introduction to MultiAgent Systems*, Wiley, 2nd ed., 2009.